

Insight into the multifunctionality of TiO₂-based catalyst

Meeprasert, J.

DOI

[10.4233/uuid:e88a9277-41a0-495e-8af2-561fbe1a543b](https://doi.org/10.4233/uuid:e88a9277-41a0-495e-8af2-561fbe1a543b)

Publication date

2023

Document Version

Final published version

Citation (APA)

Meeprasert, J. (2023). *Insight into the multifunctionality of TiO₂-based catalyst*. [Dissertation (TU Delft), Delft University of Technology]. <https://doi.org/10.4233/uuid:e88a9277-41a0-495e-8af2-561fbe1a543b>

Important note

To cite this publication, please use the final published version (if applicable).
Please check the document version above.

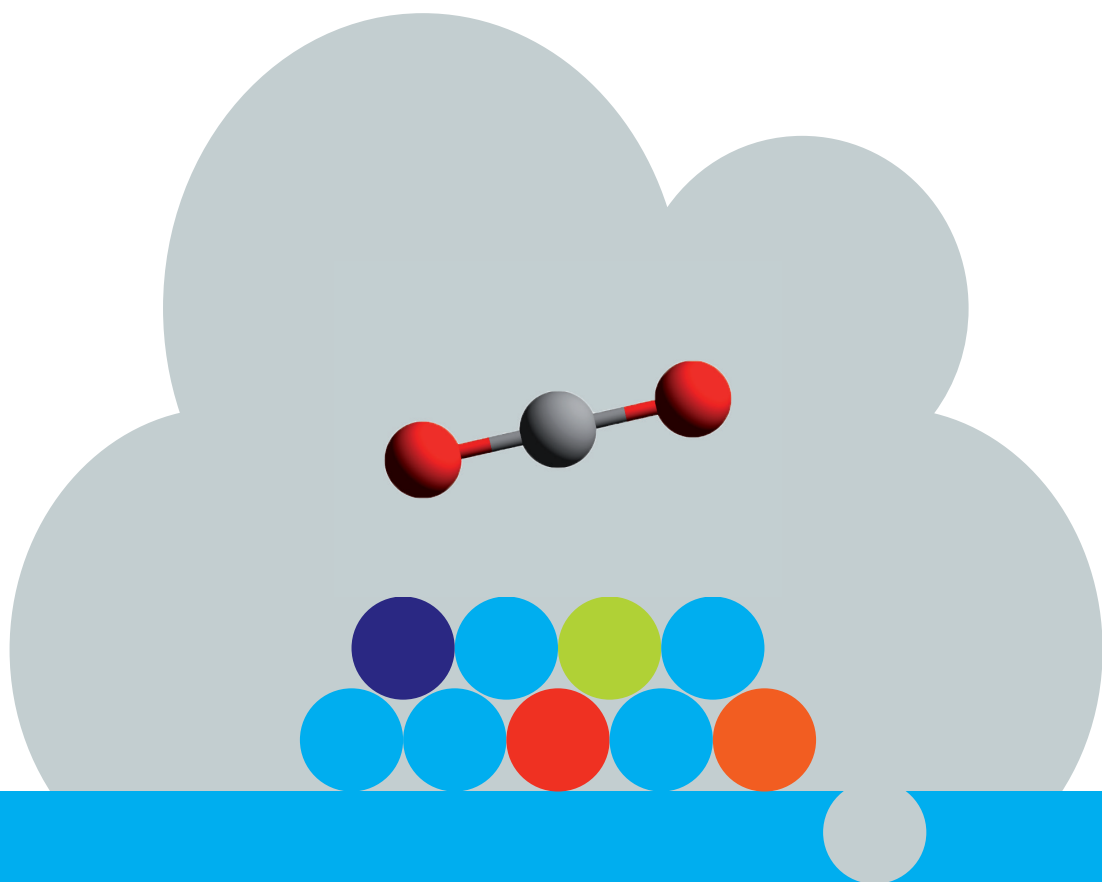
Copyright

Other than for strictly personal use, it is not permitted to download, forward or distribute the text or part of it, without the consent of the author(s) and/or copyright holder(s), unless the work is under an open content license such as Creative Commons.

Takedown policy

Please contact us and provide details if you believe this document breaches copyrights.
We will remove access to the work immediately and investigate your claim.

Insight into the multifunctionality of TiO_2 -based catalyst



Jittima Meeprasert

Insight into the multifunctionality of TiO₂-based catalyst

Dissertation

for the purpose of obtaining the degree of doctor
at Delft University of Technology
by the authority of the Rector Magnificus,
Prof.dr.ir. T.H.J.J. van der Hagen,
chair of the Board of Doctorates
to be defended publicly on
Wednesday, 15 March 2023 at 15:00 o'clock

by

Jittima MEEPRASERT

Master of Science in Chemistry,
Kasetsart University, Thailand,
Born in Bangkok, Thailand

This dissertation has been approved by the promotor.

Promotor: Prof.dr. E. A. Pidko

Copromotor: Dr. G. Li

Composition of the doctoral committee:

Rector Magnificus

Chairperson

Prof.dr. E. A. Pidko

Delft University of Technology, promotor

Dr. G. Li

Wageningen University and Research, copromotor

Independent members:

Dr. N. Artrith

Utrecht University

Prof.dr. B.M. Szyja

Wroclaw University, Poland

Prof.dr.ir. A. Urakawa

Delft University of Technology

Dr.ir. M.A. van der Veen

Delft University of Technology

Prof.dr. F.M. Mulder

Delft University of Technology

The work described in this dissertation was carried out in the Inorganic Systems Engineering (ISE) group, Department of Chemical Engineering, Faculty of Applied Science, Delft University of Technology. The research was supported by the Royal Thai Government Scholarship and the European Research Council under the European Union's Horizon 2020 Research and Innovation Program (Grant Agreement No. 725686). Access to SurfSARA supercomputer resources was sponsored by the Netherlands Organization for Scientific Research (NWO).

Printed by: Proefschriftspecialist

Cover by: Jittima Meeprasert

Copyright © 2023 by Jittima Meeprasert

ISBN 978-94-6384-413-0

An electronic version of the dissertation is available at TU Delft library

Contents

1 Introduction	1
2 CO₂ hydrogenation to CH₃OH on Cd₄/TiO₂	27
3 C₆H₆ esterification with CO₂ and CH₃OH on K₂CO₃/TiO₂	49
4 CH₄ esterification with CO₂ and CH₃OH on K₂CO₃/TiO₂	65
5 Benzonitrile hydrogenation on Au₁₃/TiO₂	77
Summary	95
Samenvatting	99
Acknowledgements	105
Curriculum Vitae	107
List of Publications	109

1

Introduction

1.1 Heterogeneous catalyst and its multifunctionality

Catalysis is a mechanism by which the rate of chemical reactions can be accelerated by adding a promoting chemical, namely “catalyst,” that is not consumed during the chemical process [1]. The function of a catalyst is to lower the activation energy of the reaction and often provide an alternative reaction pathway without affecting the energy difference between reactant and product, as shown in Figure 1.1. An ideal catalyst should maximize the conversion of reactants, produce only the desired products, and maintain its function for prolonged periods of reaction time [2].

Generally, catalysts are divided into two main classes, depending on their phase compared to reactants or products: homogeneous and heterogeneous catalysts. A homogeneous catalyst is a catalyst in the same phase as the reactants or products. In contrast, a heterogeneous catalyst is in a different phase from the reaction mixture. The most common form of heterogeneous catalyst is solid, while the reactants or products are gases or liquids. This feature leads to the major advantage of heterogeneous catalysts is that the catalyst can be separated from the reaction mixture by simple methods, such as filtration. Thus, solid catalysts can be easily recycled, resulting in low operation costs, which are the key targets of the industrial production processes. Solid catalysts also often exhibit high thermal and mechanical stability, facilitating thus their utilization on large scales. Therefore, heterogeneous catalysts have been widely used in the chemical industry, accounting for approximately 80% of all commercialized catalysts [3].

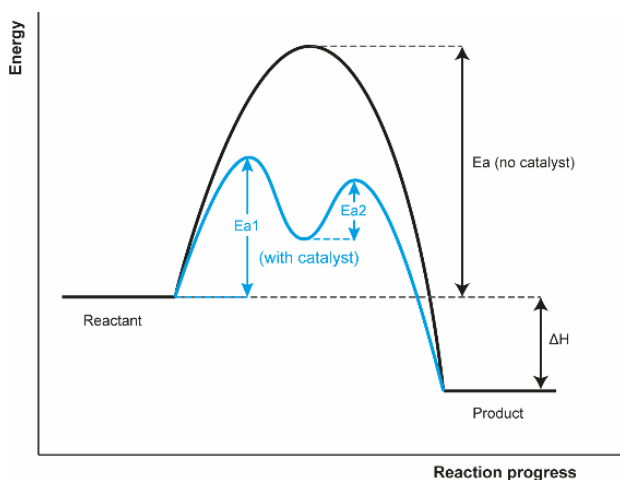


Figure 1.1 The effect of a catalyst on the activation energy and pathway of a chemical reaction.

Despite having many advantages, heterogeneous catalysts have some drawbacks. Table 1.1 lists the advantages and disadvantages of homogeneous and heterogeneous catalysts [4]. One of the main fundamental issues for many solid catalysts is the difficulty of controlling the reaction selectivity. Most common solid catalyst materials feature a wide variety of surface species and active sites with varied reactivity, giving rise to diverging reactivity within the same catalyst particle and promoting the formation of undesirable products next to the primary target conversion process. In some cases, such side products strongly bind with the active sites, prevent the regeneration of the active sites for recycling adsorption of the reactants, and thus lead to the deactivation of the catalytic surfaces. Therefore, understanding the role of the surface sites and identifying the reaction or deactivation processes in heterogeneous catalysts is critically important for learning how to control their catalytic activity and selectivity and develop effective catalysts.

Table 1.1 An overview of the main advantages and disadvantages of homogeneous and heterogeneous catalysts [4].

	Homogeneous catalyst	Heterogeneous catalyst
Selectivity	High	Low
Catalyst separation and recovery	Difficult and expensive	Easy and cheap
Thermal stability	Low	High
Mass transfer limitations	Very rare	Can be severe
Structure/Mechanism	Defined	Undefined
Applicability	Limited	Wide

Nevertheless, many different active sites are not necessarily a negative aspect of solid catalysts. In fact, different chemical moieties can exhibit synergistic effects and help promote desirable conversions by forming the so-called “multifunctional catalytic ensembles.” In such a multifunctional system, each catalytic moiety can either work separately to catalyze different elementary reaction steps or work cooperatively to promote the same reaction. Thus, naturally, solid catalysts that exhibit multifunctionality are promising candidates for facilitating multistep reactions. For instance, the tremendous progress in hydrogenation chemistry witnessed in the last decade is related to the developments of multifunctional heterogeneous catalysts [5-7].

Among various solid catalysts, oxide-supported metal catalysts (metal/oxide) have been frequently used and developed in recent years. In such systems, the catalytic phase of transition metals is dispersed on the surface of oxides. The dispersion of metals on oxides initially aims to stabilize the metal nanoparticles and increase the surface area to volume ratio. The attention to such catalysts has been raised since it was found that the oxide support can also influence catalytic performances. The reducible oxides such as TiO_2 , Fe_2O_3 , CeO_2 , and many other transition-metal oxides are particularly attractive for heterogeneous catalyst design. These supports provide versatile and tunable surface characteristics such as surface acidity and basicity. Furthermore, terminal OH groups and surface defects (steps, corners, and vacancies) can act as anchoring sites for metal nanoparticles to boost their dispersion and stabilization of the support surface [8]. For these reasons, the well-defined structure and function are crucial for designing rather complicated and efficient metal/oxide catalysts and understanding their catalytic activity.

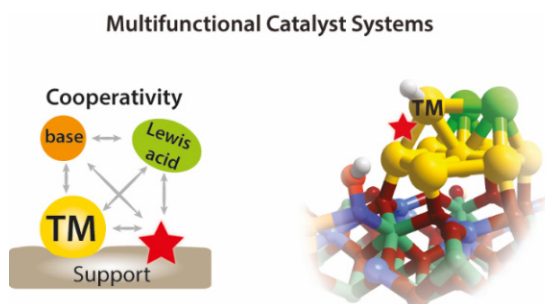


Figure 1.2 Schematic illustration of how different species on the surface can form catalytic ensembles. The synergetic action of the transition metal (TM) centers with the reactive sites of the support, along with the presence of base and Lewis acid promoters, allows for establishing a favorable conversion path for the substrates along the predefined route.

A schematic representation of a cooperative metal/oxide catalyst interface is shown in Figure 1.2. The metals with the reactive sites of the support acting as independent reactive sites or as base and Lewis acid species promoters work cooperatively to catalyze reactions. It should be noted that the reactivity of atoms at the direct contact of metal and oxide support – the interface, is typically different from the other sites. This is due to the synergistic effect between the metal and the oxide support known as the metal-support interactions (MSI) [9, 10]. The MSI comprises several phenomena, such as (i) charge transfer, (ii) interfacial perimeter, (iii) nanoparticle morphology, (iv) chemical composition, and (v) strong metal-support interaction (SMSI), as shown in Figure 1.3.

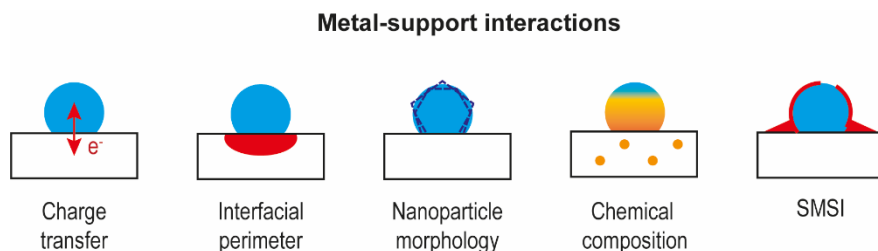


Figure 1.3 The five main phenomena of metal-support interactions (MSI).

To clarify, (i) the electrons at the interface might be rearranged upon the interaction between metal and oxide, resulting in the charge transfer. (ii) The electron's accumulation and depletion at the interfacial perimeter sites can affect the adsorption/desorption of molecules. (iii) The adhesion energy released from metal-oxide interactions can affect the morphology of metal nanoparticles. (iv) The redox process at metal and oxide support might induce the rearrangement of components and the formation of new phases. (v) The oxide support might be reduced and generate suboxides covering the metal nanoparticle, known as the SMSI [9]. Indeed, such MSI phenomena significantly impact the performance of metal/oxide catalysts by changing their structural and electronic properties [9, 10].

The primary focus of this thesis is on the molecular-level aspects of the MSI and its role in catalysis. For instance, the formation of multifunctional reactive ensembles at the interfacial perimeter and the charge transfer modulate the reactivity of the supported metal particles. Different mechanistic features arising from such MSI phenomena will be demonstrated in the subsequent chapters. Chapters 2 and 5 focus on the reactivity of titania-supported catalysts in the hydrogenation of CO₂ and aromatic amines. Mechanisms of C-H carboxylation reactions will be discussed in Chapters 3 and 4.

1.2 TiO₂-based catalysts

Titanium dioxide (titania or TiO₂) is one of the most versatile and widely-explored oxide materials used as a catalyst or catalyst support because of its high stability, nontoxicity, and cost-effectiveness [11]. In the context of this thesis, the unique features of titania extend well beyond its excellent ability to disperse the transition metal catalysts nicely in the form of well-defined nanoparticles to a wide range of tuneable MSI phenomena. The catalytic activity of TiO₂ mainly depends on their Lewis acid-base pairs which occur due to the presence of Ti⁴⁺ (Lewis acid) and O²⁻ (Lewis base) on the surface. The Brønsted acid (H⁺) can also be introduced to the surface of TiO₂ via the dissociation of H₂O or H₂ [11-14]. In addition, the deposition of metal nanoparticles on TiO₂ results in the formation of new active sites and, consequently, the changes in the activity and stability of the supported metal/TiO₂ catalyst. All these features are essential to creating highly complex multifunctional ensembles on the surface of TiO₂-supported metal catalysts, as schematically illustrated in Figure 1.2. The presence of Brønsted acid, Lewis acid, and Lewis base sites on TiO₂ can cooperate with the dispersed metals to enable the selective conversion of various chemical feedstocks.

Many studies have shown that both the crystal phase and the exposed surface structure of TiO₂ affect the catalytic properties of titania-based systems [11-14]. TiO₂ can crystallize in one of the three crystalline structures, namely anatase, brookite, and rutile (Figure 1.4). Each of these forms exhibits different physical characteristics, surface properties, and reactivities. Brookite is the least studied TiO₂ due to the difficulty of synthesizing the pure phase. A recent study found that brookite provides a higher activity than other forms of titania in some photocatalytic reactions [13, 15]. The rutile is the most stable and common form of TiO₂, with the highest density and refractive index [11]. However, it was reported that anatase becomes more stable than rutile when the particle size is smaller than 14 nm [16]. Furthermore, anatase typically exhibits higher photocatalytic activity than rutile [17]. Anatase is also preferred as a metal catalyst support because of its remarkably higher specific surface area [14]. Therefore, from this section onwards, the focus will be put on the anatase TiO₂.

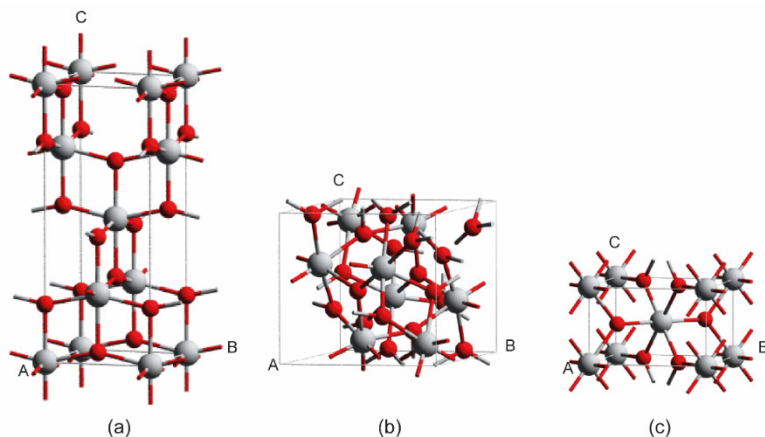


Figure 1.4 The bulk crystal structures of **(a)** anatase, **(b)** brookite, and **(c)** rutile TiO_2 .

The structure, stability and reactivity of anatase TiO_2 have been studied extensively over decades. The anatase TiO_2 has a tetragonal lattice ($P4_2/mnm$) with four TiO_2 units per unit cell (Figure 1.4a). The stability of anatase surfaces can be determined by surface energy calculations. For a series of low-index anatase surfaces, the (101) surface is thermodynamically most stable, followed by the (100), (001), and (110) surfaces, respectively [18-20]. The Wulff construction indicated that over 94% of the exposed surface area of the anatase crystals is represented by the (101) surface, whereas the (001) one is the minority surface having a fraction of about 6% [21].

The (101) surface (Figure 1.5a) contains 5- and 6-coordinated Ti atoms (Ti_{5C} , Ti_{6C}) and 2- and 3-coordinated O atoms (O_{2C} , O_{3C}). This surface has a sawtooth-like appearance, featuring alternating rows of Ti_{5C} and O_{2C} along the [010] direction. For the (100) surface (Figure 1.5b), O_{2C} , O_{3C} , and Ti_{5C} atoms are exposed on the outermost layer, while Ti_{6C} and O_{3C} atoms are at the bottom of the surface. In the case of the (001) surface (Figure 1.5c), the atomic structure is unclear due to its low stability and facile reconstruction. A study based on the add-oxygen model (AOM) method indicated that the surface contains exposed O_{2C} , O_{3C} , and Ti_{5C} centers [22], as illustrated in Figure 1.5c. An alternative surface structure featuring O_{2C} and Ti_{4C} exposed atoms was proposed by another literature based on the add-molecule model (ADM) method [23].

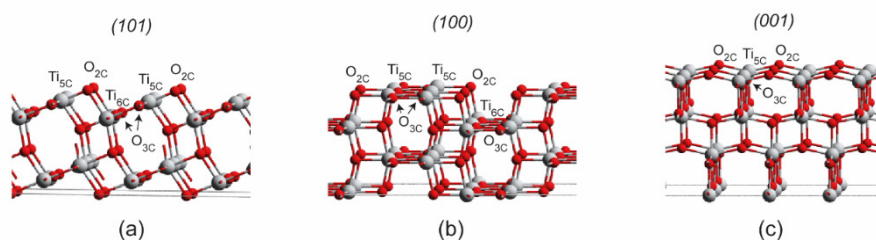


Figure 1.5 The surface morphology of anatase TiO₂ **(a)** (101), **(b)** (001), and **(c)** (100) surfaces.

The exposed Lewis acid-base pairs ($\text{Ti}^{4+}\text{-O}^{2-}$) are commonly considered to contribute to the surface reactivity of pristine TiO₂. It was reported that the Lewis acidity of Ti^{4+} sites on (101) is slightly higher than those on the (001) surface, while the Lewis basicity of O^{2-} sites on the (001) is stronger than that on the (101) surface [18, 24]. Several studies on the interaction of small molecules with different anatase surfaces indicated that the most stable (101) surface shows a lower intrinsic reactivity than the other ones. For example, the H₂O molecule dissociatively adsorbs on the (001) and (110) surfaces, while the molecular adsorption mode is observed on the (101) surface [14]. CO₂ is weakly adsorbed on the (101) surface with a linear configuration, while the formation of a variety of surface carbonates with stronger adsorption energy is observed on the (001) surface [24]. However, when considering the reactivity of supported catalytic ensembles, the dominant (101) surface appears the most relevant for practical catalytic applications.

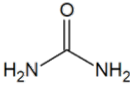
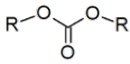

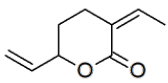

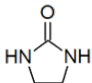
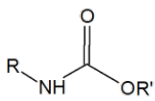
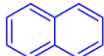
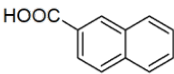
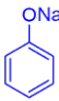
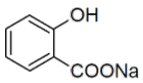
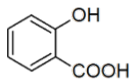

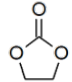
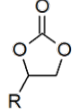
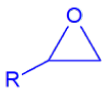
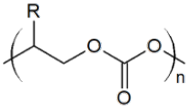
The reactivity of TiO₂ surface can be modified by introducing defects, with oxygen vacancies being the most common type of such surface defects. Removal of an oxygen atom from the surface leaves two excess electrons, which are trapped by the neighboring Ti sites. Thus, two Ti^{4+} sites are reduced to two Ti^{3+} , providing more electron-rich and reactive transition metal sites. The decreased coordination saturation of the Ti sites near the oxygen vacancy also contributes to the surface Lewis acidity. The formation of such defects can significantly impact the catalytic properties of the titania surface. For instance, the defective TiO₂ (101) surface was found to be more active than the perfect one for the reduction of CO₂ [25]. Besides, the surface oxygen vacancy can act as an anchoring site for the metal nanoparticles. For instance, a highly efficient and durable Pt-based electrocatalyst for oxygen reduction reaction has been prepared by anchoring Pt atoms on TiO₂ containing oxygen vacancies [26].

Because of the unique and tunable properties of titania, TiO_2 -based catalysts doped with various transition and non-transition metals have been synthesized and used in exploring different catalytic applications. Depending on the transition metal choice, different reactivity can be introduced to the titania-supported system [27]. For example, Pt/TiO_2 is an exceptional catalyst for the hydrogenation of various organic substrates with molecular H_2 [28]. Au/TiO_2 exhibited remarkable performance for the O_2 activation and the oxidation of organic molecules [29, 30]. Ru/TiO_2 is a promising candidate for the Fisher-Tropsch synthesis [31]. Re/TiO_2 [32] as well as related bimetallic catalysts such as Ni-Re/TiO_2 [33] and Pt-Re/TiO_2 [34] catalysts enabled highly selective reductive transformations of challenging ester substrates. Re/TiO_2 [35], Mo/TiO_2 [36], various metals promoted Co/TiO_2 [37], and other were also found to be uniquely active for the low-temperature and tunable conversions of carbon dioxide to value-added chemicals.

1.3 CO_2 conversion to chemicals

CO_2 capture and utilization have been attracting much attention as an important technology helping mitigate global warming and climate change because it could save fossil fuels and lower the CO_2 concentrations in the atmosphere. The utilization of CO_2 can be divided into the following categories: production of chemicals, production of fuels, enhanced biological utilization, and technological utilization that does not require CO_2 conversion [38]. Among them, the conversion of CO_2 to chemicals provides comprehensive benefits to the chemical industry [39]. Table 1.2 represents some of the chemicals that can be produced from CO_2 . The efficient conversion of CO_2 to chemical products is challenging because of its high thermodynamic stability. As illustrated in Figure 1.6, the Gibbs free energy of the CO_2 is lower than its reduction products, such as CO , CH_3OH , and CH_4 , which can directly be utilized in various downstream applications [38, 40]. Thus, the conversion of CO_2 always requires energy input through the reaction with more energetic reagents [41]. Among various reactive agents used for the conversion of CO_2 , H_2 is the most attractive candidate to offer an opportunity for sustainable development of atom-efficient energy technologies and environmentally benign chemical processes [42].

Table 1.2 Synthesis of chemicals from CO₂ with various reductants.

Reductants	Products		
H ₂	HCOOH	CH ₃ OH	CH ₄
CH ₄	CO	CH ₃ COOH	
NH ₃			
ROH			
Alkenes and Dienes			
Amines	HCONR ₂	R-N=C-O	
			
			
			
			
			

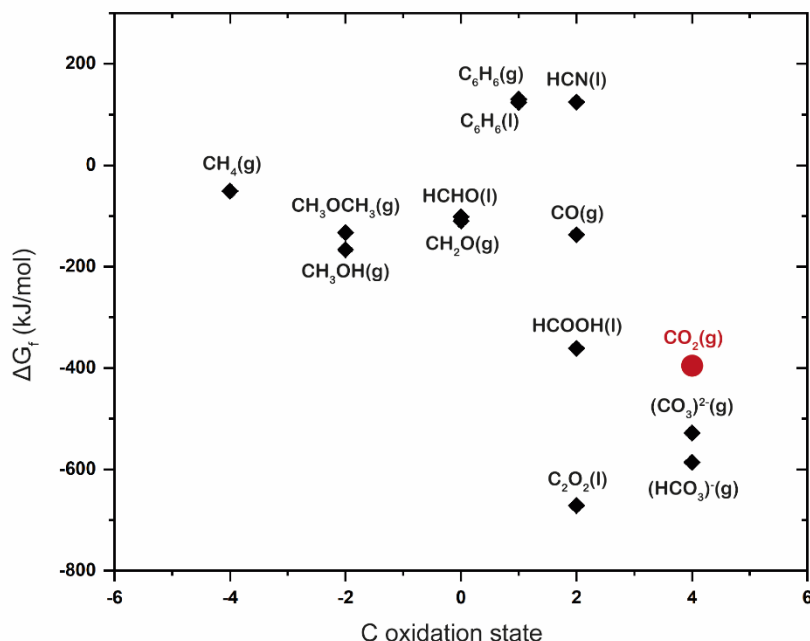


Figure 1.6 Gibbs free energy of the CO_2 compared with other chemicals.

The hydrogenation of CO_2 can be used to produce a variety of chemicals with important downstream applications. In particular, the valorization of CO_2 to valuable C1 building blocks such as CO , CH_4 , HCOOH , and CH_3OH attracts much attention from researchers in industry and academia [43, 44]. The catalytic conversion of CO_2 to such C1 chemicals is governed by three main reaction pathways (Figure 1.7): (1) the reverse water-gas shift (RWGS) pathway, (2) the direct C-O bond cleavage pathway, and (3) the formate pathway [45]. Each reaction pathway proceeds through several elementary steps and reaction intermediates leading to the formation of different products. Because of the complexity of this reaction network, the multifunctional TiO_2 -supported metal catalyst is a promising candidate for controlling the selectivity of the desired products. However, the promotion of different reaction channels can be anticipated because of various reactive ensembles formed at the multifunctional metal-support interface. Therefore, understanding the fine mechanistic details of these conversion paths over realistic models of supported heterogeneous catalysts may give an insight into the fundamental factors underlying their catalytic behavior.

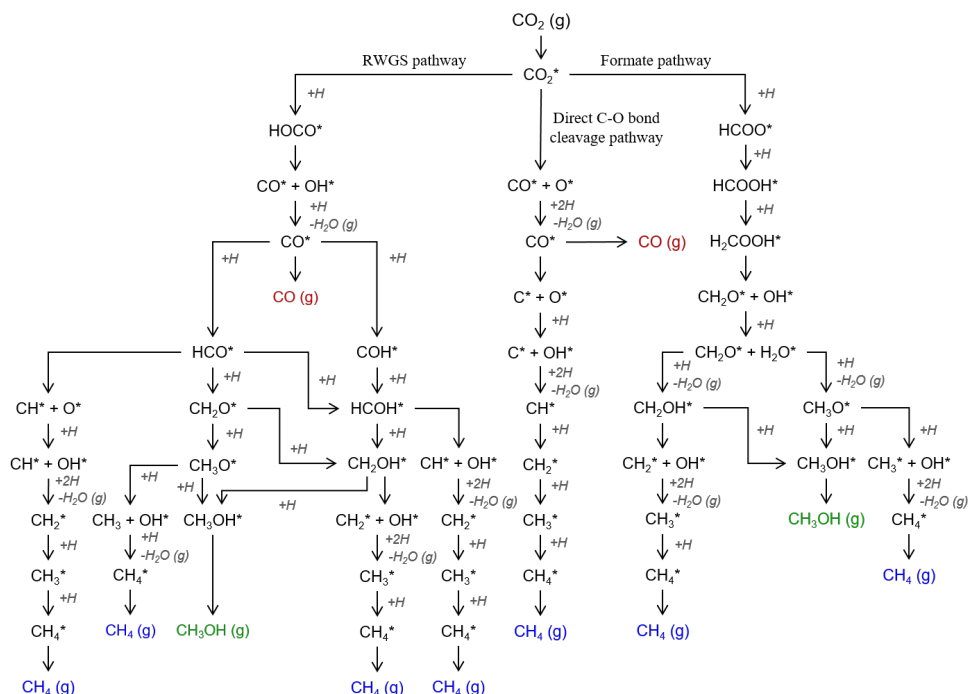


Figure 1.7 Possible reaction pathways for the hydrogenation of CO_2 .

Previous computational studies suggested that product selectivity can be determined by the binding strength of key intermediates with the catalytically active sites [45, 46]. The reaction networks in Figure 1.7 suggest that if we aim to design a catalyst with high activity and selectivity for the CH_3OH production, the CO^* , HCO^* , and CH_2O^* should be stabilized on the active site to facilitate their further reaction. In contrast, the CH_3O^* should be destabilized to allow its hydrogenation to form CH_3OH . However, the over-stabilization of some intermediates such as HCOO^* and CO^* might lead to the formation of highly stable resting states that would poison the catalytic surface. The scission of the C-O bond in CH_xO^* species, which competes with the hydrogenation process, is a critical step for the production of side-product (CH_4).

1.4 Computational modeling of complex multifunctional catalyst surfaces

The elucidation of the reaction mechanisms occurring at the active sites on the well-defined catalytic structures is crucial for the rational design of heterogeneous catalysts. In experiments, various spectroscopic methods such as X-ray diffraction/scattering (XRD), X-ray photoelectron spectroscopy (XPS), X-ray absorption spectroscopy (XAS), Raman, infrared spectroscopy (IR), transmission electron microscopy (TEM), and other methods have been performed to study what happens under reaction conditions [47]. It was found that the catalytic structures can change dramatically when exposed to reaction conditions or during chemical transformations. Furthermore, adsorbed species and dynamics at high temperatures and pressure can cause the restructuring of surfaces. These phenomena might lead to the formation of new functionalities or active sites that are not present before the reaction begins. Thus, identifying the real active sites and monitoring the catalytic processes under realistic working conditions are the persistent challenges in catalysis research. Fortunately, modern computational chemistry can help address them by giving insight into more details of the catalytic structure and its activities at the atomistic level.

In computational catalysis, theoretical calculations based on quantum chemical approaches, particularly the density functional theory (DFT), have been widely used as fundamental tools for understanding the catalytic processes [48-52]. Traditionally, the reaction mechanisms were explored within the concept of potential energy surface (PES), corresponding to simplified catalytic models under ultrahigh vacuum and at 0 K (OK/UHV). However, in the real system, catalysts usually operate under ambient or higher temperatures and pressures. Furthermore, the multifunctions of heterogeneous catalysts and the chemical transformations during the reaction raise issues of structural complexity that are difficult to model. Thus, the development of computational heterogeneous catalysis is currently evolving into studying the catalytic processes using models representing the conditions and environments encountered under realistic working conditions, in other words, *operando* conditions.

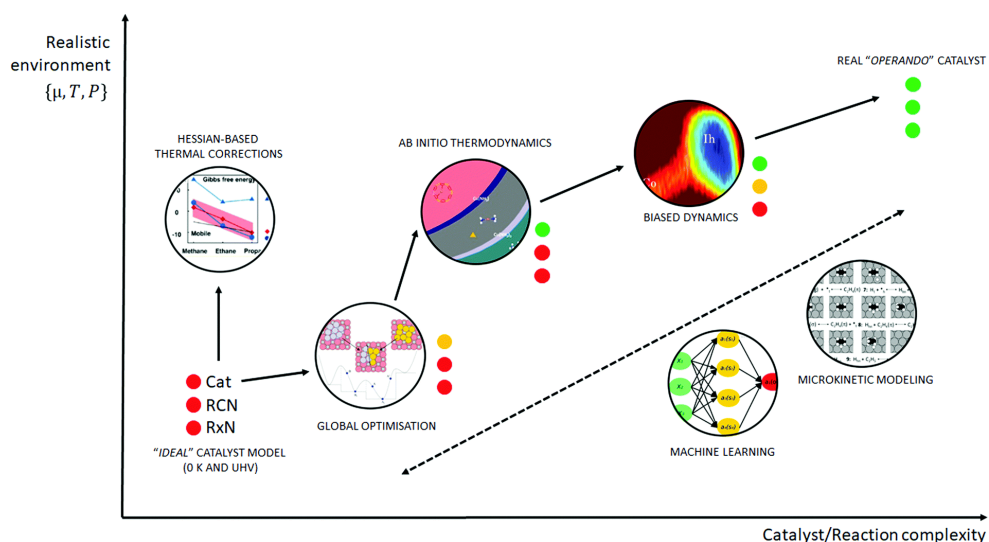


Figure 1.8 Schematic of the various computational methods applied to heterogeneous catalysis lies between an idealized UHV model and a realistic *operando* model. The traffic light depicts the quality of each method with respect to catalyst model complexity (Cat), reaction coordinate accuracy (RCN), and reaction network complexity (RxN) [48].

So far, many computational methods have been used to extend the conventional static models based on the 0 K/UHV to the *operando* conditions. Figure 1.8 illustrates a transition from 0K/UHV to *operando* conditions enabled by the introduction of four key computational methods [48]: (1) global optimization techniques, (2) ab initio constrained thermodynamics, (3) biased molecular dynamics simulations, (4) microkinetic modeling. The reaction environment (e.g., chemical potentials and temperature) becomes more realistic from the bottom to the top of the figure. At the same time, the development of computational methods results in the increased complexity of the catalytic system from left to right. Following such information, global optimization techniques are performed to screen candidate structures and search for stable active site formation. The ab initio thermodynamics can determine the thermodynamic stabilities of different active sites ensembles under varying reaction conditions, while the ab initio MD can identify the dynamic structures in environments with an explicit solvent or high reactant concentrations. Microkinetic modeling provides kinetic information from the known intermediates and reaction pathways that build up the reaction network [48, 53]. In addition, machine learning (ML) techniques can be used to assist in catalytic modeling, discovery, and prediction of chemicals with desired properties and prediction of reaction pathways without human biases [54–56].

In this thesis, the DFT calculations were employed together with the microkinetic modeling (MKM) to understand the catalytic processes. The MKM was used to reduce the complexity of the DFT-computed reaction networks and translate the atomistic details of molecular mechanisms into experimentally-measurable kinetic parameters, as schematically illustrated in Figure 1.9. Combining those two methods can identify the optimal reaction conditions so that the desired reaction pathway is enabled, resulting in the enhanced selectivity of the overall catalytic process. The general concepts and basics of each of these methods are briefly described in the following sections.

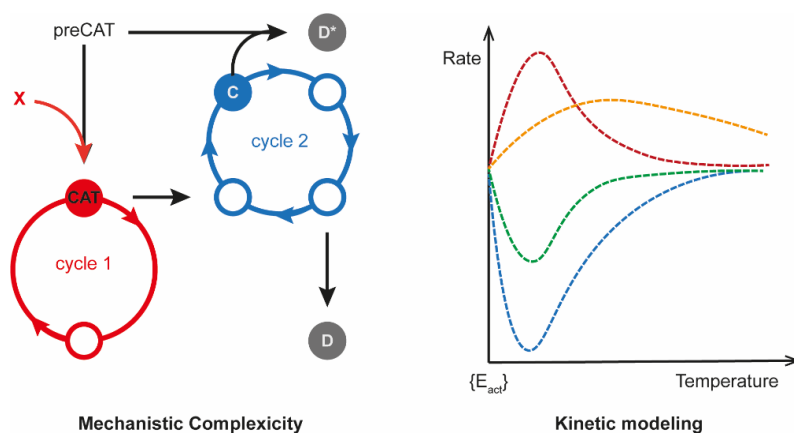


Figure 1.9 A principle scheme of the hierarchical modeling strategy within this thesis

1.4.1 Density functional theory (DFT)

Computational modeling based on density functional theory (DFT) has been a powerful research tool for analyzing spectroscopic data, modeling catalysts, and studying reaction mechanisms. By applying DFT, the electronic properties of a many-electron system (atoms, molecules, and materials) are determined by using functionals of the electronic charge density, which can be written as [57]:

$$\rho(r) = N \iint \cdots \int |\psi(r_1, r_2 \cdots r_N)|^2 ds dx_2 \cdots dx_N \quad (1)$$

where $\rho(r)$ is the total electronic density and $\psi(r_1, r_2 \cdots r_N)$ is the N-electron wave function.

The foundation of the DFT has been laid by the seminal work of Hohenberg and Kohn [58], which demonstrated formally that any ground state property of a system is a function of its electron density. However, this approach is not sufficient to calculate the actual electronic motion state. Kohn and Sham [59] extended this

theory to practice by using the electron-electron interaction potential of the density functional to obtain the lowest energy and the corresponding molecular orbitals and orbital energies. The overall energy functional can be written as follows:

$$E[\rho] = E^K[\rho] + E^V[\rho] + E^J[\rho] + E^{XC}[\rho] \quad (2)$$

where $E^K[\rho]$ is the kinetic energy of the electrons, $E^V[\rho]$ is the nuclear-electron attraction energy, $E^J[\rho]$ is the electron-electron repulsion energy, and $E^{XC}[\rho]$ is the exchange-correlation potential energy (electron-electron interaction).

Based on this approach, the exact energy of the system could in principle be obtained from the exact electron density. Unfortunately, the exact form of the exchange-correlation functional is not known, and various approximations and fitting procedures have been proposed to derive different practically approximated DFT methodologies. Various approximate exchange-correlation functionals such as local density approximation (LDA), generalized gradient approximation (GGA), metal-GGA (mGGA), and hybrid-GGA (hGGA) have been applied for the density functional development. These methods have been described in detail elsewhere [ref]. In computational catalysis, the GGA is preferred over the LDA due to its minor errors of ± 20 kJ/mol for adsorption and reaction energies [60, 61]. Among the GGA family, the mGGA produces much better electron densities, and hGGA shows the best performance in terms of accuracy [62].

1.4.2 Potential energy surface (PES)

Modeling the mechanism of chemical reactions requires the analysis of energetic and structural information of reactants, products, and intermediates occurring during the reaction. In that regard, the concept of potential energy surface (PES), a hyperdimensional energy surface as a function of geometric coordination [63], has been applied to the DFT calculations for studying the reaction mechanisms. A simple schematic PES is illustrated in Figure 1.10, similar to a hilly landscape composed of valleys, mountain passes, and peaks. Compared to a chemical reaction, the mountain passes are the reaction pathways. The valleys or minimum points are reactants, products, or intermediates, while the peaks or saddle points are transition state structures of the reaction. Thus, the shortest mountain pass between two valleys corresponding to reactant and product is the most preferred reaction pathway of the overall reaction.

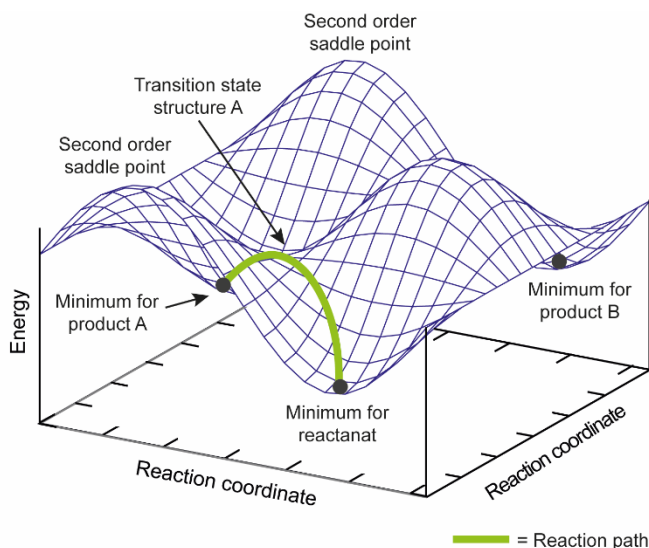


Figure 1.10 Model potential energy surface (PES) showing minima, transition state, a second-order saddle point, and reaction path.

Typically, the exploration of PES for any catalytic process involves the following steps: (1) identify/propose the active site(s), (2) predict/propose reaction mechanisms, (3) optimize candidate structures and calculate their electronic energy, (4) identify stationary points on the PES and locate the local minima and transition states connecting them to form reaction pathways, and finally (5) include temperature and pressure effects for obtaining the Gibbs free energy [49].

1.4.3 Microkinetic modeling (MKM)

The very high mechanistic complexity is one of the key challenges in closing the gap between the theoretical models and the experimental *operando* characterization of the catalytic systems. In practice, even the simplest catalytic process involves complex networks of competing and parallel multistep reaction channels taking place at different sites. The overall catalytic behavior is defined by the relative rates of each of the pathways leading to various intermediates and products, which in turn, are determined both by the intrinsic properties of the reactive ensembles and the conditions of the catalytic reactions. The DFT calculations enable the direct calculations of the rate constant of the individual reaction steps with sufficiently high accuracy. The resulting fine mechanistic details need to be further reduced to bridge the microscopic insights into the elementary steps and the macroscopic kinetics and measurable parameters of the catalytic processes.

The first principle-based kinetic modeling can be used to predict the activity of catalysts. Such models link the detailed microscopic insights into the catalytic reaction obtained from various computational approaches with the observable macroscopic kinetics of the reaction process. By reducing the mechanistic complexity, such kinetic models allow to point out computationally the abundant reaction intermediates or the composition of the catalyst under the specific reaction conditions. The resulting information on the preferred reaction pathway and the influence of the reaction conditions on catalyst behavior can be used for the *in silico* design of improving practical catalyst systems [48, 52]. The most popular approach to such kinetic models is the mean-field microkinetic modeling. In this approach, the reaction kinetics is described by using a macroscopic rate equation in which the surface state is represented by the coverage vector, as shown in the following equation

$$\left(\frac{d\theta_i}{dt} = \sum_j v_{ij} r_j f_j(\theta_1, \dots, \theta_N) \right)_{i=1-N} \quad (3)$$

where, θ_i is the surface coverage of species i at time t , v_{ij} is the stoichiometric coefficient for species i in step j , r_j is the rate of reaction j and f_i is a function of several coverages involved in step j . The adsorbates are assumed uncorrelated. This system of differential equations effectively describes all chemical processes taking place in the catalytic system. However, this approximation does not include the effect of spatial correlations in the distribution of reactants on the catalyst surface as well as the lateral interactions among adsorbates. The kinetic Monte Carlo method can be performed to solve that problems, but beyond the scope of my study.

The transition state theory (TST) and the DFT data can be applied to equation (3) for obtaining the rate constant, as shown in equation (4)

$$k_a = A_e \exp\left(\frac{-\Delta E_a}{k_B T}\right) \quad (4)$$

where the prefactor A_e accounts for the entropic changes between the initial and transition state of the elementary reaction and ΔE_a is the corresponding intrinsic activation energy barrier.

Besides, the apparent activation energy (E_a^{ap}) can be computed from the following equation:

$$E_a^{app} = k_B T^2 \left(\frac{\partial \ln(r_t)}{\partial T} \right)_P \quad (5)$$

In addition, the rate constant of the adsorption reaction can be calculated by the Hertz-Knudsen equation [64]:

$$k_{ads} = \frac{PA}{\sqrt{2\pi m k_B T}} S \quad (6)$$

where k_{ads} is the rate constant of adsorption reaction, P is the partial pressure of the adsorbate in the gas phase, A is the surface area of the adsorption site, m is the mass of adsorbate, k_B is the Boltzmann constant, T is the temperature, and S is the sticking coefficient.

The desorption reaction is calculated by the following equation:

$$k_{des} = \frac{k_B T^3}{h^3} \frac{A(2\pi m k_B)}{\sigma \theta_{rot}} e^{\left(\frac{-E_{des}}{k_B T} \right)} \quad (7)$$

where k_{des} is the rate constant of desorption reaction, h is the Plank's constant, σ is the symmetry number of a molecule, θ_{rot} is the rotational temperature of a molecule, and E_{des} is the desorption energy.

The differential equations are constructed using the rate constants and the set of elementary reaction steps. For each of the M components in the kinetic network, a single differential equation is in the form:

$$r_i = \sum_{j=1}^N \left(k_j v_i^j \prod_{k=1}^M c_k^{v_k^j} \right) \quad (8)$$

where r_i is the rate reaction, k_j is the elementary reaction constant, v_i^j is the stoichiometric coefficient of component i in elementary reaction step k and c_k is the concentration of component k on the catalytic surface.

The rate-determining step of the overall reaction can be identified by using the degree of the rate control (DRC) parameter as shown in the following equation [65-67]:

$$X_{RC,i} = \left[\frac{\partial \ln(r_t)}{\partial \ln(k_i)} \right]_{k_j \neq i, K_i} \quad (9)$$

The DRC is a weighing factor that directly relates such macroscopic rate parameters as the apparent activation energy and reaction orders and the

microscopic characteristic as the elementary reaction rates and activation barriers for elementary steps.

1.5 Scope of the thesis

The aim of this thesis is to investigate the role of multifunctional ensembles on the catalytic behaviour of TiO_2 -supported catalysts by means of DFT calculations. Particular emphasis is placed on the catalytic reactivity at the perimeter of metal- TiO_2 interface. Here, CO_2 reduction and nitrile hydrogenation are selected as the model representative and industrially relevant catalytic processes. Furthermore, I try to extend the DFT calculations from classical computational methods, based on inspection of the potential energy surface at 0 K and low reactant concentrations (OK/UHV model) towards the operando conditions by using the microkinetic modeling (MKM).

Chapter 2 investigates computationally the CO_2 hydrogenation to CH_3OH on a Cd_4/TiO_2 catalyst. This catalyst system has been discovered by our experimental collaborators as a highly selective and exceptionally active CO_2 reduction catalyst. This chapter is devoted to rationalizing the unique reactivity of this system. The main aim of my computational work was to explore the multiple-site cooperation effects on the mechanism and energetics of various CO_2 reduction paths to construct a detailed molecular-level picture of the complex reaction pathways on the catalyst surface. The resulting mechanistic insights were used to construct an MKM that was used to analyze the reaction networks at the relevant experimental conditions and construct the direct links with the experimental findings.

Chapter 3 discusses the mechanistic role of K_2CO_3 dispersed over defective TiO_2 support ($\text{K}_2\text{CO}_3/\text{TiO}_2$) for the esterification of benzene with CO_2 and CH_3OH , recently discovered experimentally. DFT calculations specifically addressed the role of the adsorbed K_2CO_3 for CO_2 activation and the fast deactivation of bare defective TiO_2 . An important message in this chapter resonating with some of the conclusions from Chapter 2 is that catalyst enhancement can be achieved through inhibition of some thermodynamically highly favourable reaction channels giving rise to the formation of resting states and effective surface poisoning rather than promoting the desirable chemical conversions. Minimizing side reactions and deactivation pathways is at least as promising strategy as the more common reactivity enhancement towards the desirable ones for catalyst development and optimization.

Chapter 4 builds up on the mechanistic study of the Chapter 3 and analyses whether this exciting catalytic chemistry enable by non-critical metal-based catalysts only can be used to convert more challenging and abundant substrates. Based on the excellent performance of $\text{K}_2\text{CO}_3/\text{TiO}_2$ catalyst in the carboxylation of the C-H bonds in benzene, we hypothesized that a similar mechanism could potentially be realized when using CH_4 as an alternative reactant. Potentially, this reaction could provide a route for the efficient valorization of natural gas and simultaneous CO_2 utilization. The DFT calculations presented in this chapter focus on providing insight into the mechanistic challenges associated with such a transformation and highlight the differences in reactivity of benzene and CH_4 , particularly for the key C-C coupling reaction with CO_2 .

Chapter 5 further explores the models and mechanistic concepts developed in the preceding chapters for providing a mechanistic explanation for the high reactivity and selectivity of Au/TiO_2 catalyst for the direct hydrogenation of benzonitrile to benzylamine, recently discovered by our experimental collaborators. To rationalize the experimental observations, the reaction mechanism was studied in detail by using Au_{13} clusters supported on a rutile TiO_2 surface as a model. The effect of Au_{13} cluster geometries on the catalytic reactivity is discussed. This study highlights the critical role of the multifunctional reaction environment at the metal-support interface for establishing a highly selective and efficient reduction of this challenging biomass-derived substrate. The proposed reaction mechanism consists of heterolytic H_2 dissociation at the $\text{Au}-\text{TiO}_2$ interface and the subsequent four consecutive H^+ and H^- transfer reaction steps involving the additional nitrile substrate activation by the Lewis acidic sites of the TiO_2 support. This chapter emphasizes and clarifies the role of each reactive center and their cooperation within the catalytic ensemble formed at the $\text{Au}-\text{TiO}_2$ interface.

References

1. Wilhelm Ostwald – Nobel Lecture: On Catalysis. <https://www.nobelprize.org/prizes/chemistry/1909/ostwald/lecture/>. 1909 [cited 2022, 2 Sep].
2. Védrine, J.C., 1 - Fundamentals of heterogeneous catalysis, in *Metal Oxides in Heterogeneous Catalysis*, J.C. Védrine, Editor. 2018, Elsevier. p. 1-41.
3. Védrine, J.C., *Metal Oxides in Heterogeneous Oxidation Catalysis: State of the Art and Challenges for a More Sustainable World*. *ChemSusChem*, 2019. 12(3): p. 577-588.

4. Fadhel, A.Z., P. Pollet, C.L. Liotta, and C.A. Eckert, *Combining the Benefits of Homogeneous and Heterogeneous Catalysis with Tunable Solvents and Nearcritical Water*. *Molecules*, 2010. **15**(11): p. 8400-8424.
5. Pritchard, J., G.A. Filonenko, R. van Putten, E.J.M. Hensen, and E.A. Pidko, *Heterogeneous and homogeneous catalysis for the hydrogenation of carboxylic acid derivatives: history, advances and future directions*. *Chem. Soc. Rev.*, 2015. **44**(11): p. 3808-3833.
6. Tamura, M., R. Tamura, Y. Takeda, Y. Nakagawa, and K. Tomishige, *Catalytic hydrogenation of amino acids to amino alcohols with complete retention of configuration*. *Chem. Commun.*, 2014. **50**(50): p. 6656-6659.
7. Wang, Y., Y. Shen, Y. Zhao, J. Lv, S. Wang, and X. Ma, *Insight into the Balancing Effect of Active Cu Species for Hydrogenation of Carbon–Oxygen Bonds*. *ACS Catal.*, 2015. **5**(10): p. 6200-6208.
8. Lang, R., X. Du, Y. Huang, X. Jiang, Q. Zhang, Y. Guo, K. Liu, B. Qiao, A. Wang, and T. Zhang, *Single-Atom Catalysts Based on the Metal–Oxide Interaction*. *Chem. Rev.*, 2020. **120**(21): p. 11986-12043.
9. van Deelen, T.W., C. Hernández Mejía, and K.P. de Jong, *Control of metal-support interactions in heterogeneous catalysts to enhance activity and selectivity*. *Nat. Catal.*, 2019. **2**(11): p. 955-970.
10. Li, Y., Y. Zhang, K. Qian, and W. Huang, *Metal–Support Interactions in Metal/Oxide Catalysts and Oxide–Metal Interactions in Oxide/Metal Inverse Catalysts*. *ACS Catal.*, 2022. **12**(2): p. 1268-1287.
11. Oi, L.E., M.-Y. Choo, H.V. Lee, H.C. Ong, S.B.A. Hamid, and J.C. Juan, *Recent advances of titanium dioxide (TiO₂) for green organic synthesis*. *RSC Adv.*, 2016. **6**(110): p. 108741-108754.
12. Wu, L., C. Fu, and W. Huang, *Surface chemistry of TiO₂ connecting thermal catalysis and photocatalysis*. *Phys. Chem. Chem. Phys.*, 2020. **22**(18): p. 9875-9909.
13. De Angelis, F., C. Di Valentin, S. Fantacci, A. Vittadini, and A. Selloni, *Theoretical Studies on Anatase and Less Common TiO₂ Phases: Bulk, Surfaces, and Nanomaterials*. *Chem. Rev.*, 2014. **114**(19): p. 9708-9753.
14. Bourikas, K., C. Kordulis, and A. Lycourghiotis, *Titanium Dioxide (Anatase and Rutile): Surface Chemistry, Liquid–Solid Interface Chemistry, and Scientific Synthesis of Supported Catalysts*. *Chem. Rev.*, 2014. **114**(19): p. 9754-9823.
15. Kandiel, T.A., L. Robben, A. Alkaim, and D. Bahnemann, *Brookite versus anatase TiO₂ photocatalysts: phase transformations and photocatalytic activities*. *Photochem. Photobiol. Sci.*, 2013. **12**(4): p. 602-609.
16. Zhang, H. and J. F. Banfield, *Thermodynamic analysis of phase stability of nanocrystalline titania*. *J. Mater. Chem.*, 1998. **8**(9): p. 2073-2076.

17. Luttrell, T., S. Halpegamage, J. Tao, A. Kramer, E. Sutter, and M. Batzill, *Why is anatase a better photocatalyst than rutile? - Model studies on epitaxial TiO₂ films*. *Sci. Rep.*, 2014. **4**(1): p. 4043.
18. Mino, L., A.M. Ferrari, V. Lacivita, G. Spoto, S. Bordiga, and A. Zecchina, *CO Adsorption on Anatase Nanocrystals: A Combined Experimental and Periodic DFT Study*. *J. Phys. Chem. C*, 2011. **115**(15): p. 7694-7700.
19. Esch, T.R., I. Gadaczek, and T. Bredow, *Surface structures and thermodynamics of low-index of rutile, brookite and anatase – A comparative DFT study*. *Appl. Surf. Sci.*, 2014. **288**: p. 275-287.
20. Arrouvel, C., M. Digne, M. Breyse, H. Toulhoat, and P. Raybaud, *Effects of morphology on surface hydroxyl concentration: a DFT comparison of anatase–TiO₂ and γ -alumina catalytic supports*. *J. Catal.*, 2004. **222**(1): p. 152-166.
21. Lazzeri, M., A. Vittadini, and A. Selloni, *Structure and energetics of stoichiometric TiO₂ anatase surfaces*. *Phys. Rev. B*, 2001. **63**(15): p. 155409.
22. Wang, Y., H. Sun, S. Tan, H. Feng, Z. Cheng, J. Zhao, A. Zhao, B. Wang, Y. Luo, J. Yang, and J.G. Hou, *Role of point defects on the reactivity of reconstructed anatase titanium dioxide (001) surface*. *Nat. Commun.*, 2013. **4**(1): p. 2214.
23. Lazzeri, M. and A. Selloni, *Stress-driven reconstruction of an oxide surface: The anatase TiO₂(001)-(1 \times 4) surface*. *Phys. Rev. Lett.*, 2001. **87**(26): p. 266105-1.
24. Mino, L., G. Spoto, and A.M. Ferrari, *CO₂ Capture by TiO₂ Anatase Surfaces: A Combined DFT and FTIR Study*. *J. Phys. Chem. C*, 2014. **118**(43): p. 25016-25026.
25. Ji, Y. and Y. Luo, *New Mechanism for Photocatalytic Reduction of CO₂ on the Anatase TiO₂(101) Surface: The Essential Role of Oxygen Vacancy*. *J. Am. Chem. Soc.*, 2016. **138**(49): p. 15896-15902.
26. Chen, Y., J. Chen, J. Zhang, Y. Xue, G. Wang, and R. Wang, *Anchoring Highly Dispersed Pt Electrocatalysts on TiO_x with Strong Metal–Support Interactions via an Oxygen Vacancy-Assisted Strategy as Durable Catalysts for the Oxygen Reduction Reaction*. *Inorg. Chem.*, 2022. **61**(12): p. 5148-5156.
27. Bagheri, S., N. Muhd Julkapli, and S. Bee Abd Hamid, *Titanium Dioxide as a Catalyst Support in Heterogeneous Catalysis*. *Sci. World J.*, 2014. **2014**: p. 727496.
28. Macino, M., A.J. Barnes, S.M. Althahban, R. Qu, E.K. Gibson, D.J. Morgan, S.J. Freakley, N. Dimitratos, C.J. Kiely, X. Gao, A.M. Beale, D. Bethell, Q. He, M. Sankar, and G.J. Hutchings, *Tuning of catalytic sites in Pt/TiO₂ catalysts for the chemoselective hydrogenation of 3-nitrostyrene*. *Nat. Catal.*, 2019. **2**(10): p. 873-881.

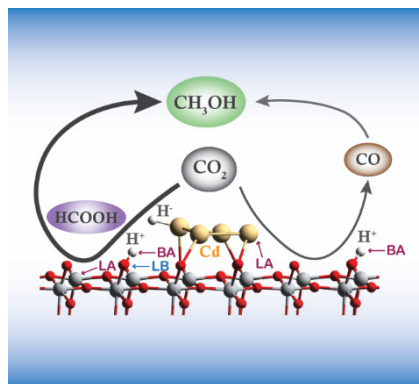
29. Panayotov, D.A., A.I. Frenkel, and J.R. Morris, *Catalysis and Photocatalysis by Nanoscale Au/TiO₂: Perspectives for Renewable Energy*. *ACS Energy Lett.*, 2017. **2**(5): p. 1223-1231.
30. Huang, J., S. He, J.L. Goodsell, J.R. Mulcahy, W. Guo, A. Angerhofer, and W.D. Wei, *Manipulating Atomic Structures at the Au/TiO₂ Interface for O₂ Activation*. *J. Am. Chem. Soc.*, 2020. **142**(14): p. 6456-6460.
31. Zhang, Y., X. Su, L. Li, H. Qi, C. Yang, W. Liu, X. Pan, X. Liu, X. Yang, Y. Huang, and T. Zhang, *Ru/TiO₂ Catalysts with Size-Dependent Metal/Support Interaction for Tunable Reactivity in Fischer–Tropsch Synthesis*. *ACS Catal.*, 2020. **10**(21): p. 12967-12975.
32. Toyao, T., S.M.A.H. Siddiki, A.S. Touchy, W. Onodera, K. Kon, Y. Morita, T. Kamachi, K. Yoshizawa, and K.-i. Shimizu, *TiO₂-Supported Re as a General and Chemoselective Heterogeneous Catalyst for Hydrogenation of Carboxylic Acids to Alcohols*. *Eur. J. Chem.*, 2017. **23**(5): p. 1001-1006.
33. Liu, K., J. Pritchard, L. Lu, R. van Putten, M.W.G.M. Verhoeven, M. Schmitkamp, X. Huang, L. Lefort, C.J. Kiely, E.J.M. Hensen, and E.A. Pidko, *Supported nickel–rhenium catalysts for selective hydrogenation of methyl esters to alcohols*. *Chem. Commun.*, 2017. **53**(70): p. 9761-9764.
34. Pritchard, J., A. Ciftci, M.W.G.M. Verhoeven, E.J.M. Hensen, and E.A. Pidko, *Supported Pt-Re catalysts for the selective hydrogenation of methyl and ethyl esters to alcohols*. *Catal. Today*, 2017. **279**: p. 10-18.
35. Ting, K.W., T. Toyao, S.M.A.H. Siddiki, and K.-i. Shimizu, *Low-Temperature Hydrogenation of CO₂ to Methanol over Heterogeneous TiO₂-Supported Re Catalysts*. *ACS Catal.*, 2019. **9**(4): p. 3685-3693.
36. Len, T., M. Bahri, O. Ersen, Y. Lefkir, L. Cardenas, I.J. Villar-Garcia, V. Pérez Dieste, J. Llorca, N. Perret, R. Checa, E. Puzenat, P. Afanasiev, F. Morfin, and L. Piccolo, *Ultradispersed Mo/TiO₂ catalysts for CO₂ hydrogenation to methanol*. *Green Chem.*, 2021. **23**(18): p. 7259-7268.
37. Li, W., G. Zhang, X. Jiang, Y. Liu, J. Zhu, F. Ding, Z. Liu, X. Guo, and C. Song, *CO₂ Hydrogenation on Unpromoted and M-Promoted Co/TiO₂ Catalysts (M = Zr, K, Cs): Effects of Crystal Phase of Supports and Metal–Support Interaction on Tuning Product Distribution*. *ACS Catal.*, 2019. **9**(4): p. 2739-2751.
38. Aresta, M., A. Dibenedetto, and A. Angelini, *Catalysis for the Valorization of Exhaust Carbon: from CO₂ to Chemicals, Materials, and Fuels. Technological Use of CO₂*. *Chem. Rev.*, 2014. **114**(3): p. 1709-1742.
39. Tabanelli, T., D. Bonincontro, S. Albonetti, and F. Cavani, *Chapter 7 - Conversion of CO₂ to Valuable Chemicals: Organic Carbonate as Green Candidates for the Replacement of Noxious Reactants*, in *Studies in Surface Science and Catalysis*, S. Albonetti, S. Perathoner, and E.A. Quadrelli, Editors. 2019, Elsevier. p. 125-144.

40. Song, C., *Global challenges and strategies for control, conversion and utilization of CO₂ for sustainable development involving energy, catalysis, adsorption and chemical processing*. *Catal. Today*, 2006. **115**(1): p. 2-32.
41. Li, W., H. Wang, X. Jiang, J. Zhu, Z. Liu, X. Guo, and C. Song, *A short review of recent advances in CO₂ hydrogenation to hydrocarbons over heterogeneous catalysts*. *RSC Adv.*, 2018. **8**(14): p. 7651-7669.
42. Wang, W., S. Wang, X. Ma, and J. Gong, *Recent advances in catalytic hydrogenation of carbon dioxide*. *Chem. Soc. Rev.*, 2011. **40**(7): p. 3703-3727.
43. Jangam, A., S. Das, N. Dewangan, P. Hongmanorom, W.M. Hui, and S. Kawi, *Conversion of CO₂ to C1 chemicals: Catalyst design, kinetics and mechanism aspects of the reactions*. *Catal. Today*, 2020. **358**: p. 3-29.
44. Alam, M.I., R. Cheula, G. Moroni, L. Nardi, and M. Maestri, *Mechanistic and multiscale aspects of thermo-catalytic CO₂ conversion to C₁ products*. *Catal. Sci. Technol.*, 2021. **11**(20): p. 6601-6629.
45. Kattel, S., P. Liu, and J.G. Chen, *Tuning Selectivity of CO₂ Hydrogenation Reactions at the Metal/Oxide Interface*. *J. Am. Chem. Soc.*, 2017. **139**(29): p. 9739-9754.
46. Li, Y., S.H. Chan, and Q. Sun, *Heterogeneous catalytic conversion of CO₂: a comprehensive theoretical review*. *Nanoscale*. **7**(19): p. 8663-8683.
47. Zhu, Y., J. Wang, H. Chu, Y.-C. Chu, and H.M. Chen, *In Situ/Operando Studies for Designing Next-Generation Electrocatalysts*. *ACS Energy Lett.*, 2020. **5**(4): p. 1281-1291.
48. Grajciar, L., C.J. Heard, A.A. Bondarenko, M.V. Polynski, J. Meeprasert, E.A. Pidko, and P. Nachtigall, *Towards operando computational modeling in heterogeneous catalysis*. *Chem. Soc. Rev.*, 2018. **47**(22): p. 8307-8348.
49. Morales-García, Á., F. Viñes, J.R.B. Gomes, and F. Illas, *Concepts, models, and methods in computational heterogeneous catalysis illustrated through CO₂ conversion*. *Wiley Interdiscip. Rev. Comput. Mol. Sci.*, 2021. **11**(4): p. e1530.
50. Eisenstein, O. and S. Shaik, *Computational Catalysis: A Land of Opportunities*. *Top. Catal.*, 2022. **65**(1): p. 1-5.
51. Studt, F., *Grand Challenges in Computational Catalysis*. *Front. Catal.*, 2021. **1**: p. 658965.
52. Chen, B.W.J., L. Xu, and M. Mavrikakis, *Computational Methods in Heterogeneous Catalysis*. *Chem. Rev.*, 2021. **121**(2): p. 1007-1048.
53. Shi, X., X. Lin, R. Luo, S. Wu, L. Li, Z.-J. Zhao, and J. Gong, *Dynamics of Heterogeneous Catalytic Processes at Operando Conditions*. *JACS Au*, 2021. **1**(12): p. 2100-2120.
54. Keith, J.A., V. Vassilev-Galindo, B. Cheng, S. Chmiela, M. Gastegger, K.-R. Müller, and A. Tkatchenko, *Combining Machine Learning and*

- Computational Chemistry for Predictive Insights Into Chemical Systems. Chem. Rev.*, 2021. **121**(16): p. 9816-9872.
55. Ma, S. and Z.-P. Liu, *Machine Learning for Atomic Simulation and Activity Prediction in Heterogeneous Catalysis: Current Status and Future. ACS Catal.*, 2020. **10**(22): p. 13213-13226.
56. Yang, W., T.T. Fidelis, and W.-H. Sun, *Machine Learning in Catalysis, From Proposal to Practicing. ACS Omega*, 2020. **5**(1): p. 83-88.
57. Blinder, S.M., *Chapter 14 - Density functional theory*, in *Introduction to Quantum Mechanics (Second Edition)*, S.M. Blinder, Editor. 2021, Academic Press: San Diego. p. 235-244.
58. Hohenberg, P. and W. Kohn, *Inhomogeneous electron gas. Phys. Rev.*, 1964. **136**(3B): p. B864-B871.
59. Kohn, W. and L.J. Sham, *Self-Consistent Equations Including Exchange and Correlation Effects. Phys. Rev.*, 1965. **140**(4A): p. A1133-A1138.
60. Wellendorff, J., T.L. Silbaugh, D. Garcia-Pintos, J.K. Nørskov, T. Bligaard, F. Studt, and C.T. Campbell, *A benchmark database for adsorption bond energies to transition metal surfaces and comparison to selected DFT functionals. Surf. Sci.*, 2015. **640**: p. 36-44.
61. Mallikarjun Sharada, S., T. Bligaard, A.C. Luntz, G.-J. Kroes, and J.K. Nørskov, *SBH10: A Benchmark Database of Barrier Heights on Transition Metal Surfaces. J. Phys. Chem. C*, 2017. **121**(36): p. 19807-19815.
62. Medvedev, M.G., I.S. Bushmarinov, J. Sun, J.P. Perdew, and K.A. Lyssenko, *Density functional theory is straying from the path toward the exact functional. Science*, 2017. **355**(6320): p. 49-52.
63. Schlegel, H.B., *Exploring potential energy surfaces for chemical reactions: An overview of some practical methods. J. Comput. Chem.*, 2003. **24**(12): p. 1514-1527.
64. Nitoń, P., A. Żywociński, M. Fiałkowski, and R. Hołyst, *A "nano-windmill" driven by a flux of water vapour: a comparison to the rotating ATPase. Nanoscale*, 2013. **5**(20): p. 9732-9738.
65. Campbell, C.T., *Future Directions and Industrial Perspectives Micro- and macro-kinetics: Their relationship in heterogeneous catalysis. Top. Catal.*, 1994. **1**(3): p. 353-366.
66. Campbell, C.T., *Finding the Rate-Determining Step in a Mechanism: Comparing DeDonder Relations with the "Degree of Rate Control". J. Catal.*, 2001. **204**(2): p. 520-524.
67. Stegelmann, C., A. Andreasen, and C.T. Campbell, *Degree of Rate Control: How Much the Energies of Intermediates and Transition States Control Rates. J. Am. Chem. Soc.*, 2009. **131**(23): p. 8077-8082.

2

CO₂ hydrogenation to methanol over Cd₄/TiO₂



Supported metal catalysts have shown to be efficient for CO₂ conversion due to their multifunctionality and high stability. Herein, we have combined density functional theory calculations with microkinetic modeling to investigate the catalytic reaction mechanisms of CO₂ hydrogenation to CH₃OH over a recently reported catalyst of Cd₄/TiO₂. Calculations reveal that the metal-oxide interface is the active center for CO₂ hydrogenation and methanol formation via the formate pathway dominates over the RWGS pathway. Microkinetic modeling demonstrated that formate species on the surface of Cd₄/TiO₂ is the relevant intermediate for the production of CH₃OH, and CH₂O[#] formation is the rate-determining step. These findings demonstrate the crucial role of the Cd-TiO₂ interface in controlling CO₂ reduction reactivity and CH₃OH selectivity.

2.1 Introduction

The increase of CO₂ concentration in the atmosphere is one of the major factors in global climate change. CO₂ capture and valorization have been considered as promising strategies to mitigate this problem [1, 2]. Using CO₂ as a feedstock to produce valuable chemicals not only can help to decrease dramatically the amount of CO₂ emitted into the atmosphere but also provide economic benefits [2, 3]. A large number of value-added chemicals can be produced from CO₂ via platform molecules such as CO, CH₄, and CH₃OH [4, 5]. Among these, CH₃OH is highly desirable because it is an important fuel as well as a starting feedstock for the production of more valuable chemical compounds [6]. Recently, two different approaches for CO₂ hydrogenation to CH₃OH have received a lot of attention: (1) electrochemical reduction and (2) thermochemical reduction [7]. The electrochemical CO₂ reduction offers the advantage that product distribution can be controlled by adjusting electrolyte, electrocatalyst, and applied voltage [8-11]. However, the selectivity, energetic efficiency, and electrode lifetime restrict its large-scale applications [10, 11]. Therefore, using the thermochemical approach to synthesize CH₃OH from CO₂ hydrogenation is more practical for potential industrial applications compared to the alternative electrochemical CO₂ reduction. It offers an opportunity to develop sustainable technologies and environmentally benign chemical processes since H₂, a reducing agent, can readily be obtained from renewable energy resources [1, 3].

Many studies have been devoted to creating new tailor-made CO₂ conversion catalysts with improved activity and selectivity to methanol, of which Cu/ZnO/Al₂O₃ catalyst has been industrialized [12, 13]. However, the disadvantages of low CH₃OH selectivity and the sintering of Cu and ZnO motivated the development of new Cu-based catalysts such as Cu/ZnO [14, 15], Cu/ZrO₂ [16, 17], and Cu/CeO₂ [18]. In these catalytic systems, it was found that H₂ molecule is dissociated at the Cu site and CO₂ is activated at the oxide surface, while the interface between Cu and metal oxide supports plays a crucial role for the stabilization of the reaction intermediate for CH₃OH formation [16, 17]. Besides Cu-based catalysts, various other materials have also been reported as promising catalysts for CO₂ hydrogenation to CH₃OH. For instance, Au [19-21], Pd [22-25], Re [26], ZnO [27], and In₂O₃ [28, 29] supported on oxides were reported to be active toward the production of CH₃OH under moderate conditions. Although many different types of catalysts have been reported, all of the active sites involved in the reaction have a common feature of multifunctionality in nature. Efficient cooperation between active sites of different

catalytic natures coupled in one heterogeneous catalyst plays a key role in eventual selective CH_3OH formation.

Regarding the reaction mechanism, typically, two different reaction pathways have been proposed for the hydrogenation of CO_2 to CH_3OH : (1) the reverse water-gas shift (RWGS) pathway and (2) the formate pathway. In the RWGS reaction, CO_2 is hydrogenated to form CO^* intermediate, which is then further hydrogenated to form CH_3OH . For the formate pathway, CH_3OH is produced via the formate (HCOO^*) intermediate [30, 31]. Most studies have suggested that the formate pathway is preferred over the RWGS pathway [13, 22, 32-35]. The main reason is that the binding strength of CO^* intermediate on these catalysts is quite weak, leading to the desorption of CO to the gas phase. However, on some other catalysts, such as Cu/TiO_2 , Cu/ZrO_2 , and Cu/CeO_x , CH_3OH was produced through CO^* intermediate due to the strong enough interaction between CO^* and catalyst [17, 18]. Therefore, the specific reaction pathway dominating methanol formation is system-dependent and should be investigated individually.

Recently, our experimental collaborators have discovered a promising reactivity of Cd/TiO_2 and CdTiO_3 catalysts in CO_2 hydrogenation to methanol [36]. It was found that Cd/TiO_2 catalyst exhibits a much higher catalytic CO_2 hydrogenation activity than the CdTiO_3 mixed oxide. To further identify the detailed reaction mechanism catalyzed by Cd/TiO_2 and clarify the functionalities of different types of active sites in this system, we constructed a Cd/TiO_2 model catalyst and investigated its catalytic activity towards CO_2 conversion to methanol with H_2 as a reductant. The key objective of this study is to explore the multiple-site cooperation effects on the catalyst reactivity by combining DFT calculation with microkinetic modeling.

2.2 Computational details

All DFT calculations have been performed using the Vienna Ab Initio Simulation Package (VASP) [37, 38]. The generalized gradient approximation (GGA) with Perdew-Burke-Ernzerhof (PBE) exchange and correlation functional was used to account for the exchange-correlation energy [38, 39]. The kinetic energy cutoff of the plane wave basis set was set to 400 eV. The threshold for energy convergence for each iteration was set to 10^{-5} eV. Geometries were assumed to be converged when forces on each atom were less than 0.05 eV/Å. Gaussian smearing of the population of partial occupancies with a width of 0.10 eV was used during iterative diagonalization of the Kohn-Sham Hamiltonian.

The bulk TiO_2 unit cell in the phase of anatase was firstly fully optimized. The optimized lattice vectors of $a = 3.799 \text{ \AA}$ $b = 3.799 \text{ \AA}$ $c = 9.716 \text{ \AA}$ have a good agreement with the experiment parameters [40]. For Cd_4/TiO_2 model, 1×3 and 2×4 supercells of anatase TiO_2 (101) surface with a vacuum space of 15 \AA were built for investigation of the reaction mechanism of H_2 dissociation and CO_2 hydrogenation, respectively. These slab models contain six titanium layers with the bottom three layers fixed while the rest was allowed to relax during the geometry optimization. The lattice parameters were fixed throughout the surface calculations. The nudged-elastic band method with the improved tangent estimate (CI-NEB) was used to determine the minimum energy path and to locate the transition state structure for each elementary reaction step [41]. The maximum energy geometry along the reaction path generated by the NEB method was further optimized using a quasi-Newton algorithm. Vibrational frequencies were calculated by determining the second derivatives of the Hessian matrix using the density functional perturbation theory as implemented in VASP 5.3.5. Transition state was confirmed by showing a single imaginary frequency corresponding to each reaction coordinate. Bader charge analysis was visualized by VESTA software [42]. Mean-field microkinetic modeling (MKM) is applied based on the DFT calculations of all elementary reaction steps. All MKM results are simulated by a home-made script.

2.3 Results

2.3.1 Cd_4/TiO_2 model rationalization

A cluster containing 4 Cd atoms (Cd_4) was selected as representative of the supported Cd nanoparticles on the TiO_2 surface since it was reported as the smallest Cd cluster featuring a magic number of Cd atoms [43]. In order to model the Cd_4/TiO_2 catalyst, two possible configurations of isolated Cd_4 cluster, i.e., a tetrahedron (T_d) and planar rhombus (C_{2v}) [44] were firstly optimized in the vacuum by using a large unit cell of $15 \times 15 \times 15 \text{ \AA}$, as shown in Figure 2.1. Then the so-obtained Cd_4 clusters were deposited and optimized on the (101) surface of anatase TiO_2 . It is found that the most stable configuration of the supported Cd_4 cluster on the (101) TiO_2 surface is a deformed planar geometry even though the tetrahedron is more stable in the gas phase. As shown in Figure 2.2, the Cd_4 (C_{2v}) cluster is slightly distorted upon the adsorption with one of the Cd atoms lying above the plane of the other three. The adsorption energy of Cd_4 over the surface is calculated to be -1.05 eV indicating a strong interaction between the metal cluster and the support of TiO_2 . Bader charge analysis demonstrates that the entire

Cd_4 cluster is $+1.48|e|$ charged, which indicates that the electrons are transferred from Cd_4 cluster to TiO_2 surface through metal-support interaction.

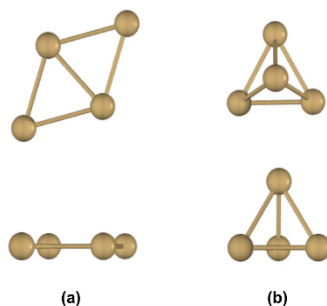


Figure 2.1 The optimized Cd_4 clusters: (a) planar rhombus and (b) tetrahedron. The clusters represent in top view (top) and side view (bottom).

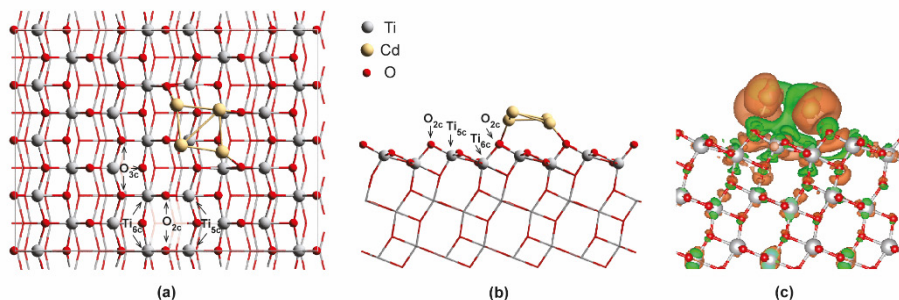


Figure 2.2 (a) Top view and (b) side view of $\text{Cd}_4/\text{TiO}_2(101)$ slab model. The O_{2c} and O_{3c} are twofold coordinated and threefold coordinated oxygen atoms, and the Ti_{5c} and Ti_{6c} are fivefold coordinated and sixfold coordinated titanium atoms on the surface of TiO_2 , respectively. (c) The electron density different plots upon the adsorption of Cd_4 cluster on TiO_2 surface. The orange and green regions represent electrons depletion and accumulation, respectively (isosurface value = $0.05 \text{ e}/\text{Bohr}^3$).

2.3.2 H_2 dissociation and H spillover

Many studies have proposed that activation and dissociation of an H_2 molecule take place at the metal-oxide interface [45–47]. In this work, six possible active sites of Cd_4/TiO_2 catalyst for the activation and dissociation of H_2 molecule was systematically studied. As shown in Figure 2.3, site A is on top of the supported Cd_4 cluster. Site B, C and D are at the interface of Cd_4/TiO_2 ($\text{Cd}\cdots\text{O}_{2c}$). Site E is located between two nearest O_{2c} atoms and site F is on top of bridging Ti_{5c} and O_{2c} atoms of TiO_2 surface. From Figure 2.3, it can be seen that heterolytic H_2 dissociation at the interface of Cd/TiO_2 is more preferable than the other sites. Among all interface

sites considered, H_2 dissociation over site C has the lowest activation barrier (0.39 eV). Homolytic dissociation of H_2 molecule over site A needs to overcome an activation barrier of 0.88 eV and generates two hydrides on the supported Cd_4 cluster. On the TiO_2 surface, both homolytic (site E) and heterolytic dissociation pathways (site F) exhibit very high activation barriers (1.74 and 2.25 eV), indicating that TiO_2 surface site is inactive for H_2 activation. This is in agreement with a previous theoretical study of H_2 dissociation on TiO_2 surfaces [48].

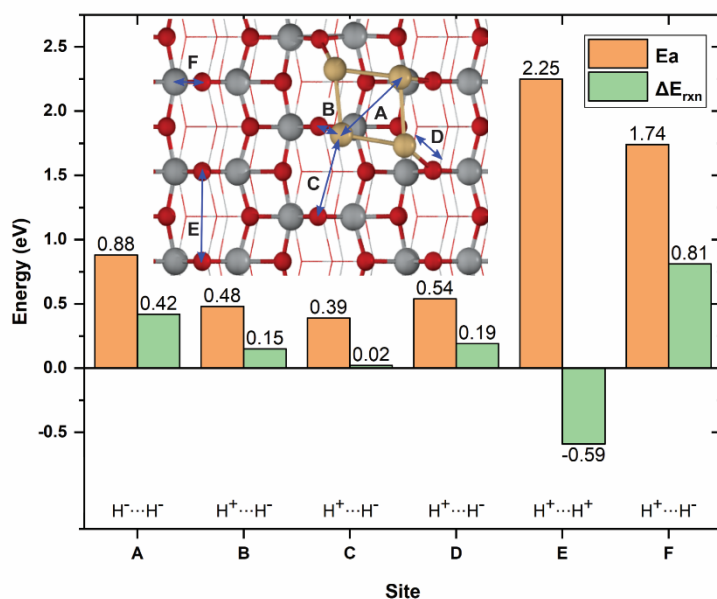


Figure 2.3. Activation energy (E_a) and reaction energy (ΔE_{rxn}) for H_2 dissociation at all possible active sites of Cd_4/TiO_2 catalyst.

After we figured out the most favorable active site for H_2 dissociation, the spillover process of the so-formed H^* on the surface of the Cd_4/TiO_2 is further studied. As shown in Figure 2.4, the migration of the H^* generated by H_2 dissociation at the interface (site C) from O_{2c} site to its neighboring O_{3c} site has an activation barrier of 0.73 eV. The other H^* species on the Cd_4 cluster can also spillover to the surface of TiO_2 with an activation barrier of 0.71 eV. H^* on O_{3c} site can also hop to another O_{2c} site next to it by overcoming a barrier of only 0.42 eV. The overall reaction is slightly endothermic. These results indicate that the activated H^* on the surface of the Cd_4/TiO_2 catalyst is rather dynamic and hydrogen migrations among different surface sites is thermodynamically and kinetically easy processes.

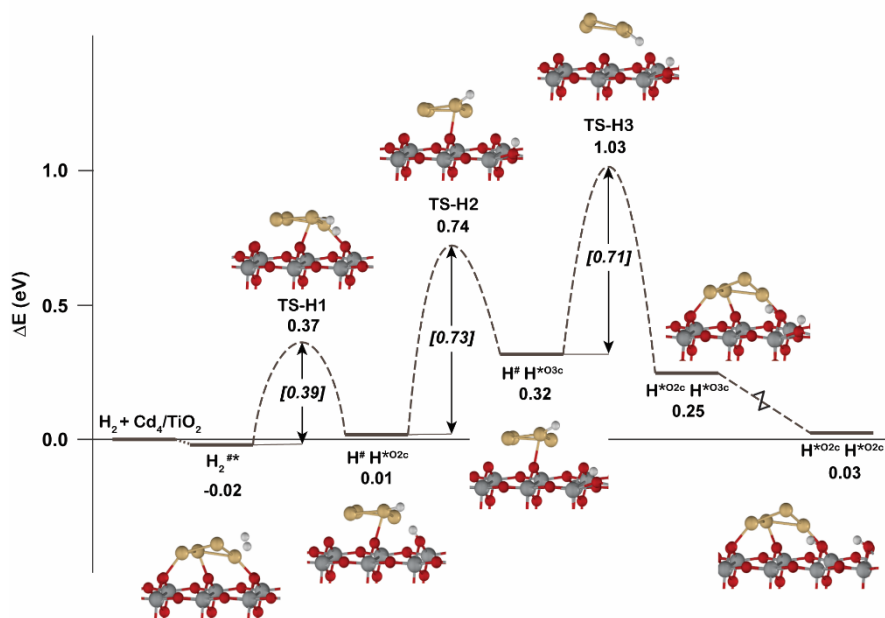


Figure 2.4 The reaction energy profiles for the H_2 dissociation followed by H migration and H spillover on Cd_4/TiO_2 catalyst

2.3.3 CO_2 hydrogenation to HCOOH and CO

In this section, the hydrogenation of CO_2 on Cd_4/TiO_2 catalyst will be discussed. Two main reaction pathways of CO_2 hydrogenation which have been intensively debated in the literature were studied: (1) methanol formation via the intermediate of HCOOH^* , and (2) methanol formation via the reversed water-gas shift (RWGS) pathway with CO as an intermediate. Note that the species with asterisk (*) and hash sign (#) are species that interact with TiO_2 surface and Cd_4 cluster of the Cd_4/TiO_2 catalyst, respectively.

Formate pathway: The reaction mechanisms of CO_2 hydrogenation to formate (HCOO^*) and formic acid (HCOOH^*) are shown in Figure 2.5. After heterolytic dissociation of H_2 at the interface of Cd_4/TiO_2 , a hydride coordinated to Cd ($\text{H}^\#$) and a proton bonded to O_{2c} site (H^*) are produced. CO_2 is adsorbed over the Ti_{5c} site nearby both H^* and $\text{H}^\#$ species. The adsorption energy is calculated to be -0.14 eV. Then CO_2 can be hydrogenated by the transfer of $\text{H}^\#$ from Cd_4 cluster to the C atom of CO_2 forming formate intermediate of HCOO^* . The activation barrier for this step is only 0.26 eV. Further protonation of HCOO^* to form formic acid (HCOOH^*) can be realized via two different reaction routes, either by protonation of monodentate HCOO^* intermediate to form *cis*- HCOOH^* (gray line in Figure 2.5), or protonation

of bidentate $\text{HCOO}^{*\#}$ intermediate which can be formed by structure rearrangement to form $\text{trans-HCOOH}^{*\#}$ (orange line in figure 2.5). The activation barriers of proton transfer for both routes are relatively low (0.22 and 0.41 eV), however, the configurational transformation of HCOO^* from monodentate coordination to bidentate coordination with both Ti_{5c} and Cd before protonation reaction is dramatically favorable. Another possible pathway for HCOOH^* formation is also identified with a small activation barrier of 0.15 eV, the so-called concerted reaction mechanism with CO_2 hydrogenation by both H^* and $\text{H}^\#$ in one step (green line in Figure 2.5).

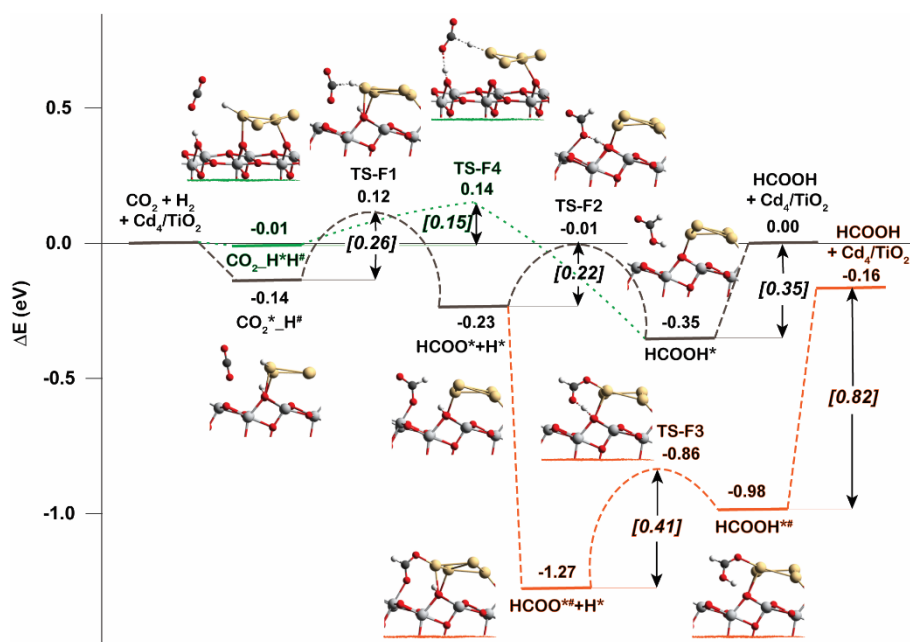


Figure 2.5. Reaction energy profiles for the CO_2 hydrogenation to HCOOH^* on Cd_4/TiO_2 catalyst. Green line is the concerted pathway. Gray line is the stepwise pathway via monodentate HCOO^* . Orange line is the stepwise pathway via bidentate HCOO^{**} . The species with asterisk (*) and hash sign (#) are species that interact with TiO_2 surface and Cd_4 cluster of the Cd_4/TiO_2 catalyst, respectively.

RWGS pathway: The RWGS reaction mechanism is initiated by CO_2 hydrogenation to form a carboxylate intermediate ($\text{HOCO}^\#$), from which CO is produced and can be further converted into methanol by continuous hydrogenation reactions. As shown in Figure 2.6, the reaction starts with the adsorption of CO_2 at the perimeter site of Cd_4 cluster after hydrogen spillover process. Then, the CO_2 can be protonated by the H^* on TiO_2 surface forming $\text{HOCO}^\#$. It is found that this reaction cannot occur directly due to the long distance

between CO_2 and H^* (4.93 Å). However, it can proceed with the assistance of an H_2O molecule which acts as a proton shuttle between H^* and CO_2 (blue line in Figure 2.6). The activation energy in this case is calculated to be 0.42 eV indicating that this process is feasible. Subsequent hydrogenation of the $\text{HOCO}^\#$ intermediate at its terminal OH group with the breaking of C-O bond produces $\text{CO}^\#$ and H_2O^* . This process requires overcoming an activation barrier of 0.35 eV. Finally, CO and H_2O can be desorbed from the catalyst with desorption barriers of 0.13 and 0.19 eV, respectively.

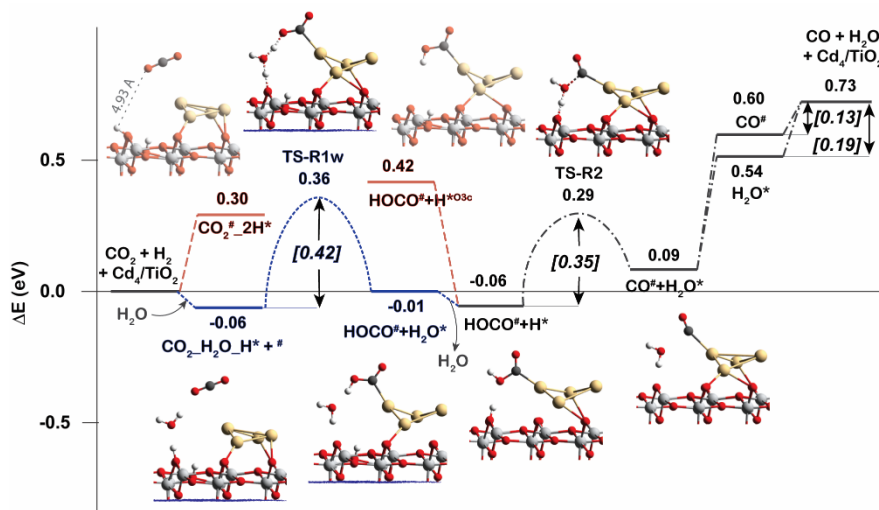


Figure 2.6 Reaction energy profiles for the CO_2 hydrogenation to CO on Cd_4/TiO_2 catalyst (RWGS pathway). Blue line is the reaction with the assistance of H_2O molecule.

Due to the unfavorable adsorption of CO_2 on the supported Cd_4 cluster, we also explored the CO_2 adsorption on a separate TiO_2 surface site without interaction with the Cd_4 cluster. The mechanisms of RWGS reaction on the TiO_2 surface are shown in Figure 2.7. In this case, this reaction starts with the adsorption of CO_2 on the TiO_2 surface after hydrogen spillover process. The adsorption energy of CO_2 is calculated to be -0.45 eV which is relatively stronger than that on supported Cd_4 cluster. The bent CO_2 geometry can be formed on the TiO_2 surface with an activation barrier of 0.44 eV. Then the adsorbed CO_2^* is directly hydrogenated to form HOCO^* without the H_2O mediator. The activation energy for this step is calculated to be 0.74 eV. The diffusion of the second H^* to the O_{3c} site close to the OH group of HOCO^* needs to overcome an activation barrier of 0.76 eV. After that, the cleavage of the C-O bond of HOCO^* intermediate to generate CO^* and OH^* species on the TiO_2 surface is rather difficult with an activation barrier of 1.86 eV.

However, the presence of H_2O molecule can again decrease this activation barrier to 0.94 eV with C-O bonding breaking and OH group hydrogenation occurring simultaneously.

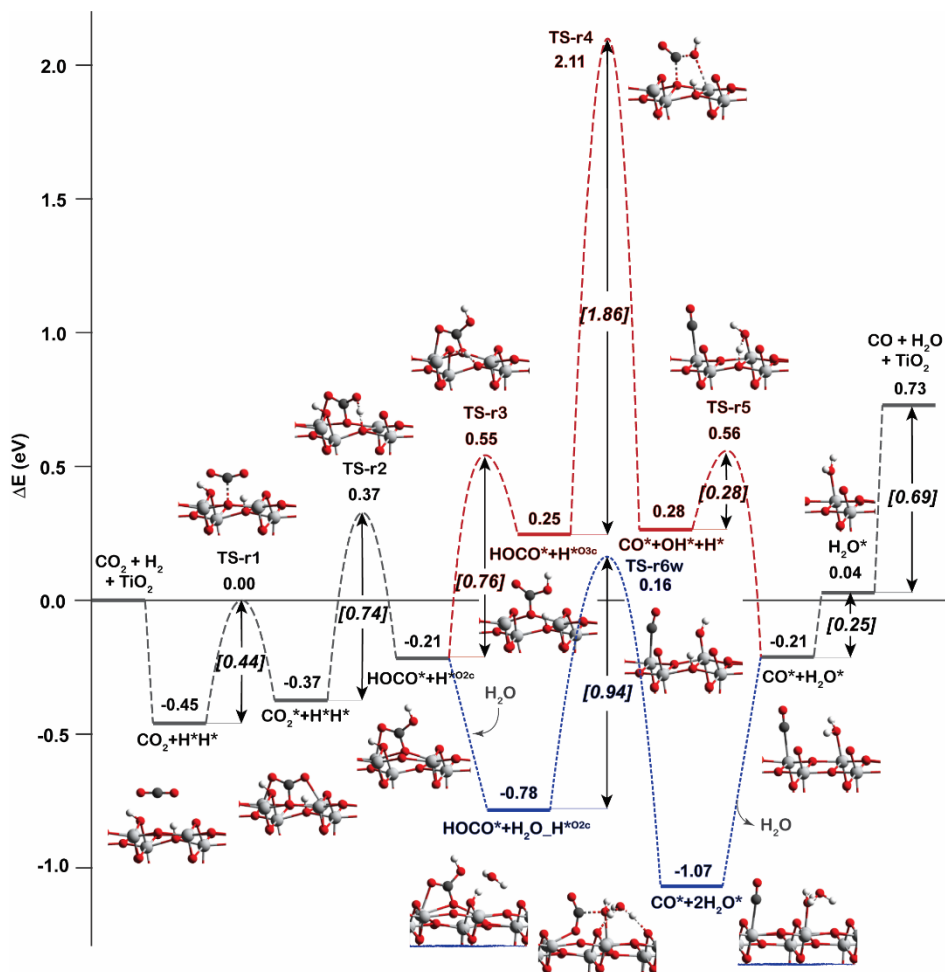


Figure 2.7 Reaction energy profiles for the CO₂ hydrogenation to CO on clean TiO₂ surface (RWGS pathway). Blue line is the reaction with the assistance of H₂O molecule.

It is found that H₂O molecule plays an important role as a proton shuttle to promote the most difficult reaction steps during the RWGS reactions taking place at both the interface and TiO₂ surface of Cd₄/TiO₂ catalyst. The hydrogenation reaction of CO₂ is the most difficult step for the reaction that occurred at the interface, while the C-O bond cleavage of HOCO* carboxylate intermediate is found to be the most difficult step for the reaction occurred at the TiO₂ surface. The

highest activation energy of the RWGS reaction that occurs at the interface of Cd₄ and TiO₂ surface (TS-R1w) is about two times lower than that of the other reaction route on the TiO₂ surface (TS-r6w). Therefore, it is concluded that the most preferable active site for the RWGS reaction is the interface of Cd₄/TiO₂ catalyst. Therefore, in the next section, the discussion of CH₃OH formation via CO* will only focus on the reaction route at the interface.

2.3.4 CH₃OH formation

In this section, we will discuss the reaction mechanism of CH₃OH formation from HCOOH* as well as CO* intermediates generated from the formate and the RWGS reaction pathways. The results are shown in Figure 2.8. Totally four elementary hydrogenation reaction steps are involved for CH₃OH formation from CO i.e. CO* → HCO*, HCO* → CH₂O*, CH₂O* → CH₃O* and CH₃O* → CH₃OH. The activation barrier for CO hydrogenation to form HCO* is 0.32 eV by H[#] on Cd₄ cluster. The next step of dissociative adsorption of H₂ on top of HCO* intermediate generating CH₂O* and H[#] species has an activation barrier of 1.10 eV. Subsequent CH₃O* formation by CH₂O* hydrogenation is a barrierless process with a reaction energy of -1.40 eV. Finally, the CH₃OH is formed by hydrogenation of CH₃O* intermediate with an activation barrier of 0.48 eV. In addition, CH₃OH can be produced by the hydrogenolysis of CH₃O* (green line in Figure 2.8). The activation energy of this step is only 0.04 eV lower than that of the CH₃O* hydrogenation step. These results imply that both CH₃O* hydrogenolysis and CH₃O* hydrogenation coexist in the formation of CH₃OH.

Alternatively, CH₃OH can also be formed from HCOOH* (blue line in Figure 2.8). The initial step is the hydrogenation of HCOOH* to produce formaldehyde (CH₂O*) and an OH* species (CH₂O* + OH* + H*). The activation energy of this step is calculated to be 0.65 eV. Then, the OH* is protonated to form H₂O and regenerate a vacant interfacial active site on the surface. In the next step, after another H₂ molecule is dissociated at the interface, the CH₃OH can be formed by two successive hydrogenation steps from CH₂O*, which is the same process as the reactions via the RWGS pathway.

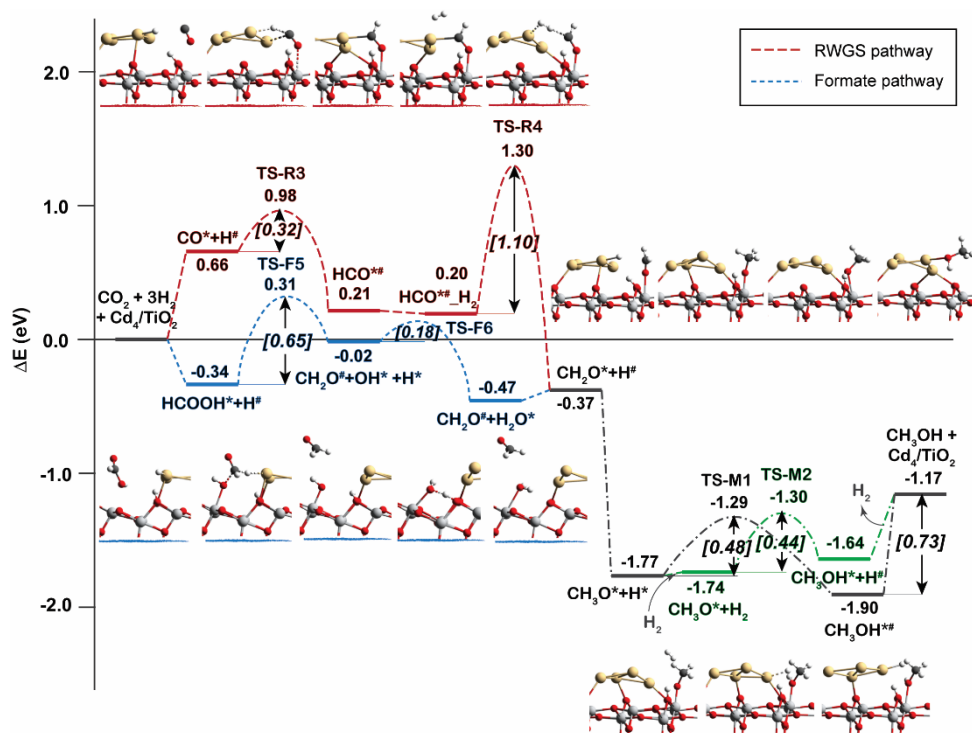


Figure 2.8 Reaction energy profiles for the production of CH_3OH from CO and HCOOH .

To summarize, Figure 2.9 gives a schematic representation of the whole DFT reaction mechanism identified in this work, and the whole reaction pathways of CO_2 hydrogenation to CH_3OH on Cd_4/TiO_2 catalyst are shown in Figure 2.10. It can be seen that the formate pathway dominates over the RWGS pathway for the production of CH_3OH from CO_2 and H_2 . The formation of CH_2O^* intermediate is found to be the most difficult reaction step for CH_3OH production from both RWGS and formate reaction routes.

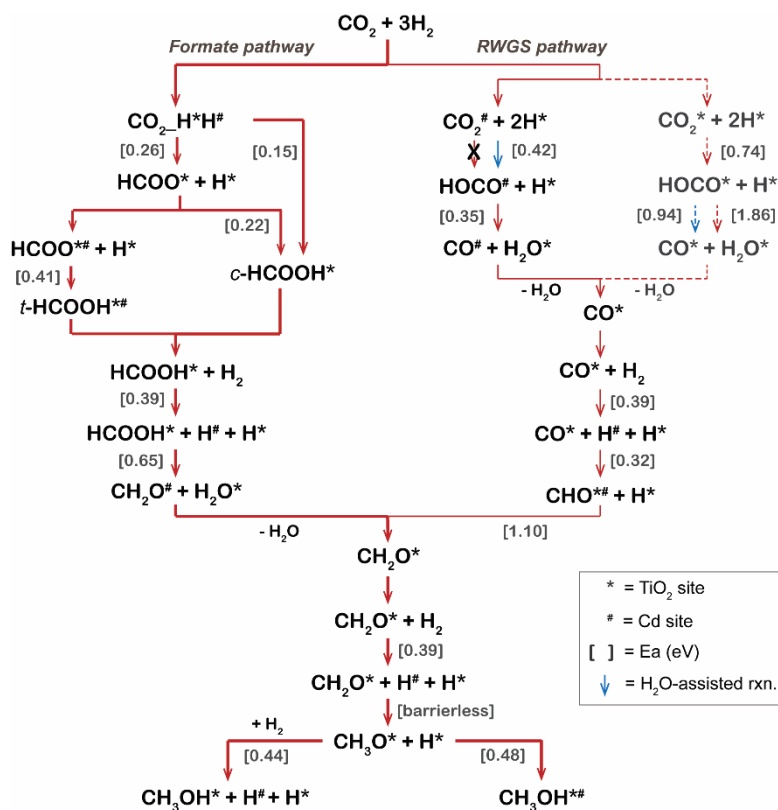


Figure 2.9 A schematic representation of the whole reaction mechanism for CO_2 hydrogenation to CH_3OH on Cd_4/TiO_2 catalyst. Numbers in parentheses represent activation energies in eV. Solid lines and dash lines represent reactions at the interface and TiO_2 surface, respectively.

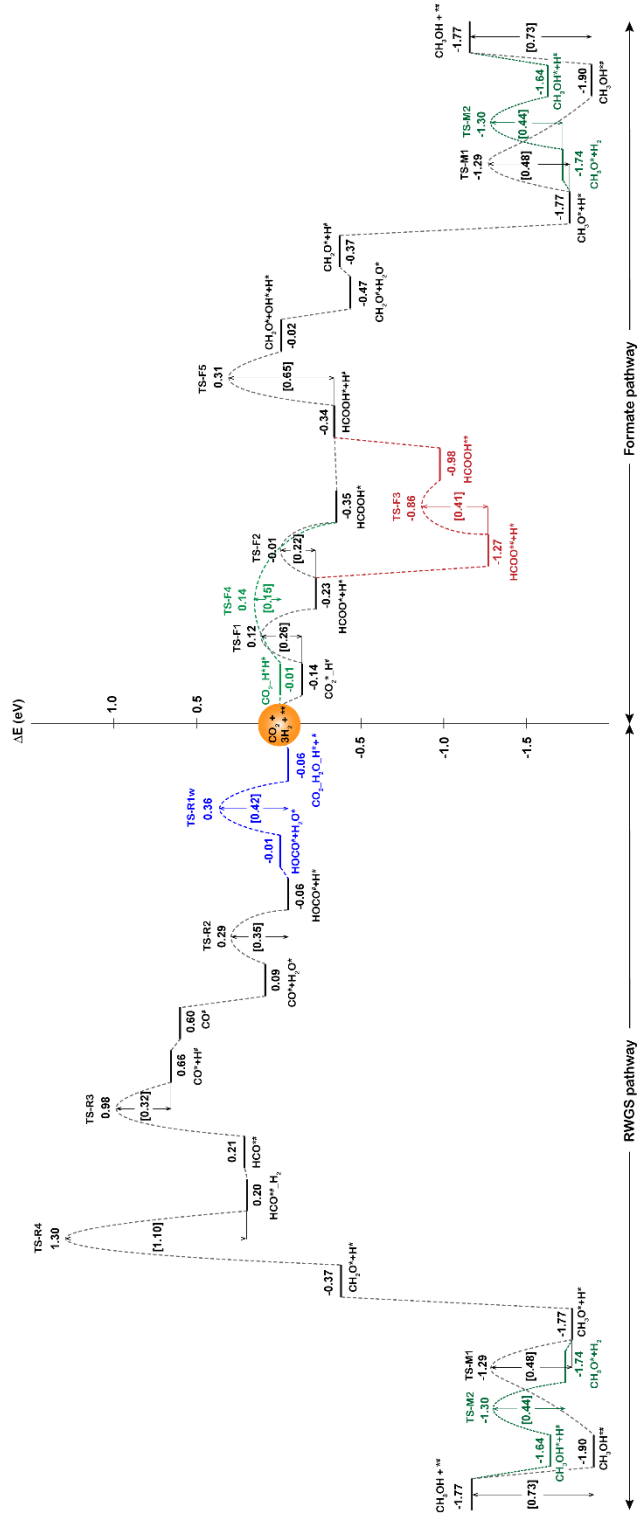


Figure 2.10 The complete reaction energy profiles for the competing mechanisms of the CO_2 hydrogenation to CH_3OH on Cd_4/TiO_2 catalyst

2.3.5 Microkinetic modeling

All considered elementary steps of the CO_2 hydrogenation to CH_3OH on the interface sites of the Cd_4/TiO_2 catalyst, and corresponding activation energies are listed in Table 2.1. The MKM is performed using a dual-site model representing TiO_2 (*) and Cd (#) sites on Cd_4/TiO_2 catalyst, respectively. The ratio between the number of * and # sites is 0.5:0.5. The reaction rate, surface coverages, and degree of rate control (DRC) are calculated under the following steady-state reaction conditions: total pressure = 2 MPa., $\text{H}_2/\text{CO}_2 = 3:1$, temperature = 270–310°C. The apparent activation energy (E_{app}) is determined from the slope of the Arrhenius plot, as shown in Figure 2.11a. The E_{app} for the CH_3OH formation is calculated to be 1.46 eV, while that for the CO formation is computed at 4.10 eV, which is due to the incomplete representation of the catalyst system in the MKM model. Our calculations suggest that the direct RWGS can take place over TiO_2 surface with a barrier of around 2 eV, whereas the presence of H_2O in the system can help establish the lower-energy path for the CO formation at the interface sites. However, in the simulations, the water coverage at such sites was very low, resulting in negligible CO formation and, as a result, the unrealistically high apparent activation barrier. The introduction of additional H_2O in the system reduced the barrier for the RWGS path to the expected value of 0.77 eV that is close to the overall barrier for the CO desorption via the H_2O -assisted reaction path. The presence of water did not affect the kinetic parameters for CH_3OH production. The latter path dominated all MKM simulations in line with the experimental observations of the high selectivity to methanol over Cd/TiO_2 catalyst [36]. Therefore, we focused specifically on the methanol production path in further analysis of the MKM simulation results.

Table 2.1 Summary of elementary reaction steps and activation energies from DFT calculations used for microkinetic modeling. Ea-f and Ea-b are activation energy for forward and backward reactions, respectively. * and # represent TiO₂ and Cd sites on Cd₄/TiO₂ catalyst.

		Elementary reaction step	Ea-f (eV)	Ea-b
H₂ dissociation	R0:	$[H_2] + [*] + [\#] \leftrightarrow [H_2^{* \#}]$	0.00	0.02
	R1:	$[H_2^{* \#}] \leftrightarrow [H^*] + [H^\#]$	0.39	0.38
	R2:	$[H^\#] + [*] \leftrightarrow [H^*] + [\#]$	0.71	0.78
Formate pathway	R3:	$[CO_2] + [H^*] + [H^\#] \leftrightarrow [CO_2-H^*H^\#]$	0.00	0.01
	R4:	$[CO_2-H^*H^\#] \leftrightarrow [HCOOH^*] + [\#]$	0.15	0.49
	R5:	$[CO_2] + [*] + [H^\#] \leftrightarrow [CO_2^*-H^\#]$	0.00	0.14
	R6:	$[CO_2^*-H^\#] \leftrightarrow [HCOO^*] + [\#]$	0.26	0.35
	R7:	$[HCOO^*] + [H^*] \leftrightarrow [HCOOH^*] + [*]$	0.22	0.34
	R8:	$[HCOO^*] + [\#] \leftrightarrow [HCOO^{* \#}]$	0.00	1.04
	R9:	$[HCOO^{* \#}] + [H^*] \leftrightarrow [HCOOH^{* \#}] + [*]$	0.41	0.12
	R10:	$[HCOOH^{* \#}] \leftrightarrow [HCOOH^*] + [\#]$	0.63	0.00
	R11:	$[HCOOH^*] + [H^\#] \leftrightarrow [CH_2O^\#] + [OH^*]$	0.65	0.33
	R12:	$[CH_2O^\#] + [*] \leftrightarrow [CH_2O^*] + [\#]$	0.00	0.44
	R13:	$[OH^*] + [H^*] \leftrightarrow [H_2O^*] + [*]$	0.18	0.63
	R14:	$[H_2O] + [*] \leftrightarrow [H_2O^*]$	0.00	0.57
CH₃OH formation	R15:	$[CH_2O^*] + [H^\#] \leftrightarrow [CH_3O^*] + [\#]$	0.00	1.40
	R16:	$[CH_3O^*] + [H^*] + [\#] \leftrightarrow [CH_3OH^{* \#}] + [*]$	0.48	0.61
	R17:	$[CH_3OH] + [*] + [\#] \leftrightarrow [CH_3OH^{* \#}]$	0.00	0.73
RWGS pathway	R18:	$[H_2O] + [H^*] \leftrightarrow [H_2O-H^*]$	0.00	0.26
	R19:	$[CO_2] + [H_2O^*] + [H_2O-H^*] \leftrightarrow$	0.00	0.06
	R20:	$[CO_2-H_2O-H^*] + [\#] \leftrightarrow [HOCO^\#] +$	0.42	0.37
	R21:	$[H_2O] + [*] \leftrightarrow [HOH^*]$	0.00	0.19
	R22:	$[HOCO^\#] + [H^*] \leftrightarrow [CO^\#] + [HOH^*]$	0.35	0.20
	R23:	$[CO] + [\#] \leftrightarrow [CO^\#]$	0.00	0.13
	R24:	$[CO] + [*] \leftrightarrow [CO^*]$	0.00	0.03
	R25:	$[CO^*] + [H^\#] \leftrightarrow [HCO^{* \#}]$	0.32	0.77
	R26:	$[HCO^{* \#}] + [H_2] \leftrightarrow [HCO^{* \#}-H_2]$	0.00	0.01
	R27:	$[HCO^{* \#}-H_2] \leftrightarrow [CH_2O^*] + [H^\#]$	1.10	1.67
CH₃O* to CH₃OH*	R28:	$[CH_3O^*] + [H_2] + [\#] \leftrightarrow [CH_3OH^*] + [H^\#]$	0.44	0.34
	R29:	$[CH_3OH] + [*] \leftrightarrow [CH_3OH^*]$	0.00	0.46

Figure 2.11b shows that the $\text{HCOO}^{*\#}$ has the highest surface coverage ($\sigma \approx 0.5$), indicating the formation of this intermediate is the resting state of the overall reaction. This result is consistent with the experimental in-situ IR observation [36]. DRC analysis (Figure 2.11c) shows that the conversion of HCOOH^* to $\text{CH}_2\text{O}^{\#}$ (R11), the most difficult reaction step of the formate pathway, is also the rate-determining step. This result demonstrates that formate pathway dominates over RWGS pathway for the CO_2 hydrogenation to CH_3OH on the surface of Cd/TiO_2 catalyst. In addition, it was found that the H_2 dissociation reaction step (R1 in Table 1) has only a minor influence on the overall reaction rate. The effect of H_2 and CO_2 partial pressure on the reaction rate is also investigated by MKM, as shown in Figure 2.11d. These results indicate that increasing H_2 partial pressure can significantly enhance the methanol production rate, which, in turn, is not affected by the CO_2 partial pressure.

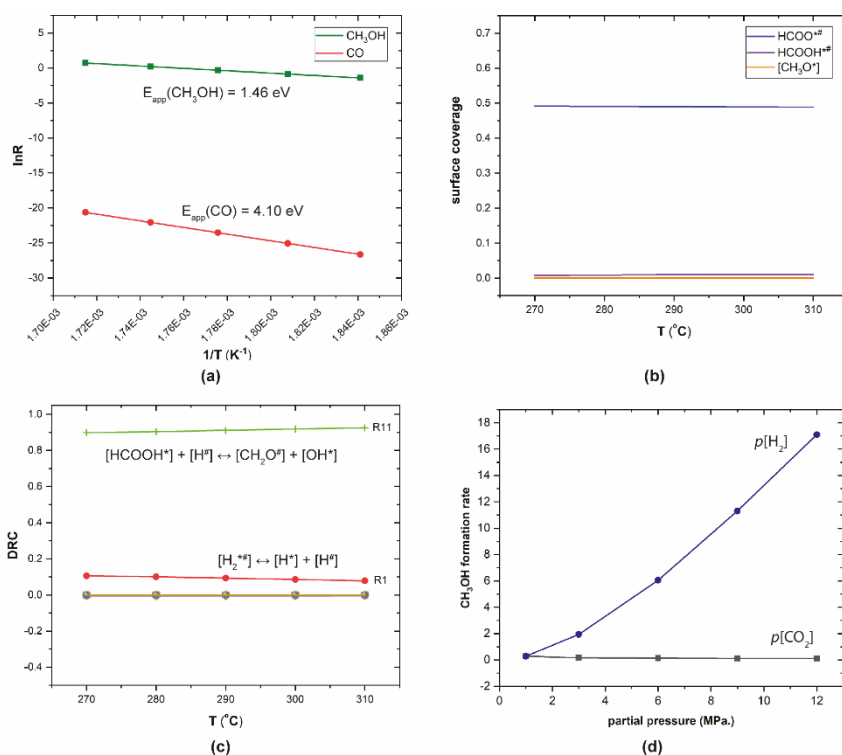


Figure 2.11 Results of the microkinetic modeling for the CO_2 hydrogenation on Cd/TiO_2 catalyst. (a) is product formation rates as a function of temperature ($T=270\text{--}310^{\circ}\text{C}$) and the calculated apparent activation energy (E_a). (b) is surface coverages of major surface intermediates at $270\text{--}310^{\circ}\text{C}$. (c) is degree of rate control analysis at $270\text{--}310^{\circ}\text{C}$. (d) is the partial pressure dependence of the CH_3OH formation rate at 290°C . The partial pressure of another reactant is fixed as 1 MPa.

2.4 Conclusion

In summary, the reaction mechanisms of CO₂ hydrogenation to methanol over TiO₂-supported Cd catalyst have been investigated computationally by a combination of DFT and MKM modelling approaches. It is proposed that the interface between the Cd₄ cluster and the support of TiO₂ plays a key role for H₂ dissociation as well as preactivation of CO₂. H₂ dissociation and CO₂ activation are energetically more favorable at the Cd-TiO₂ interface than that at bare TiO₂ surface and Cd cluster. Both CO₂ hydrogenation reactions to formate and CO are remarkably facilitated by the synergy between H⁻ on Cd and H⁺ on TiO₂ surface (Figure 2.5, formate pathway; Figure 2.6, RWGS pathway). In contrast, CO₂ conversion to CH₃OH on bare TiO₂ is very difficult compared to the Cd/TiO₂ interface. Cd-TiO₂ interface is crucial for stabilizing various reaction intermediates and promoting the rate-determining step of formaldehyde formation identified by DFT and MKM. All these mechanism results indicate that the multifunctionality of Cd/TiO₂ interface, including Lewis acids of metals and Lewis base of surface oxygen, is of great importance accounting for the outstanding catalytic activity of Cd/TiO₂ material. Water molecules produced from the reaction or present in the reaction system can dramatically facilitate the most difficult reaction steps of RWGS reaction. However, formate is identified to be the relevant intermediate for CO₂ hydrogenation to methanol, with formaldehyde formation being the rate-limiting reaction step. Our results demonstrate that Cd/TiO₂ can be a promising candidate for valorization of CO₂ to produce methanol and the multifunctionality of the metal-support interface is a crucial aspect for rational design of CO₂ hydrogenation catalyst.

References

1. Wang, W., S. Wang, X. Ma, and J. Gong, *Recent advances in catalytic hydrogenation of carbon dioxide*. *Chem Soc Rev*, 2011. **40**(7): p. 3703-27.
2. Alvarez, A., A. Bansode, A. Urakawa, A.V. Bavykina, T.A. Wezendonk, M. Makkee, J. Gascon, and F. Kapteijn, *Challenges in the Greener Production of Formates/Formic Acid, Methanol, and DME by Heterogeneously Catalyzed CO₂ Hydrogenation Processes*. *Chem Rev*, 2017. **117**(14): p. 9804-9838.
3. Pérez-Fortes, M., J.C. Schöneberger, A. Boulamanti, and E. Tzimas, *Methanol synthesis using captured CO₂ as raw material: Techno-economic and environmental assessment*. *Appl. Energy*, 2016. **161**: p. 718-732.

4. Li, W., H. Wang, X. Jiang, J. Zhu, Z. Liu, X. Guo, and C. Song, *A short review of recent advances in CO₂ hydrogenation to hydrocarbons over heterogeneous catalysts*. *RSC Adv.*, 2018. **8**: p. 7651-7669.
5. Ye, R.-P., W.G. Jie Ding, M.D. Argyle, Q. Zhong, Y. Wang, C.K. Russell, Z. Xu, A.G. Russell, Q. Li, M. Fan, and Y.-G. Yao, *CO₂ hydrogenation to high-value products via heterogeneous catalysis*. *Nat. Commun.*, 2019. **10**: p. 5698.
6. Ghasemzadeh, K., S.M. Sadati Tilebon, M. Nasirinezhad, and A. Basile, *Economic Assessment of Methanol Production*, in *Methanol*. 2018. p. 613-632.
7. Albo, J., M. Alvarez-Guerra, P. Castaño, and A. Irabien, *Towards the electrochemical conversion of carbon dioxide into methanol*. *Green Chem.*, 2015. **17**(4): p. 2304-2324.
8. Yang, W., K. Dastafkan, C. Jia, and C. Zhao, *Design of Electrocatalysts and Electrochemical Cells for Carbon Dioxide Reduction Reactions*. *Adv. Mater. Technol.*, 2018. **3**(9): p. 1700377.
9. Qiao, J., Y. Liu, F. Hong, and J. Zhang, *A review of catalysts for the electroreduction of carbon dioxide to produce low-carbon fuels*. *Chem. Soc. Rev.*, 2014. **43**(2): p. 631-75.
10. Khezri, B., A.C. Fisher, and M. Pumera, *CO₂ reduction: the quest for electrocatalytic materials*. *J. Mater. Chem. A*, 2017. **5**(18): p. 8230-8246.
11. Sun, Z., T. Ma, H. Tao, Q. Fan, and B. Han, *Fundamentals and Challenges of Electrochemical CO₂ Reduction Using Two-Dimensional Materials*. *Chem*, 2017. **3**(4): p. 560-587.
12. Behrens, M., F. Studt, I. Kasatkin, S. Kühl, M. Hävecker, F. Abild-Pedersen, S. Zander, F. Girgsdies, P. Kurr, B.-L. Knief, M. Tovar, R.W. Fischer, J.K. Nørskov, and R. Schlögl, *The Active Site of Methanol Synthesis over Cu-ZnO-Al₂O₃ Industrial Catalysts*. *Science*, 2012. **336**: p. 893-897.
13. Kattel, S., P.J. Ramírez, J.G. Chen, J.A. Rodriguez, and P. Liu, *Active sites for CO₂ hydrogenation to methanol on Cu/ZnO catalysts*. *Science*, 2017. **355**(6331): p. 1296-1299.
14. Wu, J., M. Saito, M. Takeuchi, and T. Watanabe, *The stability of Cu/ZnO-based catalysts in methanol synthesis from a CO₂-rich feed and from a CO-rich feed*. *Appl. Catal. A*, 2001. **218**: p. 235-240.
15. Hu, X., W. Qin, Q. Guan, and W. Li, *The Synergistic Effect of CuZnCeO_x in Controlling the Formation of Methanol and CO from CO₂ Hydrogenation*. *ChemCatChem*, 2018. **10**(19): p. 4438-4449.
16. Larmier, K., W.C. Liao, S. Tada, E. Lam, R. Verel, A. Bansode, A. Urakawa, A. Comas-Vives, and C. Coperet, *CO₂-to-Methanol Hydrogenation on Zirconia-Supported Copper Nanoparticles: Reaction Intermediates and the Role of the Metal-Support Interface*. *Angew. Chem. Int. Ed.*, 2017. **56**(9): p. 2318-2323.

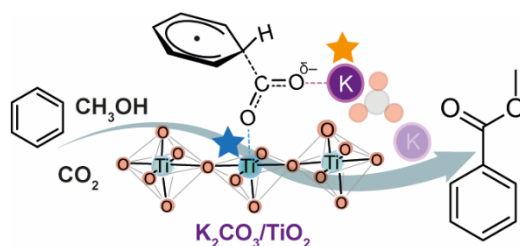
17. Kattel, S., B. Yan, Y. Yang, J.G. Chen, and P. Liu, *Optimizing Binding Energies of Key Intermediates for CO₂ Hydrogenation to Methanol over Oxide-Supported Copper*. *J. Am. Chem. Soc.*, 2016. **138**(38): p. 12440-50.
18. Graciani, J., K. Mudiyansele, F. Xu, A.E. Baber, J. Evans, S.D. Senanayake, D.J. Stacchiola, P.L. Hrbek, J.F. Sanz, and J.A. Rodriguez, *Highly active copper-ceria and copper-ceria-titania catalysts for methanol synthesis from CO₂*. *Science*, 2014. **345**: p. 546-550.
19. Vourros, A., I. Garagounis, V. Kyriakou, S.A.C. Carabineiro, F.J. Maldonado-Hódar, G.E. Marnellos, and M. Konsolakis, *Carbon dioxide hydrogenation over supported Au nanoparticles: Effect of the support*. *J. CO₂ Util.*, 2017. **19**: p. 247-256.
20. Hartadi, Y., D. Widmann, and R.J. Behm, *Methanol formation by CO₂ hydrogenation on Au/ZnO catalysts – Effect of total pressure and influence of CO on the reaction characteristics*. *J. Catal.*, 2016. **333**: p. 238-250.
21. Rodriguez, J.A., J. Evans, L. Feria, A.B. Vidal, P. Liu, K. Nakamura, and F. Illas, *CO₂ hydrogenation on Au/TiC, Cu/TiC, and Ni/TiC catalysts: Production of CO, methanol, and methane*. *J. Catal.*, 2013. **307**: p. 162-169.
22. Malik, A.S., S.F. Zaman, A.A. Al-Zahrani, M.A. Daous, H. Driss, and L.A. Petrov, *Development of highly selective PdZn/CeO₂ and Ca-doped PdZn/CeO₂ catalysts for methanol synthesis from CO₂ hydrogenation*. *Appl. Catal. A: Gen.*, 2018. **560**: p. 42-53.
23. Snider, J.L., V. Streibel, M.A. Hubert, T.S. Choksi, E. Valle, D.C. Upham, J. Schumann, M.S. Dwyer, A. Gallo, F. Abild-Pedersen, and T.F. Jaramillo, *Revealing the Synergy between Oxide and Alloy Phases on the Performance of Bimetallic In–Pd Catalysts for CO₂ Hydrogenation to Methanol*. *ACS Catal.*, 2019. **9**(4): p. 3399-3412.
24. Wu, D., K. Deng, B. Hu, Q. Lu, G. Liu, and X. Hong, *Plasmon-Assisted Photothermal Catalysis of Low-Pressure CO₂ Hydrogenation to Methanol over Pd/ZnO Catalyst*. *ChemCatChem*, 2019. **11**(6): p. 1598-1601.
25. Jiang, F., S. Wang, B. Liu, J. Liu, L. Wang, Y. Xiao, Y. Xu, and X. Liu, *Insights into the Influence of CeO₂ Crystal Facet on CO₂ Hydrogenation to Methanol over Pd/CeO₂ Catalysts*. *ACS Catal.*, 2020. **10**(19): p. 11493-11509.
26. Ting, K.W., T. Toyao, S.M.A.H. Siddiki, and K.-i. Shimizu, *Low-Temperature Hydrogenation of CO₂ to Methanol over Heterogeneous TiO₂-Supported Re Catalysts*. *ACS Catal.*, 2019. **9**(4): p. 3685-3693.
27. Wang, J., G. Li, Z. Li, C. Tang, Z. Feng, H. An, H. Liu, T. Liu, and C. Li, *A highly selective and stable ZnO-ZrO₂ solid solution catalyst for CO₂ hydrogenation to methanol*. *Sci. Adv.*, 2017. **3**(10): p. e1701290.
28. Yang, C., C. Pei, R. Luo, S. Liu, Y. Wang, Z. Wang, Z.-J. Zhao, and J. Gong, *Strong Electronic Oxide–Support Interaction over In₂O₃/ZrO₂ for Highly*

- Selective CO₂ Hydrogenation to Methanol*. *J. Am. Chem. Soc.*, 2020. **142**(46): p. 19523-19531.
29. Dang, S., B. Qin, Y. Yang, H. Wang, J. Cai, Y. Han, S. Li, P. Gao, and Y. Sun, *Rationally designed indium oxide catalysts for CO₂ hydrogenation to methanol with high activity and selectivity*. *Sci. Adv.*, 2020. **6**(25): p. eaaz2060.
30. Li, Y., S.H. Chan, and Q. Sun, *Heterogeneous catalytic conversion of CO₂: a comprehensive theoretical review*. *Nanoscale*, 2015. **7**(19): p. 8663-8683.
31. Kattel, S., P. Liu, and J.G. Chen, *Tuning Selectivity of CO₂ Hydrogenation Reactions at the Metal/Oxide Interface*. *J. Am. Chem. Soc.*, 2017. **139**(29): p. 9739-9754.
32. Dou, M., M. Zhang, Y. Chen, and Y. Yu, *Theoretical study of methanol synthesis from CO₂ and CO hydrogenation on the surface of ZrO₂ supported In₂O₃ catalyst*. *Surf. Sci.*, 2018. **672-673**: p. 7-12.
33. Wang, J., G. Li, Z. Li, C. Tang, Z. Feng, H. An, H. Liu, T. Liu, and C. Li, *A highly selective and stable ZnO-ZrO₂ solid solution catalyst for CO₂ hydrogenation to methanol*. *Sci Adv*, 2018. **3**(10): p. e1701290.
34. Ye, J., C. Liu, D. Mei, and Q. Ge, *Active Oxygen Vacancy Site for Methanol Synthesis from CO₂ Hydrogenation on In₂O₃(110): A DFT Study*. *ACS Catal.*, 2013. **3**(6): p. 1296-1306.
35. Liu, C., B. Yang, E. Tyo, S. Seifert, J. DeBartolo, B. von Issendorff, P. Zapol, S. Vajda, and L.A. Curtiss, *Carbon Dioxide Conversion to Methanol over Size-Selected Cu₄ Clusters at Low Pressures*. *J. Am. Chem. Soc.*, 2015. **137**(27): p. 8676-9.
36. Wang, J., J. Meeprasert, Z. Han, H. Wang, Z. Feng, C. Tang, F. Sha, S. Tang, G. Li, and C.L. E.A. Pidko, *Highly dispersed Cd cluster supported on TiO₂ as an efficient catalyst for CO₂ hydrogenation to methanol*. *Chin. J. Catal.*, 2022. **43**(3): p. 761-770.
37. Kresse, G. and J. Furthmüller, *Efficiency of ab-initio total energy calculations for metals and semiconductors using a plane-wave basis set*. *Comput. Mater. Sci.*, 1996. **6**(1): p. 15-50.
38. Kresse, G. and J. Furthmüller, *Efficient iterative schemes for ab initio total-energy calculations using a plane-wave basis set*. *Phys. Rev. B*, 1996. **54**(16): p. 11169-11186.
39. Perdew, J.P., K. Burke, and M. Ernzerhof, *Generalized Gradient Approximation Made Simple*. *Phys. Rev. Lett.*, 1996. **77**(18): p. 3865-3868.
40. Diebold, U., *The surface science of titanium dioxide*. *Surf. Sci. Rep.*, 2003. **48**(5): p. 53-229.
41. Henkelman, G., B.P. Uberuaga, and H. Jónsson, *A climbing image nudged elastic band method for finding saddle points and minimum energy paths*. *J. Chem. Phys.*, 2000. **113**(22): p. 9901-9904.

42. Momma, K. and F. Izumi, *VESTA 3 for three-dimensional visualization of crystal, volumetric and morphology data*. *J. Appl. Crystallogr.*, 2011. **44**(6): p. 1272-1276.
43. Kohaut, S. and M. Springborg, *Growth patterns and structural motifs of cadmium clusters with up to 60 atoms: disordered or not?* *Phys Chem Chem Phys*, 2016. **18**(41): p. 28524-28537.
44. Zhao, J., *Density-functional study of structures and electronic properties of Cd clusters*. *Phys. Rev. A*, 2001. **64**(4): p. 043204.
45. Boronat, M., F. Illas, and A. Corma, *Active Sites for H₂ Adsorption and Activation in Au-TiO₂ and the Role of the Support*. *J. Phys. Chem. A*, 2009. **113**: p. 3750-3757.
46. Wan, W., X. Nie, M.J. Janik, C. Song, and X. Guo, *Adsorption, Dissociation, and Spillover of Hydrogen over Au/TiO₂ Catalysts: The Effects of Cluster Size and Metal-Support Interaction from DFT*. *J. Phys. Chem. C*, 2018. **122**(31): p. 17895-17916.
47. Sun, K., M. Kohyama, S. Tanaka, and S. Takeda, *A Study on the Mechanism for H₂ Dissociation on Au/TiO₂ Catalysts*. *J. Phys. Chem. C*, 2014. **118**(3): p. 1611-1617.
48. Hu, G., Z. Wu, and D.-e. Jiang, *First Principles Insight into H₂ Activation and Hydride Species on TiO₂ Surfaces*. *J. Phys. Chem. C*, 2018. **122**(35): p. 20323-20328.

3

Mechanistic investigation of benzene esterification with CO₂ and CH₃OH by K₂CO₃/TiO₂



Potassium carbonate dispersed over defective TiO₂ support (K₂CO₃/TiO₂) is an efficient catalyst for benzene esterification with CO₂ and CH₃OH. Density functional theory calculations reveal that this unique catalytic reactivity originates from the cooperation of the Ti³⁺/K⁺ surface sites. K₂CO₃ promotor steers the stabilization of surface intermediates thus preventing catalyst deactivation.

This chapter has been published in ChemComm, 2021, 57, 7890-7893.

3.1 Introduction

CO₂ conversion into valuable chemicals has received much attention due to the environmental concerns associated with the growing atmospheric concentrations of greenhouse gases. Many efforts have been invested to develop a carbon-neutral economic system by recycling the carbon resource of CO₂ from industrial emissions to the production of chemicals [1-3]. The carboxylation of aromatics by CO₂ is one of the attractive routes for the valorization of CO₂, because the produced aromatic carboxylic acids and their derivatives can serve as important chemical feedstocks [4, 5]. Conventionally, such a carboxylation coupling reaction is carried out in the presence of strong base or Lewis acids such as NaH [6], AlCl₃ [4], and AlBr₃ [7]. The strong base is needed to cleave the C-H bond of arene to form a nucleophilic carbon atom which can further interact with the weak CO₂ electrophile. The role of the Lewis acid is to activate the CO₂ molecule before the arene C-H bond carboxylation [8]. However, both these strategies usually provide rather low yields of the target products due to the low electrophilicity of CO₂ and side reactions caused by excessive reactivity of the mediators [7, 8]. Therefore, the development of alternative catalytic procedures avoiding the usage of strong base or acid is highly desired but also represents one of the great challenges for this reaction.

Recently, Kanan et al. reported that alkali carbonates (K₂CO₃ and Cs₂CO₃) finely dispersed over TiO₂ support could promote the two-step cycle of benzene esterification with CO₂ and CH₃OH to produce methyl benzoate with both high yield (80%) and high selectivity (100%) in the absence of stoichiometric additives [9]. It is important to note that bare TiO₂ can also promote the first step of benzene C-H bond carboxylation, however, the catalyst became deactivated after just one catalyst recycling. In contrast, no carboxylation products were observed when K₂CO₃ or Cs₂CO₃ powders as the only component was used. Thus, it was hypothesized that dispersing alkali carbonate over TiO₂ would engender catalytic carboxylation activity towards hydrocarbon substrates because of the disruption of the bulk alkali carbonate structure. However, the mechanistic aspects of this system, such as the nature of the active site and the exact role of the different catalyst components, remained moot. Especially for the initial C-H bond carboxylation with CO₂ many possible mechanisms have been proposed [8]. This inspired us to carry out a comprehensive mechanistic study of benzene carboxylation with CO₂ and subsequent methylation by CH₃OH over the K₂CO₃/TiO₂ catalyst by periodic density functional theory calculations. Our main objective was

to identify the role and function of each catalyst component and to propose the origin of the deactivation of bare TiO_2 catalyst.

3.2 Computational details

In this work, all calculations were performed using the Vienna Ab Initio Simulation Package (VASP) 5.3.5 [10, 11]. DFT calculations were carried out using PBE functional based on the generalized gradient approximation (GGA) [12]. Grimme's DFT-D3 method with Becke-Jonson damping was used to account for the dispersion interactions [13]. The DFT+U method was applied to the 3d orbitals of Ti to correct the on-site Coulomb interactions. The U value used in this work is 4.2 eV [14]. The energy cutoff and convergence criteria used in this study were 400 eV, 10^{-5} eV, and 0.05 eV/Å for the electronic and ionic loops, respectively. Transition states were determined by the nudged-elastic band method with the improved tangent estimate (CI-NEB) and subsequent frequency analysis. The model of $\text{K}_2\text{CO}_3/\text{TiO}_2$ catalyst was built following the experimental evidence of the very fine dispersion of K_2CO_3 on the surface of TiO_2 [9]. Figure 3.1 shows the catalyst model featuring the K_2CO_3 species deposited on the defective anatase TiO_2 (101) surface. We hypothesized that the interface of coordination-unsaturated surface Ti site (Ti^{3+}) together with the adjacent K_2CO_3 cluster form the reactive ensemble because neither the bulk crystalline K_2CO_3 nor the pristine TiO_2 surface are active [9, 15].

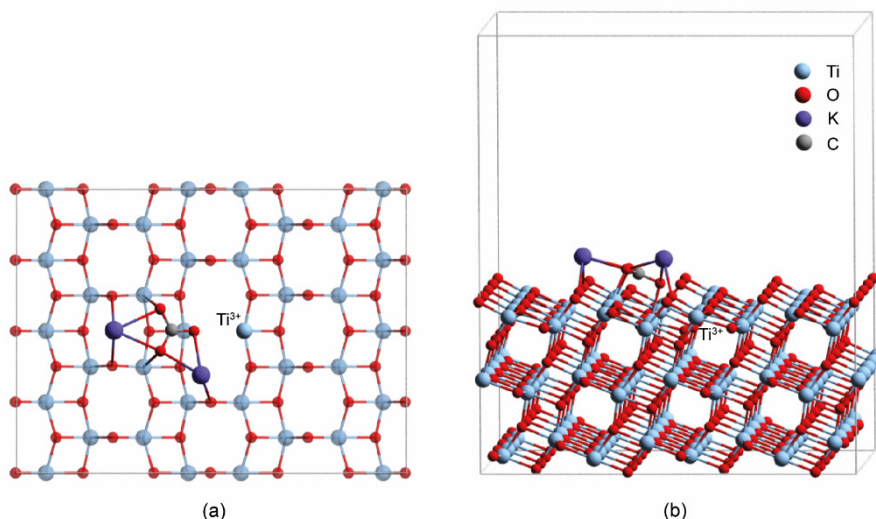


Figure 3.1 Optimized structure of K_2CO_3 supported on defective anatase TiO_2 (101) surface ($\text{K}_2\text{CO}_3/\text{TiO}_2$). (a) and (b) are top view and side view, respectively

3.3 Results

3.3.1 Benzene activation and deprotonation

The experimental study hypothesized that the benzene carboxylation mechanism could proceed via benzene deprotonation followed by rapid reaction with CO_2 to produce a surface-bound carbonate [1]. K_2CO_3 should then be responsible for the deprotonation reaction, as observed in other hydrocarbon carboxylation reactions promoted by homogeneous catalysts [2, 3]. An alternative mechanism involves a direct C-H bond carboxylation via electrophilic attack by pre-activated CO_2 , which has also been considered in a number of earlier studies as a viable reaction path [4, 5]. Herein, both reaction pathways were considered by DFT calculations and the respectively computed energetics are shown in Figure 3.2. We found that the deprotonation of C_6H_6 (Figure 3.2a) is an endothermic reaction with a rather higher activation barrier ($\Delta E_{\text{rxn}} = 1.07$ eV, $E_a = 1.41$ eV). The alternative reaction starts with a much more favourable addition of an activated CO_2^* to C_6H_6 ($\Delta E_{\text{rxn}} = 0.46$ eV, $E_a = 0.72$ eV) followed by an exothermic C-H bond dissociation (Figure 3.2b) ($\Delta E_{\text{rxn}} = -1.37$ eV, $E_a = 1.19$ eV). A similar trend is also observed in the case of bare defective TiO_2 (Figure 3.2c and Figure 3.2d). These results indicate that the C_6H_6 deprotonation that Kanan et al.[9] proposed as an initial reaction step for the benzene carboxylation is both thermodynamically and kinetically less favourable than the direct carboxylation route facilitated by $\text{K}_2\text{CO}_3/\text{TiO}_2$, which is in line with the substantial carboxylation activity of the carbonate-free TiO_2 catalyst.

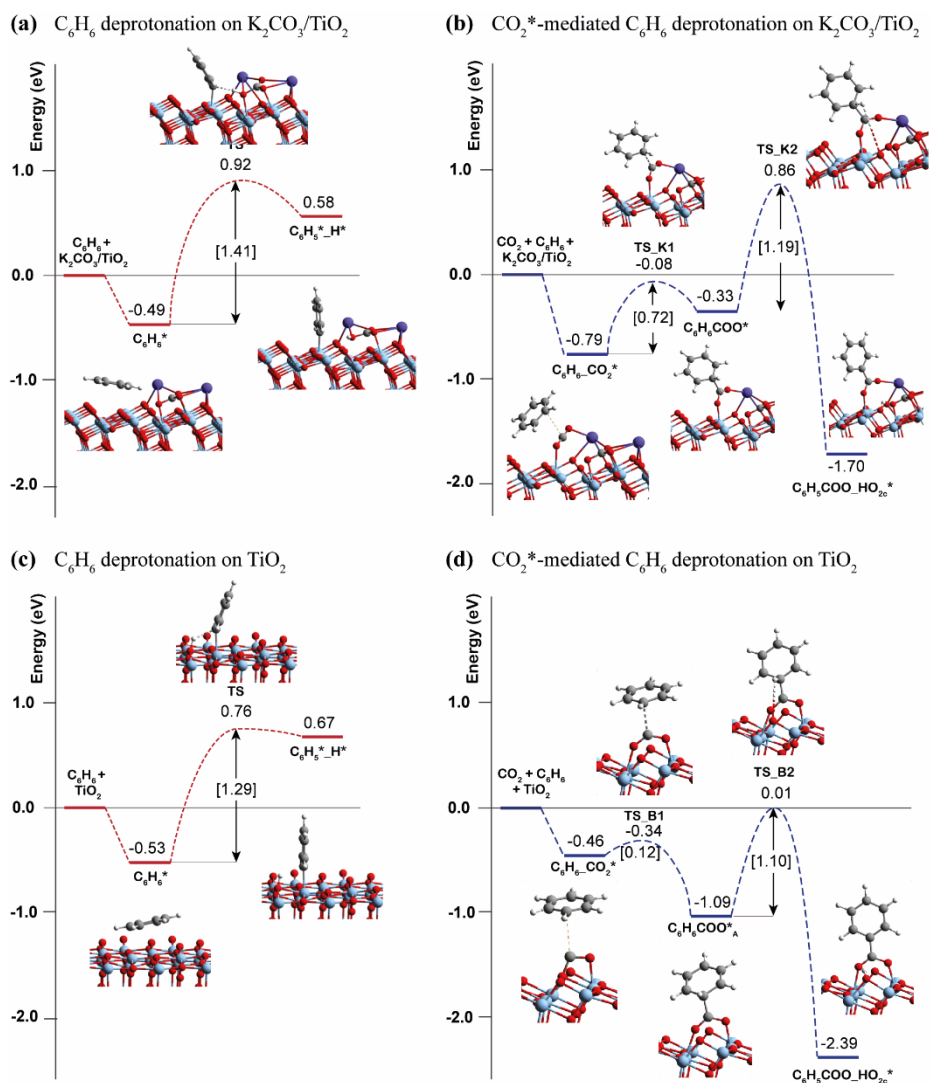
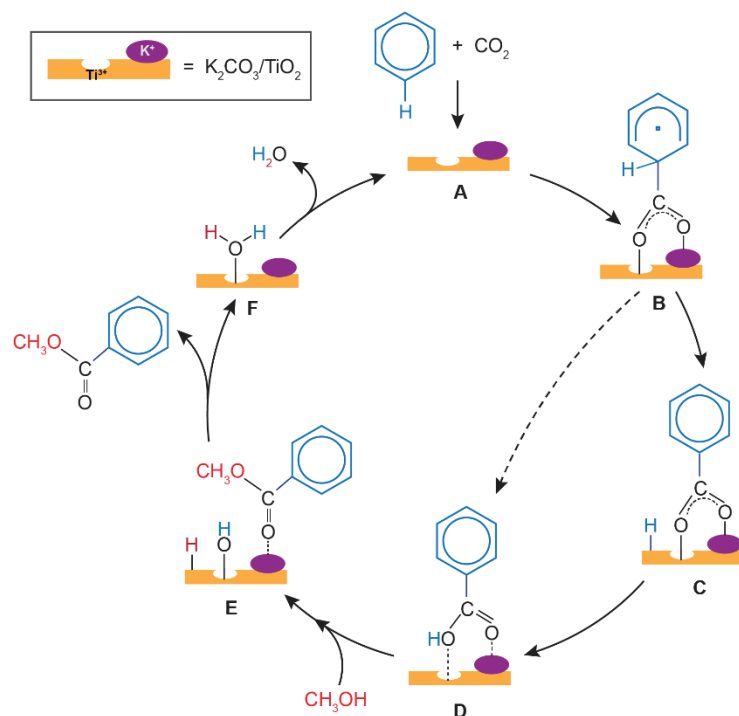


Figure 3.2 The comparison of computed reaction energy diagrams for C_6H_6 deprotonation and CO_2^* -mediated C_6H_6 deprotonation on $\text{K}_2\text{CO}_3/\text{TiO}_2$ and bare defective TiO_2 . **(a)** C_6H_6 deprotonation on $\text{K}_2\text{CO}_3/\text{TiO}_2$. **(b)** CO_2^* -mediated C_6H_6 deprotonation on $\text{K}_2\text{CO}_3/\text{TiO}_2$. **(c)** C_6H_6 deprotonation on bare defective TiO_2 . **(d)** CO_2^* -mediated C_6H_6 deprotonation on bare defective TiO_2 .



Scheme 3.1 Proposed mechanism of benzene esterification with CO_2 and CH_3OH on $\text{K}_2\text{CO}_3/\text{TiO}_2$ catalyst. The $\text{A} + \text{CO}_2 + \text{C}_6\text{H}_6 \rightarrow \text{D}$ conversion involves the carboxylation of benzene with CO_2 via the one-step direct (dashed) or stepwise indirect (solid path) mechanisms to yield the adsorbed benzoic acid. The latter is methylated with CH_3OH ($\text{D} + \text{CH}_3\text{OH} \rightarrow \text{F} + \text{C}_6\text{H}_5\text{COOCH}_3$) to yield methyl benzoate product and the adsorbed water. Subsequent desorption of H_2O by-product ($\text{F} \rightarrow \text{A} + \text{H}_2\text{O}$) regenerates the catalytic surface ensemble.

3.3.2 Esterification of benzene with CO_2 and CH_3OH on $\text{K}_2\text{CO}_3/\text{TiO}_2$

Scheme 3.1 presents a proposed reaction mechanism for the esterification of benzene with CO_2 and CH_3OH by the $\text{K}_2\text{CO}_3/\text{TiO}_2$ catalyst. The computed reaction energy profile is shown in Figure 3.3. The previous section showed that the C-H carboxylation of benzene with activated CO_2 is preferred over the alternative mechanism initiated by the C_6H_6 deprotonation. Thus, we proposed that the reaction starts with the adsorption of CO_2 through bidentate coordination with the interface Ti^{3+} and K^+ sites. It should be noted that the presence of K_2CO_3 prevents a bidentate adsorption mode of CO_2 with two Ti^{3+} surface atoms, which occur on the bare defective TiO_2 surface. In the next step, the C-C bond formation between the co-adsorbed benzene and CO_2^* generates the $\text{C}_6\text{H}_6\text{COO}^*$ intermediate ($\text{C}_6\text{H}_6\text{CO}_2^*$

→ C₆H₆COO*). This step is endothermic with $\Delta E_{\text{rxn}} = 0.46$ eV and proceeds with activation energy (Ea) of 0.72 eV.

Next, the C-H bond of the activated C₆H₆ fragment is cleaved to form benzoic acid (C₆H₅COOH*) or benzoate (C₆H₅COO*) surface intermediate. The former is formed via a direct intramolecular H-transfer from the C₆H₆ moiety of C₆H₆COO* to terminal O of the carboxylate moiety. The computed activation barrier for this step is 1.31 eV. An alternative path involves a two-step surface-assisted H*-transfer, upon which the C₆H₆COO* intermediate is first deprotonated by the vicinal basic surface O sites (Ea = 1.19 eV) followed by the C₆H₅COO* and H* recombination (Ea = 1.19 eV). The highest activation energy of the indirect route is only ca. 0.10 eV lower than that of the direct pathway, indicating that both reaction routes can contribute to the catalytic reaction. The hydrogen transfer from the C₆H₆COO* to form C₆H₅COO* is predicted to be more difficult than the initial coupling of CO₂ and benzene, which is consistent with the experimentally observed kinetic isotopic effect results [9]. The electronic analysis further indicated that effective charge transfer between intermediates and the defective catalyst surface facilitates the C-C coupling and deprotonation reaction processes (Figure 3.4-3.5). The desorption of benzoic acid to regenerate the catalytic interface is endothermic by 0.95 eV.

The closure of the catalytic cycle can be facilitated in the presence of methanol, which reacts with the surface benzoate intermediate (CH₃OH_C₆H₅COOH*) to produce methyl benzoate product (C₆H₅COOCH₃*_HO*_H*). During the methylation process, a CH₃OH molecule is added to the system and co-adsorbed at the neighboring surface oxygen atom of benzoic acid. Then, the methyl benzoate is generated by the formation of the C-O bond between CH₃OH and benzoic acid. The simultaneous deprotonation of CH₃OH* and cleavage of the C-OH bond of C₆H₅COOH* result in the generation of two hydroxyl groups on the surface. This concerted step is slightly exothermic and proceeds with an activation energy of 0.73 eV. In the next step, the methyl benzoate product is desorbed from the surface with ΔE of 0.30 eV. The last step is the recombination of surface OH groups to form H₂O and regenerate the catalytic interface sites (HO*_H*_O₂ → H₂O*). This dehydration step is barrierless but proceeds with a barrier of 0.93 eV associated with the surface migration of H*. Overall, the hydrogen transfer step following the C-C bond formation in the carboxylation process is the most difficult step along the reaction path, with an activation barrier of 1.31 eV.

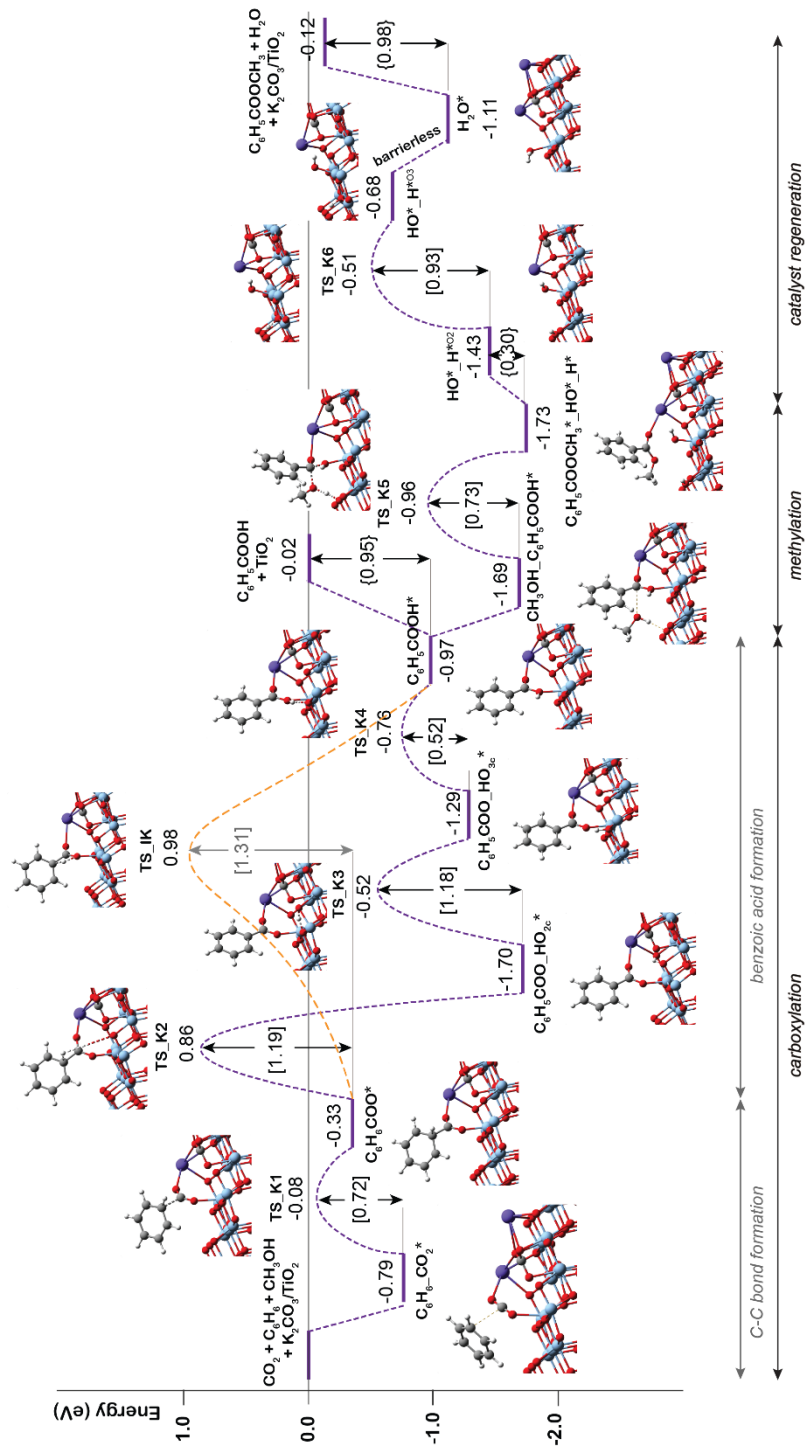


Figure 3.3 DFT-computed reaction energy diagram for the benzene esterification with CO_2 and CH_3OH on $\text{K}_2\text{CO}_3/\text{TiO}_2$.

Electronic structure analysis of $C_6H_6COO^*$: For the 1st step, which represents carboxylation of benzene with CO_2 forming benzoic acid, the $C_6H_6COO^*$ is proposed as the first intermediate. The formation of the meta-stable $C_6H_6COO^*$ species on the surface of the catalyst is facilitated by the interaction of the CO_2 moiety with the Ti^{3+} and K^+ species (with two Ti^{3+} in the case of bare TiO_2). As shown in Figure 3.4, the reaction is formally a nucleophilic aromatic substitution reaction, which is facilitated by the increased nucleophilicity of CO_2 adsorbed to the defect Ti^{3+} sites. This mechanistic proposal is supported by the anionic nature of the $C_6H_6COO^*$ intermediate on K_2CO_3/TiO_2 and bare TiO_2 catalysts as follows from the charge density difference plots.

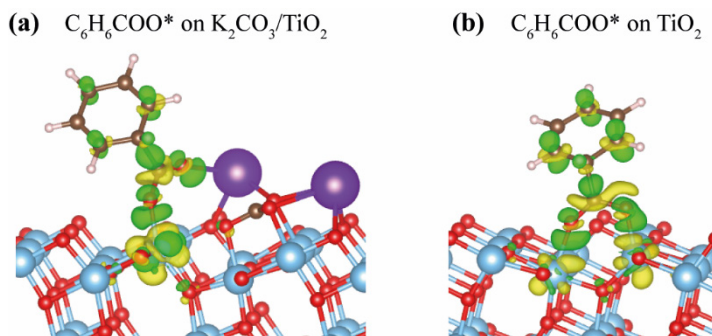


Figure 3.4 Charge density difference plots of $C_6H_6COO^*$ adsorbed on (a) K_2CO_3/TiO_2 and (b) bare defective TiO_2 . The green and yellow regions represent enriched and depleted electron density, respectively. The isosurface values are 0.005 e/Bohr³.

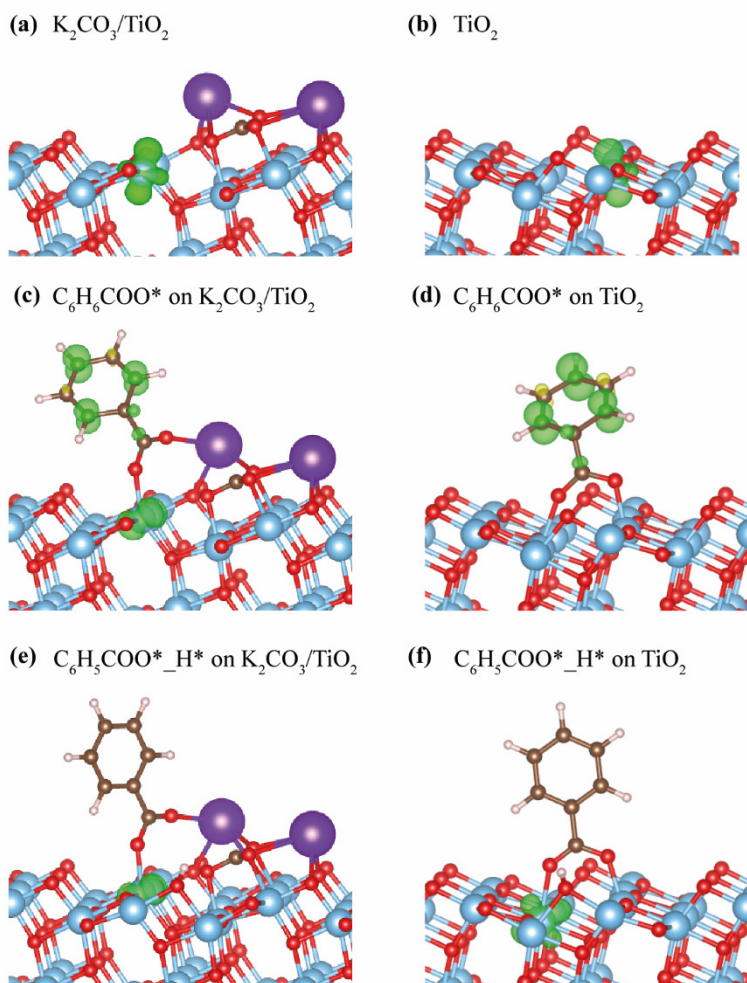


Figure 3.5 The spin density difference of (a) $\text{K}_2\text{CO}_3/\text{TiO}_2$, (b) defective TiO_2 , (c) $\text{C}_6\text{H}_6\text{COO}^*$ on $\text{K}_2\text{CO}_3/\text{TiO}_2$, (d) $\text{C}_6\text{H}_6\text{COO}^*$ on TiO_2 , (e) $\text{C}_6\text{H}_5\text{COO}^*$ on $\text{K}_2\text{CO}_3/\text{TiO}_2$, and (f) $\text{C}_6\text{H}_5\text{COO}^*$ on TiO_2 . Isosurface values are 0.01 e/Bohr^3 .

Figure 3.5 illustrates the spin density difference that occurred during the C-H carboxylation of benzene with CO_2 . Figure 3.5a-b show that the unpaired electron is localized on Ti^{3+} site for both bare TiO_2 and $\text{K}_2\text{CO}_3/\text{TiO}_2$ catalysts. When $\text{C}_6\text{H}_6\text{COO}^*$ intermediate was formed (Figure 3.5c-d), redistribution of the unpaired electrons on the benzene ring indicated the formation of a sigma complex. In the next step, Hydride transfer from the benzene ring to the surface, forming $\text{C}_6\text{H}_5\text{COO}^*$ intermediates leading to spin density relocated to the surface (Figure 3.5e-f).

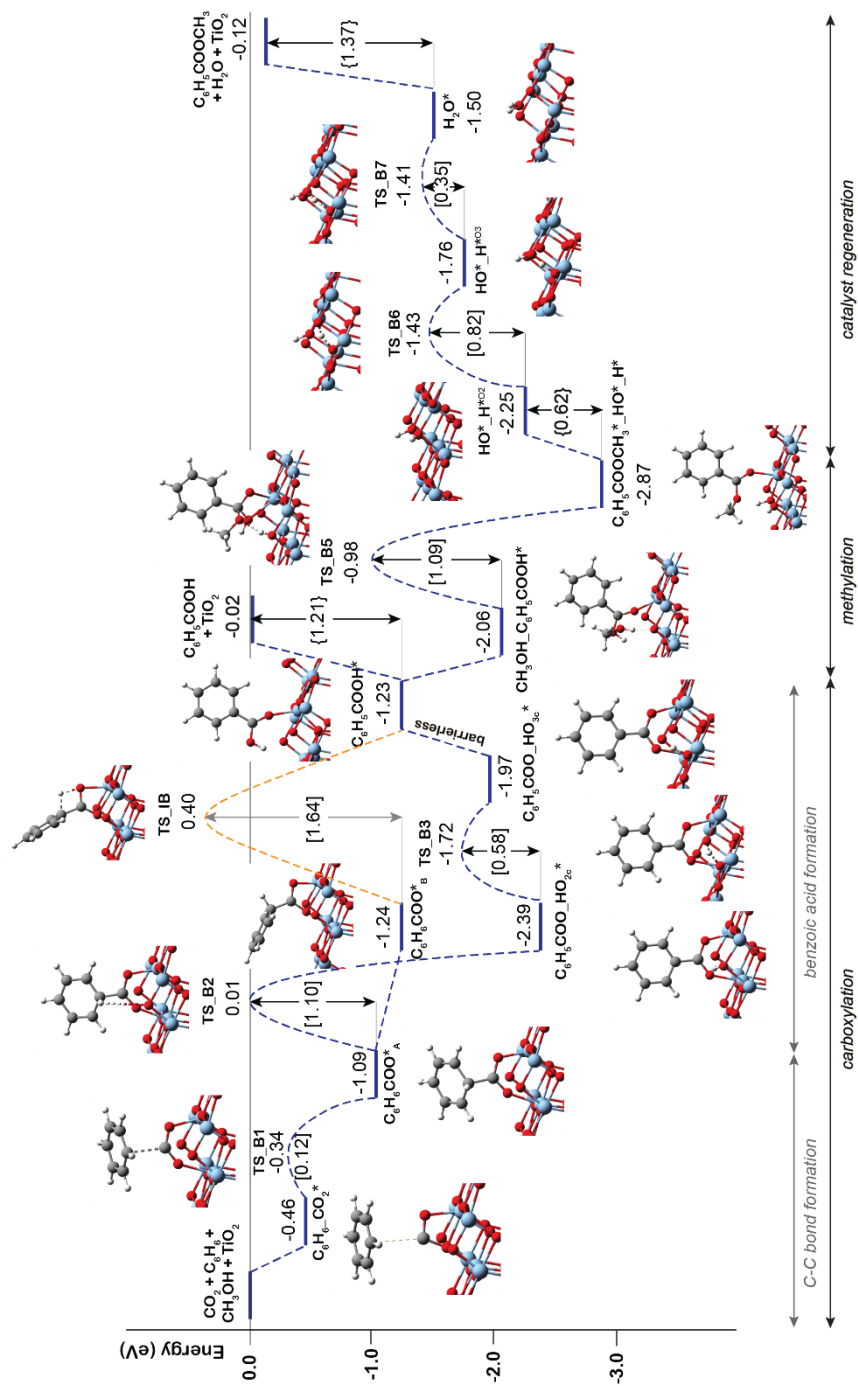


Figure 3.6 DFT-computed reaction energy diagram for the benzene esterification with CO_2 and CH_3OH on bare defective TiO_2 .

3.3.3 Esterification of benzene with CO₂ and CH₃OH on bare TiO₂

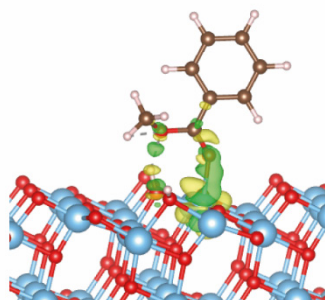
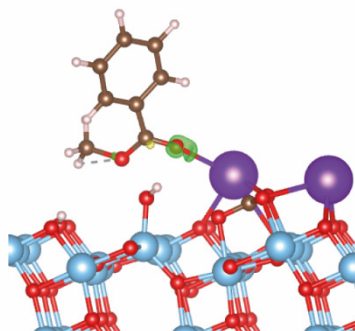
Previous experimental studies [9] showed that the carbonate-free defective TiO₂ can also promote benzene carboxylation, but it loses the activity already after the first reaction cycle. We therefore hypothesized that the reaction intermediates or the reaction products (e.g. methyl benzoate or water) might block the active site of the bare TiO₂ catalyst, while the presence of K₂CO₃ species protects catalyst from such poisoning. To check this hypothesis, the DFT analysis was extended to the mechanism of benzene carboxylation followed by methylation on the bare and defective anatase TiO₂ (101) surface. Figure 3.6 presents the respective DFT-computed reaction energy diagram. In this case, the C-C bond formation between CO₂ and benzene is thermodynamically and kinetically more favorable than on the interface site ($\Delta E_{\text{rxn}} = -0.63$ eV, $E_a = 0.12$ eV). However, the subsequent H* transfer to directly form adsorbed benzoic acid is, in this case, 0.3 eV higher than over the K₂CO₃/TiO₂. A much more favorable reaction is the benzoate formation via the hydroxylation of the TiO₂ surface. This step has a barrier of 1.1 eV and stabilizes the system by ΔE_{rxn} of -1.3 eV. Almost identical energetics was observed for the K₂CO₃/TiO₂ catalyst. For the subsequent concerted benzoic acid methylation reaction, the activation energy over defective TiO₂ is 0.36 eV higher than that of K₂CO₃/TiO₂ catalyst reaction ($E_a(\text{TS_B5}) = 1.09$ eV vs $E_a(\text{TS_K5}) = 0.73$ eV).

The comparison of the reaction profiles in Figures 3.3 and 3.6 reveals that the activation energies of all elementary steps (except the initial CO₂ coupling with benzene) over the defective TiO₂ surface and K₂CO₃-promoted TiO₂ are quite close and comparable suggesting that indeed both catalysts can enable the esterification reaction of benzene with CO₂ and CH₃OH to form methyl benzoate. However, we find that most of the reaction intermediates on the defective TiO₂ surface are significantly more stable than those on K₂CO₃/TiO₂. The energies of all reaction intermediates on the defective TiO₂ surface are in the range of 0.00 to -3.00 eV, while those on K₂CO₃/TiO₂ catalyst fall in the range of +1.00 to -2.00 eV relative to the reactant state. The stronger binding interaction on the bare TiO₂ surface impedes the desorption of the products and regeneration of the active site for the next catalytic cycle. Specifically, the desorption energies of methyl benzoate and H₂O on the defective TiO₂ surface are 0.39 and 0.32 eV higher than that on K₂CO₃/TiO₂, respectively ($E_{\text{des}}(\text{C}_6\text{H}_5\text{COOCH}_3)$: 1.37 eV vs 0.98 eV; $E_{\text{des}}(\text{H}_2\text{O})$: 0.62 eV vs 0.30 eV).

Electronic structure analysis of $C_6H_5COOCH_3^*$ and H_2O^* : The electron density difference plots for $C_6H_5COOCH_3$ and H_2O adsorption on K_2CO_3/TiO_2 and defective TiO_2 are shown in Figure 3.7. Upon adsorption, it can be seen that electron transfer takes place between the adsorption sites (Ti^{3+} and K^+) and the oxygen atoms of the adsorbates ($C_6H_5COOCH_3$ and H_2O). For the adsorption of $C_6H_5COOCH_3$, it is obvious that the electron transfer between $C_6H_5COOCH_3$ and TiO_2 is much more significant than that between $C_6H_5COOCH_3$ and K_2CO_3/TiO_2 , accounting for the stronger interaction and higher desorption barrier. For the adsorption of H_2O on defective TiO_2 , the accumulation of electrons is observed at both Ti^{3+} - O_{H_2O} bonds. In the case of H_2O adsorbed on K_2CO_3/TiO_2 , the accumulation of electrons on the surface is only observed at Ti^{3+} site, while that on K^+ is negligible. These results indicate the stronger interaction of $C_6H_5COOCH_3$ and H_2O on the defective TiO_2 , which is in agreement with the calculated desorption energy.

(a) $C_6H_5COOCH_3^*$ on K_2CO_3/TiO_2

(b) $C_6H_5COOCH_3^*$ on TiO_2



(c) H_2O^* on K_2CO_3/TiO_2

(d) H_2O^* on TiO_2

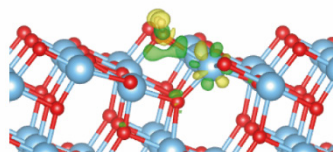
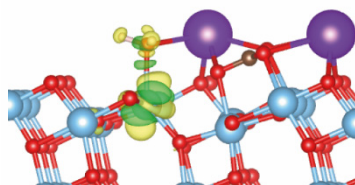


Figure 3.7 Charge density difference of (a) $C_6H_5COOCH_3$ adsorption on K_2CO_3/TiO_2 , (b) $C_6H_5COOCH_3$ adsorption on defective TiO_2 , (c) H_2O adsorption on K_2CO_3/TiO_2 , and (d) H_2O^* adsorption on defective TiO_2 . Green region indicates electron accumulation whereas yellow region indicates electron depletion. Iso-surface values are 0.005 e/Bohr³.

3.4 Conclusion

In this work, we conclude that both bare TiO_2 with oxygen vacancy and $\text{K}_2\text{CO}_3/\text{TiO}_2$ catalysts are able to activate CO_2 and benzene to form benzoate products. However, the excessive reactivity of the surface sites in the former results in surface poisoning by the reaction products/by-products. The presence of potassium carbonate species partially deactivates the reactive sites on the titanium surface to facilitate the product desorption and the regeneration of the catalytic interface sites. Although the K_2CO_3 species cannot act as an active site alone for this reaction, it steers the local structures of the transition states and reaction intermediates, and thus facilitates the products desorption and catalyst regeneration. These insights shed light on the role of multicomponent reaction environments on the catalytic surface for efficient CO_2 valorization. They can form a base for further development of efficient and stable catalysts for the direct carboxylation with CO_2 of other more challenging hydrocarbon substrates such as ethane, methane, and ethylene.

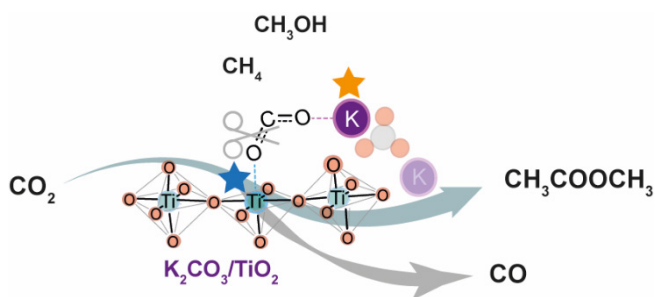
References

1. Burkart, M.D., N. Hazari, C.L. Tway, and E.L. Zeitler, *Opportunities and Challenges for Catalysis in Carbon Dioxide Utilization*. *ACS Catal.*, 2019. **9**(9): p. 7937-7956.
2. Kamkeng, A.D.N., M. Wang, J. Hu, W. Du, and F. Qian, *Transformation technologies for CO_2 utilisation: Current status, challenges and future prospects*. *J. Chem. Eng.*, 2021. **409**: p. 128138.
3. Hepburn, C., E. Adlen, J. Beddington, E.A. Carter, S. Fuss, N. Mac Dowell, J.C. Minx, P. Smith, and C.K. Williams, *The technological and economic prospects for CO_2 utilization and removal*. *Nature*, 2019. **575**(7781): p. 87-97.
4. Olah, G.A., B. Török, J.P. Joschek, I. Bucsí, P.M. Esteves, G. Rasul, and G.K. Surya Prakash, *Efficient Chemoselective Carboxylation of Aromatics to Arylcarboxylic Acids with a Superelectrophilically Activated Carbon Dioxide- $\text{Al}_2\text{Cl}_6/\text{Al}$ System*. *J. Am. Chem. Soc.*, 2002. **124**(38): p. 11379-11391.
5. Lindsey, A.S. and H. Jeskey, *The Kolbe-Schmitt Reaction*. *Chem. Rev.*, 1957. **57**(4): p. 583-620.
6. Luo, J., S. Preciado, P. Xie, and I. Larrosa, *Carboxylation of Phenols with CO_2 at Atmospheric Pressure*. *Eur. J. Chem.*, 2016. **22**(20): p. 6798-6802.
7. Nemoto, K., H. Yoshida, N. Egusa, N. Morohashi, and T. Hattori, *Direct Carboxylation of Arenes and Halobenzenes with CO_2 by the Combined Use of AlBr_3 and R_3SiCl* . *J. Org. Chem.*, 2010. **75**(22): p. 7855-7862.

8. Luo, J. and I. Larrosa, *C-H Carboxylation of Aromatic Compounds through CO₂ Fixation*. *ChemSusChem*, 2017. **10**(17): p. 3317-3332.
9. Xiao, D.J., E.D. Chant, A.D. Frankhouser, Y. Chen, A. Yau, N.M. Washton, and M.W. Kanan, *A closed cycle for esterifying aromatic hydrocarbons with CO₂ and alcohol*. *Nat. Chem.*, 2019. **11**(10): p. 940-947.
10. Kresse, G. and J. Furthmüller, *Efficiency of ab-initio total energy calculations for metals and semiconductors using a plane-wave basis set*. *Comput. Mater. Sci.*, 1996. **6**(1): p. 15-50.
11. Kresse, G. and J. Furthmüller, *Efficient iterative schemes for ab initio total-energy calculations using a plane-wave basis set*. *Phys. Rev. B*, 1996. **54**(16): p. 11169-11186.
12. Perdew, J.P., K. Burke, and M. Ernzerhof, *Generalized Gradient Approximation Made Simple*. *Phys. Rev. Lett.*, 1996. **77**(18): p. 3865-3868.
13. Grimme, S., S. Ehrlich, and L. Goerigk, *Effect of the damping function in dispersion corrected density functional theory*. *J. Comput. Chem.*, 2011. **32**(7): p. 1456-1465.
14. Song, W., S. Ma, L. Wang, J. Liu, and Z. Zhao, *Theoretical Explanation of the Photogenerated Carrier Separation at the Surface Junction*. *ChemCatChem*, 2017. **9**(23): p. 4340-4344.
15. Sorescu, D.C., W.A. Al-Saidi, and K.D. Jordan, *CO₂ adsorption on TiO₂(101) anatase: A dispersion-corrected density functional theory study*. *J. Chem. Phys.*, 2011. **135**(12): p. 124701.

4

CH₄ esterification with CO₂ and CH₃OH on K₂CO₃/TiO₂

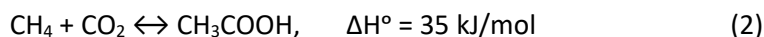
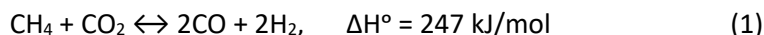


The catalytic activity of K₂CO₃/TiO₂ for the two-step cycle of CH₄ esterification with CO₂ and CH₃OH was investigated computationally and compared with the reaction of C₆H₆. Even though the theory predicts that the K₂CO₃/TiO₂ can catalyze the carboxylation of CH₄ with CO₂ and the subsequent methylation by CH₃OH, the reaction is not selective. The formation of side product (CO) competes with the CH₄ carboxylation, while it is not the case for the carboxylation of C₆H₆.

4.1 Introduction

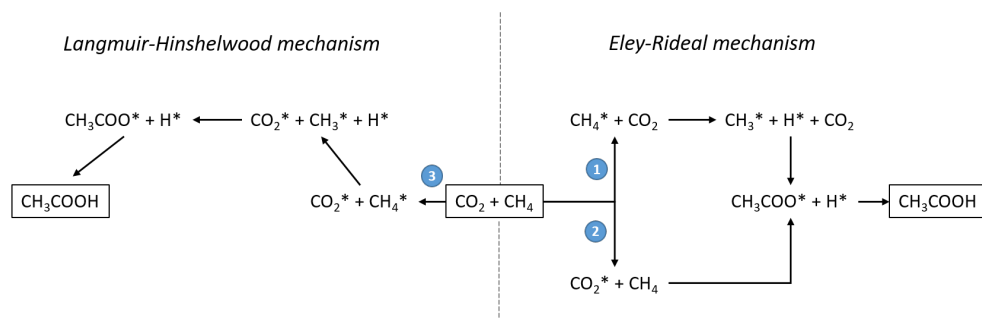
CO₂ and CH₄ are the primary greenhouse gases that cause the global warming crisis. The development of an effective approach for converting these greenhouse gases into fuels and chemicals is of great importance to environmental sustainability as well as economic benefits. However, using CO₂ and CH₄ as co-feedstocks is still challenging because of their high stability. To date, most studies have focused on the dry reforming of CH₄ with CO₂ to produce syngas (CO and H₂), followed by either CH₃OH synthesis or Fischer-Tropsch processes [1]. Nevertheless, the high energy demand and the deactivation of catalysts are the drawbacks of producing syngas.

Besides the syngas synthesis, the production of CH₃COOH by the direct C-C coupling of CH₄ and CO₂ has gained attention due to the 100% atomic efficiency and relatively mild conditions [2]. The CH₃COOH is an important industrial feedstock to produce value-added chemicals such as vinyl acetate, cellulose acetate, and acetic anhydride [3, 4]. Another advantage of CH₃COOH production over traditional dry reforming is that it requires much lower enthalpy of the formation (ΔH°), as shown in equations (1) and (2) [5, 6]. However, the high stability of the substrate molecules in this process remains a challenge.



So far, many catalysts have been developed to promote the activation of the challenging CH₄ and CO₂ substrates for the direct CH₃COOH synthesis. The promising catalyst should be able to activate CH₄ and CO₂ simultaneously as well as stabilize the CH₃* species to prevent coke formation from the dehydrogenation process [6]. Thus, using multifunctional heterogeneous catalysts can achieve efficient production of CH₃COOH. Pd/SiO₂ [7], Rh/SiO₂ [7], Fe/ZnO [8], Zn/CeO₂ [1], and Co/Pd-based TiO₂ [9] are the metal oxide catalysts that have been used for the direct conversion of CO₂ and CH₄ to CH₃COOH. The overall conversion process contains four elementary reaction steps: (1) the dissociation of CH₄, (2) the activation of CO₂, (3) the C-C bond coupling, and (4) the protonation of acetate forming acetic acid [1, 8, 10, 11]. The mechanistic studies by experiments and DFT calculations reveal that this reaction can occur via either the Langmuir-Hinshelwood (LH) or Eley-Rideal (ER) mechanism depending on the types and nature of active sites [2]. The LH mechanism is defined as the reaction of two surface species (CO₂* and CH₃*) forming acetate intermediate, while the ER

mechanism represents the reaction between adsorbed species and gas-phase molecules. In most cases, the insertion of gas-phase CO_2 into CH_3^* is proposed [1, 10, 11], while the direct interaction between adsorbed CO_2^* and gas-phase CH_4 is rarely reported. Three possible reaction pathways for the conversion of CO_2 and CH_4 to CH_3COOH are summarized in Scheme 4.1.



Scheme 4.1. Three possible pathways for the direct conversion of CH_4 and CO_2 to CH_3COOH .

Considering the active site of catalysts, it was found that the ER mechanism usually occurs on the metal sites, while the LH mechanism dominates on the oxide surfaces. Generally, a Lewis acid-base pair on metal oxide catalysts is responsible for the heterolytic C-H bond dissociation of CH_4 and the activation of CO_2 [2]. In some cases, the oxygen vacancies (O_v) on the surface can serve as an active site for activating CH_4 and CO_2 . For instance, the O_v site of Zn-doped CeO_2 can facilitate CH_4 activation [12]. The O_v of In_2O_3 in $\text{ZnO}/\text{In}_2\text{O}_3$ catalyst was found to be an active site for adsorption and activation of CO_2 [13]. In addition, additives such as alkali or alkali earth metals can influence the reactivity of CO_2 . For example, the addition of alkalis was found to promote the CO_2 methanation activity of Ru/TiO_2 catalyst [14, 15]. The modifications of rutile TiO_2 with MgO , CaO , and BaO were found to promote the activation of CO_2 , forming tridentate carbonate-like species [16]. However, the role of active sites and the mechanisms may change due to the type and nature of catalysts. Therefore, identifying active sites and understanding their role in each elementary reaction step is essential for improving catalytic performance.

Recently, Kanan and co-workers [17] reported the new efficient $\text{K}_2\text{CO}_3/\text{TiO}_2$ catalyst for the two-step cycle of benzene esterification with CO_2 and CH_3OH . The first cycle is the benzene C-H bond carboxylation with CO_2 , while another is the methylation of benzoate with CH_3OH forming methyl ester. Our DFT calculations described in the previous chapter revealed that the K_2CO_3 species could prevent catalyst poisoning, whereas the O_v surface site significantly affects the catalytic

activity. The interfacial atoms at the proximity of O_v , such as $Ti^{3+}-K^+$ and $Ti^{3+}-O^{2-}$, are responsible for binding the reactive intermediate [18]. In this chapter, we applied those finding to explore the catalytic potential of K_2CO_3/TiO_2 for a similar reaction but using CH_4 instead of benzene. We expect that the understanding through this study will be useful in the rational design of oxides-based catalysts for the effective direct conversion of CH_4 and CO_2 to produce C_{2+} chemicals.

4.2 Computational details

All calculations were performed using the Vienna Ab Initio Simulation Package (VASP) 5.3.5 [19, 20]. DFT calculations were carried out using PBE functional based on the generalized gradient approximation (GGA) [21]. Grimme's DFT-D3 method with Becke-Jonson damping was used to account for the dispersion interactions [22]. The DFT+U method was applied to the 3d orbitals of Ti to correct the on-site Coulomb interactions. The U value used in this work is 4.2 eV [23]. The energy cutoff and convergence criteria for the electronic and ionic loops were 400 eV, 10^{-5} eV, and 0.05 eV/Å, respectively. Transition states were determined by the nudged-elastic band method with the improved tangent estimate (CI-NEB) and subsequent frequency analysis. The model of K_2CO_3/TiO_2 catalyst was built as described in our previous work [18] following the experimental evidence of the very fine dispersion of K_2CO_3 on the surface of TiO_2 [17]. The catalyst model featuring the K_2CO_3 species deposited on the defective anatase TiO_2 (101) surface as the same as shown in Chapter 3 (Figure 3.1). We hypothesized that the interface of coordination-unsaturated surface Ti site (Ti^{3+}) together with the 2-coordinated O surface site (O_{2c}), and the adjacent K_2CO_3 cluster form the reactive ensemble because neither the bulk crystalline K_2CO_3 nor the pristine TiO_2 surface are active [17, 24].

4.3 Results and Discussion

4.3.1 The dissociative adsorption of CH_4

Both Eley-Rideal (ER) and Langmuir-Hinshelwood (LH) mechanisms were proposed for the coupling of CH_4 and CO_2 , depending on the types and nature of catalysts (Scheme 4.1) [2]. In the first case, a common mechanistic picture involves the dissociation of CH_4 on the catalyst surface followed by the C-C coupling with a gas-phase CO_2 , as shown in the route ① in Scheme 4.1. When taking place on metal oxides, the oxygen vacancy site can promote the adsorption and activation of CO_2 , facilitating thus the coupling of a gas-phase CH_4 over an activated CO_2 (② in Scheme

4.1). In the case of LH mechanism, the product of CH_3COOH is formed via the C-C coupling of two surface species, CO_2^* and CH_3^* , as shown in route ③ in Scheme 4.1. We, therefore, first considered the dissociative adsorption of CH_4 on the $\text{K}_2\text{CO}_3/\text{TiO}_2$ model surface. The respective computed reaction energy diagrams and optimized structures of the key intermediates and transition states are shown in Figure 4.1. Upon adsorption ($\Delta E_{\text{ads,CH}_4} = -0.22$ eV), CH_4 coordinates weakly to the open Ti^{3+} surface site and forms additional weak $\text{CH}\cdots\text{O}$ interactions ($r = 2.20$ Å) with surface oxygen atoms (Figure 4.2a). Next, the C-H bond, which points to the adjacent O_{2c} site, is dissociated to form CH_3^* on the Ti^{3+} site and leaves its H on the O_{2c} site as a Brønsted acid. The formally heterolytic C-H cleavage of methane is predicted to be a kinetically difficult ($E_a = 1.76$ eV) and thermodynamically unfavorable process ($\Delta E = 0.54$ eV).

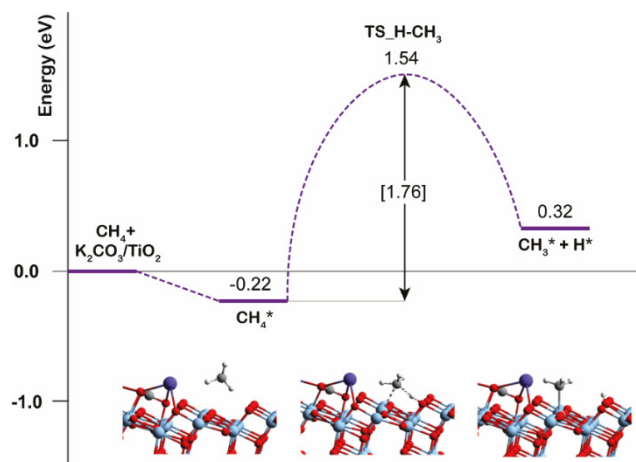


Figure 4.1 Reaction energy diagram for CH_4 dissociation on $\text{K}_2\text{CO}_3/\text{TiO}_2$

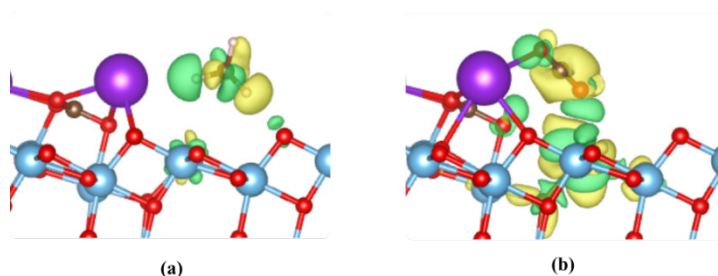


Figure 4.2 Electron density difference plots of (a) CH_4^* , and (b) CO_2^* structures on $\text{K}_2\text{CO}_3/\text{TiO}_2$. The green and yellow regions represent enriched and depleted electron density, respectively (isosurface value = $0.001 \text{ e}/\text{Bohr}^3$).

For the alternative reaction pathway following ER mechanism (② in Scheme 4.1), the CO₂ adsorption is considered as the initial step. The adsorbed CO₂ interacts with Ti³⁺ and K⁺ sites through its O atoms. The O-C-O angle is 177.6° implying CO₂ is activated. The adsorption energy of CO₂ is calculated to be -0.40 eV, which is about two times stronger than that of CH₄. This result is also reflected by a large electron accumulation between O of CO₂ and Ti³⁺ surface site, as shown in Figure 4.2b. The electron density plot also indicates the transfer of electrons from CO₂ to the surface, resulting in the electrophilicity of adsorbed CO₂. Hence, we hypothesize that the carboxylation of CH₄ with CO₂ on the K₂CO₃/TiO₂ starts with the CO₂^{*} rather than the CH₄^{*} due to the strong adsorption energy of CO₂ and the high activation energy of CH₄ dissociation. In addition, the difficulty of CH₄ dissociation implies that the LH mechanism (③ in Scheme 4.1) is not the preferred reaction pathway for the coupling of CO₂ and CH₄ on the K₂CO₃/TiO₂ catalyst.

4.3.2 CH₄ carboxylation with CO₂ to CH₃COOH

As described in the above section, we propose that CH₃COOH can be produced on the K₂CO₃/TiO₂ catalyst by the C-C coupling of activated CO₂ and gas-phase CH₄. The reaction mechanism and energy profiles are shown in Figure 4.3. The reaction starts with the adsorption of CO₂ at the interface Ti³⁺ and K⁺ sites, followed by the physisorption of CH₄ at the nearby O_{2c} site (CH₄_CO^{*}). Then the C-C coupling of CO₂^{*} and CH₄ occurs simultaneously with the breaking of one C-H bond of CH₄, forming the CH₃COO^{*} intermediate and H^{*} on the surface. This reaction is exothermic with an activation barrier of 1.22 eV, which is about 0.50 eV lower than that of the direct C-H bond dissociation of CH₄ on the catalyst. This indicates that CO₂^{*} can facilitate the C-H bond activation of CH₄, which is similar to the C-H carboxylation of C₆H₆ with CO₂ discussed in Chapter 3.

In the next step, the proton migration might occur before the protonation of CH₃COO^{*} due to a long distance between CH₃COO^{*} and H^{*}_O_{2c} (3.40 Å). The activation energy of the proton migration from the O_{2c} to the O_{3c} site is about 1.00 eV. After that, the CH₃COO^{*} is protonated by the H^{*}_O_{3c} forming CH₃COOH^{*} with an activation barrier of 0.32 eV. The alternative reaction pathway is a direct H-transfer from CH₄ to the terminal O of CO₂^{*} (concerted route). We found that the activation energy of this step is extremely high (E_a = 2.45 eV), indicating this reaction route is not feasible. It should be noted that this result differs from our previous study in that the carboxylation of C₆H₆ with CO₂ on the same catalyst can proceed via both stepwise and concerted manners with a small difference in activation energy (ΔE_a = 0.1 eV).

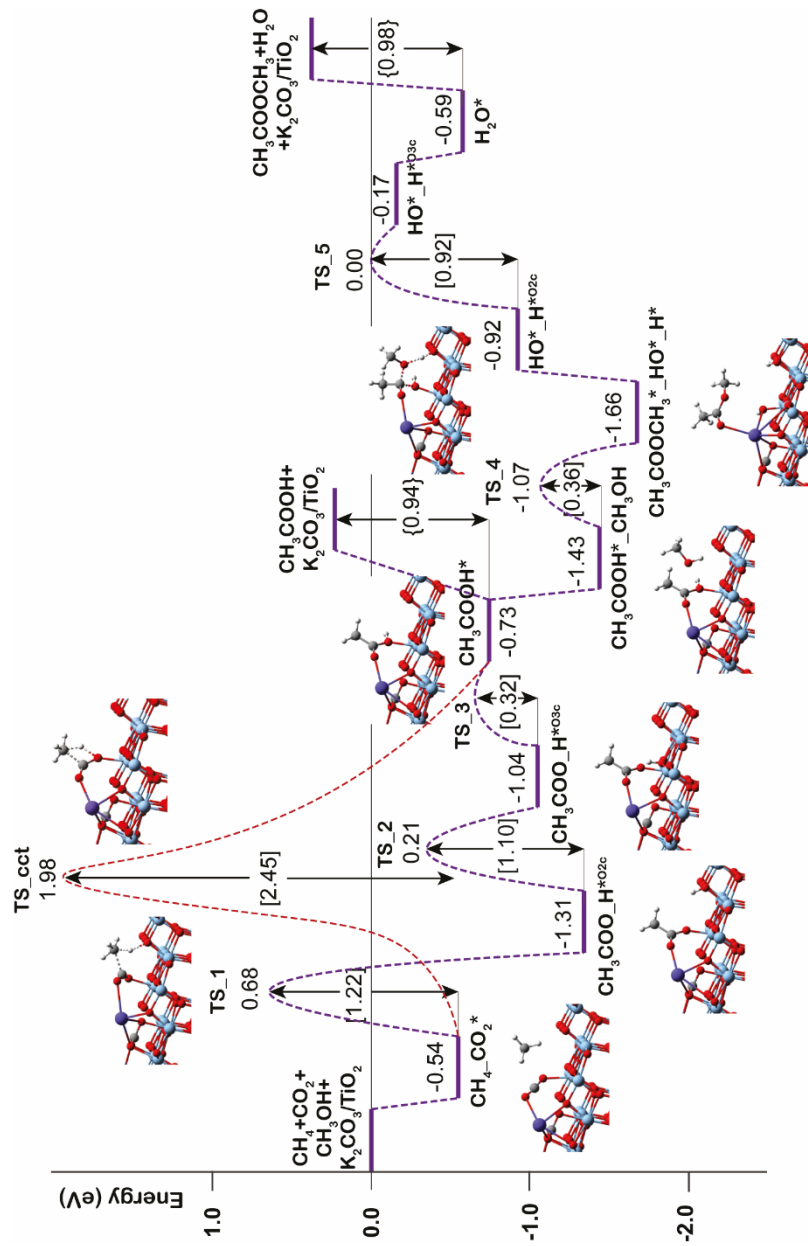


Figure 4.3 Reaction energy profile for the CH_4 carboxylation with CO_2 and subsequent reaction with CH_3OH on $\text{K}_2\text{CO}_3/\text{TiO}_2$

4.3.3 CH₃COOH methylation with CH₃OH to CH₃COOCH₃

In this section, the esterification of CH₃COOH with CH₃OH by K₂CO₃/TiO₂ catalyst is investigated, as shown in Figure 4.3. Similar to the esterification of benzoic acid in Chapter 3, CH₃OH weakly interacts with the O_{2c} surface site and the –OH moiety of acetic acid through its OH group forming CH₃COOH*–CH₃OH complex. Then, the esterification is occurred by forming a C–O bond between the C atom of CH₃COOH* and the O atom of CH₃OH. At the same time, the C–OH bond of CH₃COOH* cleaves accompanied by the deprotonation of CH₃OH producing CH₃COOCH₃* and two hydroxyl groups on the surface (CH₃COOCH₃*–HO*–H*). This process is slightly exothermic and proceeds with a small activation energy ($E_a = 0.36$ eV). Then, CH₃COOCH₃ can desorb from the catalyst with a barrier of 0.74 eV. For the last step, the two hydroxyl groups on the surface can form H₂O and the catalytic active site is regenerated (HO*–H*O_{3c} → H₂O*). This reaction is barrierless, however, H* migration on the surface needs to overcome a barrier of 0.92 eV before H₂O formation. The desorption energy of H₂O is calculated to be 0.98 eV. Overall, the C–C coupling of CO₂ with CH₄ is identified as the most difficult step of the reaction, with the highest activation barrier of 1.22 eV along the reaction coordinate.

4.3.4 Product selectivity and comparison between CH₄ and benzene

We also studied the dissociation of CO₂* to CO* because this reaction might be a competitive pathway to the production of CH₃COOH. As shown in Figure 4.4, the dissociation of CO₂ occurred by the C–O bond cleavage forming CO, while a leaving O atom from CO₂ occupies the unsaturated Ti³⁺ surface site. This process is slightly endothermic, with an activation energy of 1.16 eV. The moderate activation energy indicates that the direct dissociation of CO₂ to CO on K₂CO₃/TiO₂ is possible.

We further compared the coupling of CO₂* and CH₄ (Figure 4.5a) with the direct conversion of CO₂* to CO*. The results show that the activation energy difference between both reactions is very small ($\Delta E_a = 0.06$ eV). Thus, CO might be observed as a side product of the reaction, whereas the oxidation of Ti³⁺ to Ti⁴⁺ during this process could deactivate the catalyst.

In the case of benzene (Figure 4.5b), the activation energy of C–H carboxylation with CO₂ was calculated to be 1.19 eV. This energy is almost identical to the CO formation (1.16 eV) and the C–H carboxylation with CO₂ in CH₄ (1.22 eV). So, it seems that the formation of CO could compete with the production of benzoate. However, the experimental results showed high selectivity to benzoate (88–91%).

We hypothesize that the formation of metastable $\text{C}_6\text{H}_6\text{COO}^*$ is a key to the high selectivity of benzoate. As shown in Figure 4.5, the C-H carboxylation with CO_2 in CH_4 proceeds in one step without forming an intermediate, while benzene occurs in two-step reactions via the $\text{C}_6\text{H}_6\text{COO}^*$. The formation of such metastable intermediate is due to the aromaticity of benzene, as described in Chapter 3. This process requires an activation energy of 0.72 eV, which is significantly lower than the conversion of CO_2 to CO . Thus, this result can explain why the C-H carboxylation of benzene with CO_2 dominates over the decomposition of CO_2 .

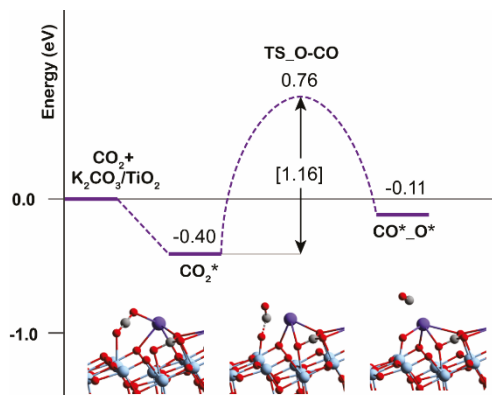


Figure 4.4. Reaction energy diagram for CO_2 dissociation on $\text{K}_2\text{CO}_3/\text{TiO}_2$

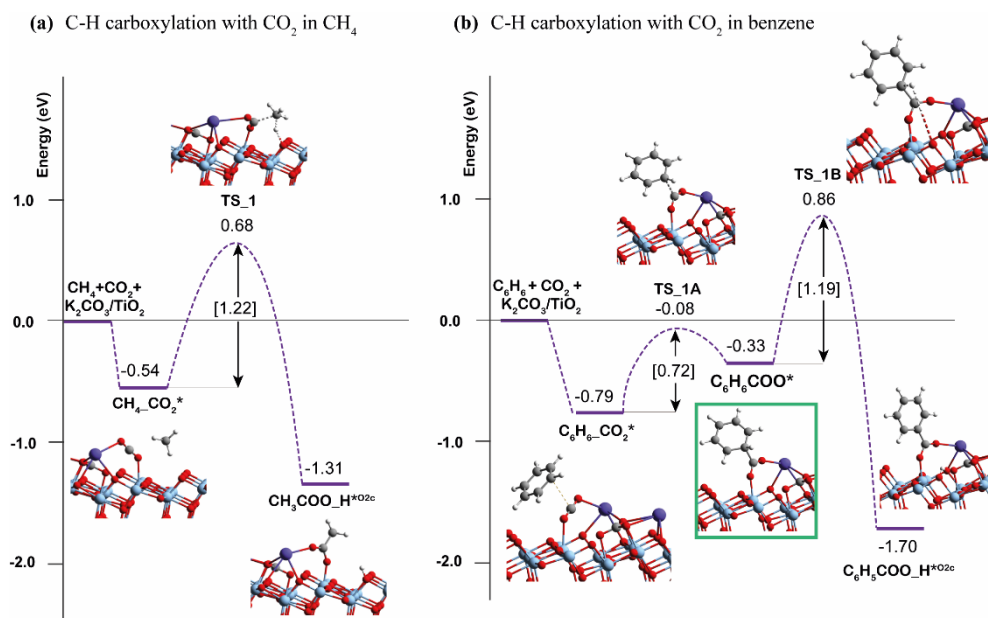


Figure 4.5. Reaction energy diagram for the C-H carboxylation with CO_2 in (a) CH_4 and (b) benzene

4.4 Conclusion

Our previous computational study [18] and experimental study from Kanan et al. [17] showed that the $\text{K}_2\text{CO}_3/\text{TiO}_2$ is an efficient catalyst for benzene esterification with CO_2 and CH_3OH . Hence, we further extend this system to study other hydrocarbon carboxylation and further esterification. In this study, CH_4 is used as a representative of non-aromatic compounds. The results indicate that $\text{K}_2\text{CO}_3/\text{TiO}_2$ is an efficient catalyst for the esterification of both benzoic acid and acetic acid with CH_3OH . For the carboxylation reaction, the $\text{K}_2\text{CO}_3/\text{TiO}_2$ can catalyze both C_6H_6 and CH_4 carboxylation with CO_2 . However, it is interesting to note that the side reaction, which is the formation of CO , could compete with the CH_4 carboxylation, while it is not the case for the C_6H_6 carboxylation reaction. Therefore, we expect the low selectivity of carboxylate when using a non-aromatic compound as a reactant for the carboxylation with CO_2 on $\text{K}_2\text{CO}_3/\text{TiO}_2$ catalyst. To improve product selectivity, enhancing the Lewis basic strength of the O_{2c} site by replacing Ti^{4+} with a lower-valence cation might be one of the strategies to facilitate the C-H bond activation of CH_4 , which is the most difficult step of the reaction.

References

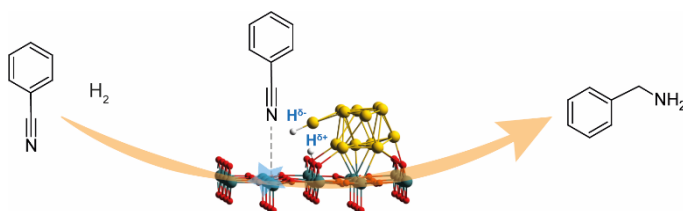
1. Zhao, Y., C. Cui, J. Han, H. Wang, X. Zhu, and Q. Ge, *Direct C–C Coupling of CO_2 and the Methyl Group from CH_4 Activation through Facile Insertion of CO_2 into Zn–CH_3 σ -Bond*. *J. Am. Chem. Soc.*, 2016. **138**(32): p. 10191-10198.
2. Tu, C., X. Nie, and J.G. Chen, *Insight into Acetic Acid Synthesis from the Reaction of CH_4 and CO_2* . *ACS Catal.*, 2021. **11**(6): p. 3384-3401.
3. Martín-Espejo, J.L., J. Gandara-Loe, J.A. Odriozola, T.R. Reina, and L. Pastor-Pérez, *Sustainable routes for acetic acid production: Traditional processes vs a low-carbon, biogas-based strategy*. *Sci. Total Environ.*, 2022. **840**: p. 156663.
4. Merli, G., A. Becci, A. Amato, and F. Beolchini, *Acetic acid bioproduction: The technological innovation change*. *Sci. Total Environ.*, 2021. **798**: p. 149292.
5. Arora, S. and R. Prasad, *An overview on dry reforming of methane: strategies to reduce carbonaceous deactivation of catalysts*. *RSC Adv.*, 2016. **6**(110): p. 108668-108688.
6. Alcantara, M.L., K.A. Pacheco, A.E. Bresciani, and R.M. Brito Alves, *Thermodynamic Analysis of Carbon Dioxide Conversion Reactions. Case Studies: Formic Acid and Acetic Acid Synthesis*. *Ind. Eng. Chem. Res.*, 2021. **60**(25): p. 9246-9258.

7. Ding, Y.-H., W. Huang, and Y.-G. Wang, *Direct synthesis of acetic acid from CH₄ and CO₂ by a step-wise route over Pd/SiO₂ and Rh/SiO₂ catalysts*. *Fuel Process. Technol.*, 2007. **88**(4): p. 319-324.
8. Nie, X., X. Ren, C. Tu, C. Song, X. Guo, and J. G. Chen, *Computational and experimental identification of strong synergy of the Fe/ZnO catalyst in promoting acetic acid synthesis from CH₄ and CO₂*. *Chem. Commun.*, 2020. **56**(28): p. 3983-3986.
9. Huang, W., W.Z. Sun, and F. Li, *Efficient synthesis of ethanol and acetic acid from methane and carbon dioxide with a continuous, stepwise reactor*. *AIChE J.*, 2010. **56**(5): p. 1279-1284.
10. Montejo-Valencia, B.D., Y.J. Pagán-Torres, M.M. Martínez-Iñesta, and M.C. Curet-Arana, *Density Functional Theory (DFT) Study To Unravel the Catalytic Properties of M-Exchanged MFI, (M = Be, Co, Cu, Mg, Mn, Zn) for the Conversion of Methane and Carbon Dioxide to Acetic Acid*. *ACS Catal.*, 2017. **7**(10): p. 6719-6728.
11. Wang, S., S. Guo, Y. Luo, Z. Qin, Y. Chen, M. Dong, J. Li, W. Fan, and J. Wang, *Direct synthesis of acetic acid from carbon dioxide and methane over Cu-modulated BEA, MFI, MOR and TON zeolites: a density functional theory study*. *Catal. Sci. Technol.*, 2019. **9**(23): p. 6613-6626.
12. Zhao, Y., H. Wang, J. Han, X. Zhu, and Q. Ge, *Active Site Ensembles Enabled C–C Coupling of CO₂ and CH₄ for Acetone Production*. *J. Phys. Chem. C*, 2018. **122**(17): p. 9570-9577.
13. Zhao, Y., H. Wang, J. Han, X. Zhu, D. Mei, and Q. Ge, *Simultaneous Activation of CH₄ and CO₂ for Concerted C–C Coupling at Oxide–Oxide Interfaces*. *ACS Catal.*, 2019. **9**(4): p. 3187-3197.
14. Petala, A. and P. Panagiotopoulou, *Methanation of CO₂ over alkali-promoted Ru/TiO₂ catalysts: I. Effect of alkali additives on catalytic activity and selectivity*. *Appl. Catal. B*, 2018. **224**: p. 919-927.
15. Panagiotopoulou, P., *Methanation of CO₂ over alkali-promoted Ru/TiO₂ catalysts: II. Effect of alkali additives on the reaction pathway*. *Appl. Catal. B*, 2018. **236**: p. 162-170.
16. Nolan, M., *Alkaline earth metal oxide nanocluster modification of rutile TiO₂ (110) promotes water activation and CO₂ chemisorption*. *J. Mater. Chem. A*, 2018. **6**(20): p. 9451-9466.
17. Xiao, D.J., E.D. Chant, A.D. Frankhouser, Y. Chen, A. Yau, N.M. Washton, and M.W. Kanan, *A closed cycle for esterifying aromatic hydrocarbons with CO₂ and alcohol*. *Nat. Chem.*, 2019. **11**(10): p. 940-947.
18. Meeprasert, J., G. Li, and E.A. Pidko, *Mechanistic investigation of benzene esterification by K₂CO₃/TiO₂: the catalytic role of the multifunctional interface*. *Chem. Commun.*, 2021. **57**(64): p. 7890-7893.

19. Kresse, G. and J. Furthmüller, *Efficiency of ab-initio total energy calculations for metals and semiconductors using a plane-wave basis set*. *Comput. Mater. Sci.*, 1996. **6**(1): p. 15-50.
20. Kresse, G. and J. Furthmüller, *Efficient iterative schemes for ab initio total-energy calculations using a plane-wave basis set*. *Phys. Rev. B*, 1996. **54**(16): p. 11169-11186.
21. Perdew, J.P., K. Burke, and M. Ernzerhof, *Generalized Gradient Approximation Made Simple*. *Phys. Rev. Lett.*, 1996. **77**(18): p. 3865-3868.
22. Grimme, S., S. Ehrlich, and L. Goerigk, *Effect of the damping function in dispersion corrected density functional theory*. *J. Comput. Chem.*, 2011. **32**(7): p. 1456-1465.
23. Song, W., S. Ma, L. Wang, J. Liu, and Z. Zhao, *Theoretical Explanation of the Photogenerated Carrier Separation at the Surface Junction*. *ChemCatChem*, 2017. **9**(23): p. 4340-4344.
24. Sorescu, D.C., W.A. Al-Saidi, and K.D. Jordan, *CO₂ adsorption on TiO₂(101) anatase: A dispersion-corrected density functional theory study*. *J. Chem. Phys.*, 2011. **135**(12): p. 124701.

5

Benzonitrile hydrogenation on $\text{Au}_{13}/\text{TiO}_2$



Density Functional Theory is used to determine the reaction mechanisms of benzonitrile hydrogenation to benzylamine on Au_{13} cluster supported on a rutile TiO_2 (110) catalyst. An Au/TiO_2 interface is identified as an active site for the dissociation of H_2 and the hydrogenation of benzonitrile. The CN moiety of the benzonitrile substrate is polarized by the adsorption to Lewis acidic Ti center. The generated hydride-proton pair is necessary for reducing the polar CN moiety, facilitating the subsequent hydrogenation reaction.

This chapter is partially based on ACS Catal, 2021, 11(13), 7672-7684.

5.1 Introduction

Benzylamine is an important chemical compound with widespread applications in the textile, agrochemical, and pharmaceutical industries [1, 2]. There are three main classical production paths of benzylamine summarized in Figure 5.1. The first method is the chlorination of toluene to benzyl chloride, followed by the reaction with ammonia to produce the target benzylamine compound [2, 3]. Despite its simplicity, the use of toxic chlorine gas as the key reagent as well as the accompanying non-selective conversion and generation of substantial amounts of inorganic wastes render this method the least environmentally friendly. The second route starts with the high-temperature ammoxidation of toluene to benzonitrile followed by the catalytic hydrogenation to form benzylamine. Alternatively, the selective oxidation of toluene can be used to generate benzaldehyde, which is then converted to benzylamine via the reductive amination reaction. Although the latter two methods are substantially more environmentally friendly and efficient, there are some significant drawbacks. The ammoxidation of toluene to benzonitrile is limited mostly to nonfunctionalized substrates due to the high temperature and pressure used [4, 5]. Whereas the formation of benzaldehyde can be performed under relatively mild conditions, it suffers from overoxidation to benzoic acid [6].

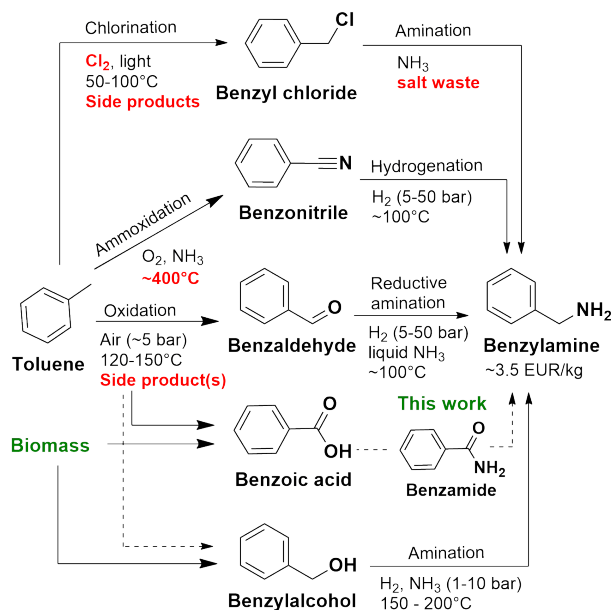


Figure 5.1 An overview of benzylamine synthesis methods [7].

In the past decades, many studies have attempted to synthesize benzylamine efficiently from green and renewable resources under milder conditions. An attractive substrate for such a process is the biomass-derived benzyl alcohol that can be converted to benzylamine via the direct amination reaction with yields ranging between 66–86% [8–14]. An even more desirable substrate is benzoic acid which is generally more abundant, cheaper, and readily obtained from renewable feedstocks [15, 16]. Conventional routes from the benzoic acid or its derivatives to benzylamine would require multistep synthetic procedures and/or the use of stoichiometric reducing agents, inevitably resulting in selectivity losses and/or substantial waste generation. A catalytic conversion path utilizing molecular H_2 as the reducing and NH_3 as the amination agent is highly desirable for high atom- and energy efficiency.

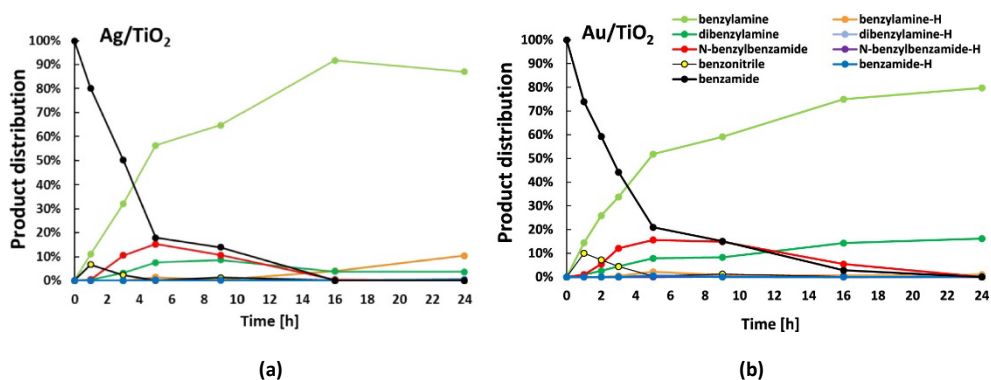


Figure 5.2 Time profiles for the hydrogenation of benzamide with (a) Ag/TiO_2 and (b) Au/TiO_2 . Reaction conditions: benzamide (2 mmol), 200 °C, 6 bar NH_3 , 30 bar H_2 (Au) or 50 bar H_2 (Ag), 1 mol % Au (1 wt % Au catalyst) or 5 mol % Ag (2.5 wt % Ag catalyst), undecane (internal standard, 40 μL), and CPME (20 mL). (Product names ending with “-H” have at least one aromatic ring that is hydrogenated toward a cyclohexyl moiety.) [7]

Previous studies demonstrated that hydrogenation and reductive amination of aliphatic amides and carboxylic acids could indeed provide a sustainable route to amines [17, 18]. However, these methodologies based on noble metal catalysts such as Ru, Rh, Pd, and Pt were not applicable to the conversion of aromatic substrates because of their high reactivity towards the aromatic ring hydrogenation. Very recently, the experimental studies by De Vos group at KU Leuven identified Ag/TiO_2 and Au/TiO_2 as highly efficient catalysts for the reductive amination of benzoic acid and its derivatives (e.g. benzamide) to produce benzylamine by using only H_2 and NH_3 as the reagents [7]. In particular, the experimental studies demonstrated high selectivity for conversion of benzamide to

benzylamine in the presence of H_2 and NH_3 over TiO_2 -supported Au and Ag catalysts. At the high conversion levels, the formation of dibenzylamine and *N*-benzylbenzamide was observed, while no notable over hydrogenation activity of the aromatic ring was detected (Figure 5.2). The optimized reaction conditions allowed obtaining benzylamine in yields ranging 80-92%. The experimental analysis has led to a mechanistic proposal for the direct catalytic conversion of benzamide to benzylamine illustrated in Figure 5.3, in which the specific role of Au/ TiO_2 catalyst was ascribed to the highly selective and efficient hydrogenation of the polar $-\text{CN}$ moiety in the benzamide intermediate. However, the origin of this unique reactivity and the role of the multifunctional interface in it were unclear. To clarify these issues and provide mechanistic support to our experimental collaborators from the de Vos group, I investigated the mechanism of benzonitrile hydrogenation to benzylamine over a model Au/ TiO_2 catalyst by periodic Density Functional Theory (DFT) calculations.

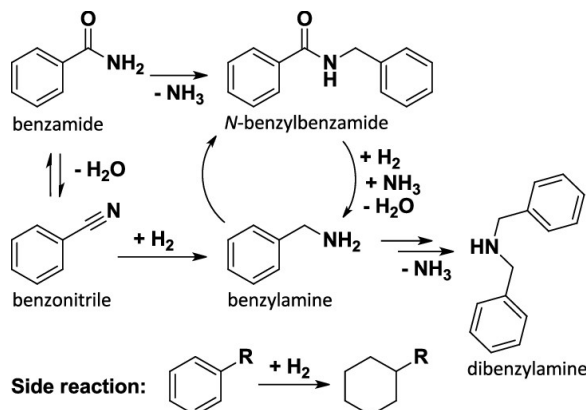


Figure 5.3 Reaction scheme for the hydrogenation of benzamide to benzylamine [7].

5.2 Computational details

All periodic Density Functional Theory (DFT) calculations were carried out using the Vienna Ab Initio Simulation Package (VASP) 5.3.5 [19, 20]. The generalized gradient approximation (GGA) with PBE exchange-correlation functional was used [21]. Grimme's DFT-D3 method with Becke-Jonson damping was used to account for the dispersion interactions [22]. The on-site Coulomb interaction was included using the DFT+U method with a Hubbard parameter of $U = 4.2$ eV for the Ti atoms [23]. The kinetic energy cutoff of the plane wave basis set was set to 400 eV. The threshold for the energy convergence for each electronic optimization iteration

was set to 10^{-5} eV, while the geometry optimizations were assumed to be converged when forces on each atom were less than 0.05 eV/Å.

The Gibbs free energy profiles were estimated by considering only the entropy losses due to the adsorption of molecular species on the catalyst surface and the formation of the adsorption complex ($G_{complex}$), which were calculated by:

$$G_{complex} = [E_{complex} - E_{Au_{13}/TiO_2} - \sum (E_{adsorbate} + TS_{rot} + TS_{trans})]$$

where $E_{complex}$, E_{Au_{13}/TiO_2} , and $E_{adsorbate}$ are the electronic energy of adsorption complex, bare Au_{13}/TiO_2 and the adsorbate, respectively. The TS_{rot} and TS_{trans} are the rotational and translational entropy contribution to the energy of the gas-phase adsorbate at the corresponding reaction temperature, respectively. Note, that the zero-point energy (ZPE) is neglected in our calculations.

To construct the model of Au_{13}/TiO_2 catalyst, the rutile TiO_2 (110) surface with a p(3x5) supercell size as the support following the experimental results. The Au_{13} cluster size was selected because it is small enough to be computationally feasible and large enough to provide a hemispherical shape in contact with the substrate, mimicking that seen in experiments [24]. In addition, the Au_{13} has been used as a representative of supported Au particles on TiO_2 for the chemoselective hydrogenation of nitroaromatic compounds [25]. Previous DFT study demonstrated that the supported Au_{13} cluster could form either planar (2D) or 3D structures on the TiO_2 (110) surface [26, 27]. Therefore, both configurations were considered in this study. For the 3D Au_{13} cluster supported on TiO_2 , three different configurations (Figure 5.4) were constructed and deposited on the TiO_2 (110) surface. These starting configurations were selected based on the literature data [28, 29]. The DFT calculations revealed that the planar Au_{13} -2D/ TiO_2 (Figure 5.5a) is 0.62 eV more stable than the most favorable 3D structure of Au_{13} cluster on TiO_2 (Au_{13} -3D/ TiO_2 , Figure 5.5b). Thus, both Au_{13} -2D/ TiO_2 and Au_{13} -3D/ TiO_2 structures were considered as representative model catalysts in the mechanistic analysis of the catalytic benzonitrile hydrogenation because the energy difference is not very significant.

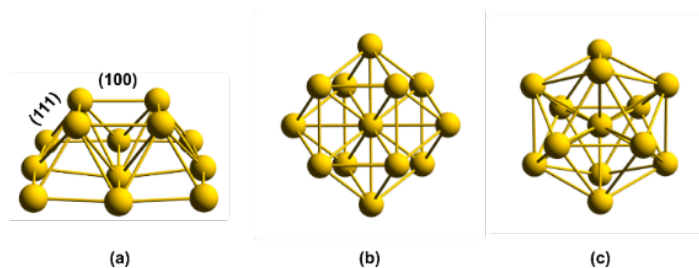


Figure 5.4 Optimized structures of Au_{13} -3D cluster with different geometry. **(a)** Au_{13} cluster as extracted from bulk Au, **(b)** octahedral Au_{13} cluster, and **(c)** icosahedral Au_{13} cluster.

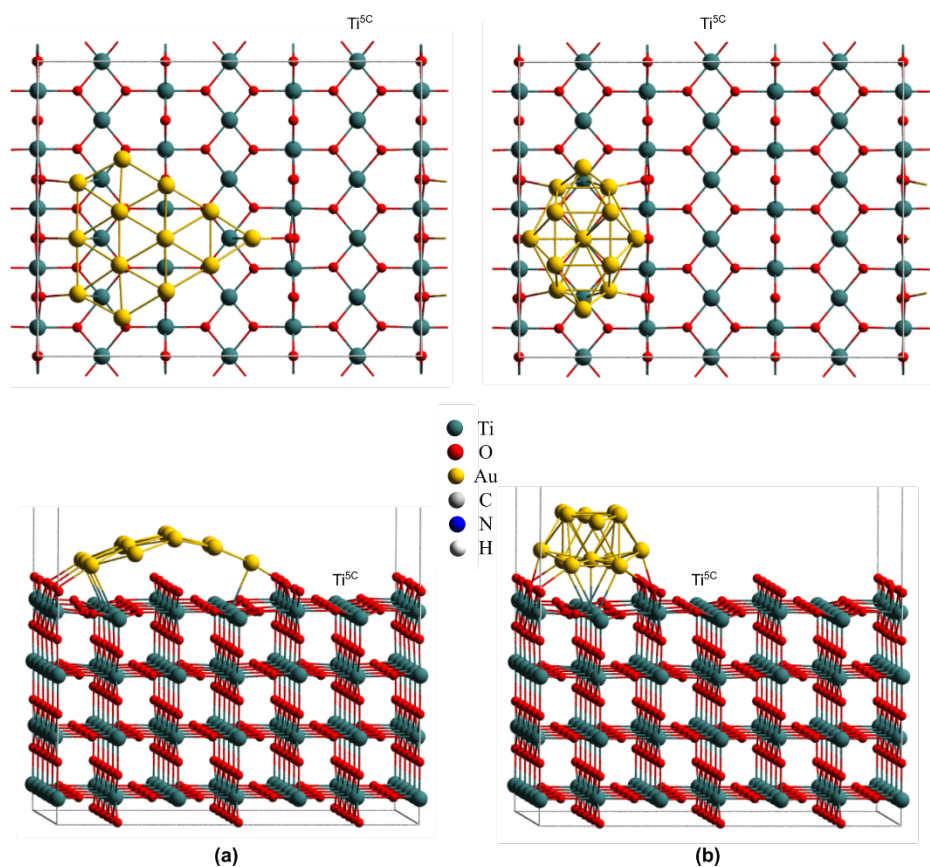


Figure 5.5 Structural configurations of Au_{13} clusters deposited on the stoichiometric rutile TiO_2 (110) surface. **(a)** top and side view of Au_{13} -2D/ TiO_2 . **(b)** top and side view of the most stable configuration of Au_{13} -3D/ TiO_2 .

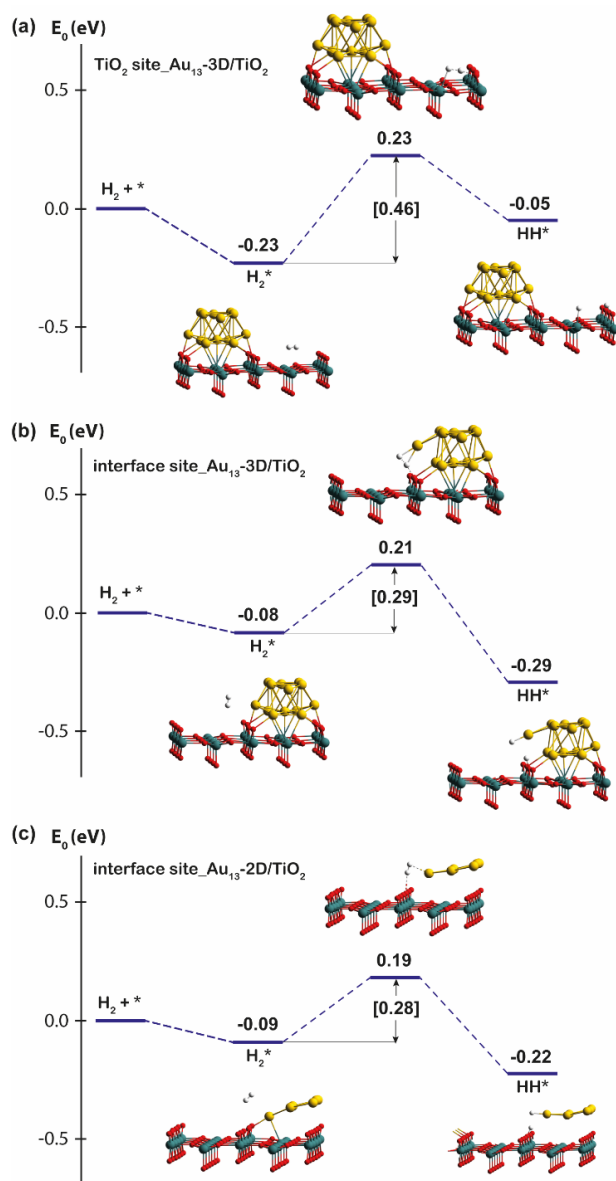


Figure 5.6 DFT-computed reaction energy profiles of H_2 dissociation on (a) a TiO_2 site and (b) interfacial sites of Au_{13} -3D/ TiO_2 , and on (c) an interfacial site of Au_{13} -2D/ TiO_2

5.3 Results and Discussion

5.3.1 H₂ dissociation on Au₁₃/TiO₂

Previous studies of H₂ dissociation on bare rutile TiO₂ (110) [30] and Au/TiO₂ (110) [31, 32] found that the heterolytic dissociation is favored in comparison with the homolytic H₂ activation. Thus, only the former mechanism, which is the H₂ cleavage to produce a couple of proton (H⁺) and hydride (H⁻) was considered in this study. The results in Chapter 2 also suggest that such a heterolytic H₂ cleavage can be promoted both by the Lewis acid-base sites of the support itself or by the metal-titania interface sites. Therefore, three alternative sites were considered for H₂ dissociation by Au/TiO₂ (Figure 5.6), namely (a) the Ti_{5c}-O_{2c} pair site of the TiO₂ support, as well as (b) the Au(3D)-O_{2c} and (c) Au(2D)-O_{2c} interface sites for the 3D and 2D supported Au cluster models, respectively. The DFT calculations show that the heterolytic H₂ dissociation at the Au/TiO₂ interface site is exothermic, while that reaction at the TiO₂ surface site is endothermic. The calculated activation energy of H-H bond cleavage at the Ti_{5c}-O_{2c} pair site ($E_a = 0.46$ eV) is about one time higher than that over the Au-O_{2c} pair sites ($E_a = 0.29$ - 0.28 eV). Therefore, our calculations show that the H₂ dissociation at the interfacial Au-O_{2c} sites is both thermodynamically and kinetically more favorable than at the Ti_{5c}-O_{2c} pair site. Furthermore, we found that the geometry of the supported Au₁₃ clusters does not affect the activation and the reaction energy of H₂ dissociation. Both Au₁₃-2D/TiO₂ and Au₁₃-3D/TiO₂ show very similar catalytic activity for this step.

Compared with the results of heterolytic H₂ dissociation on Cd/TiO_{2(anatase)} (Chapter 2), Au/TiO_{2(rutile)} is more active for the dissociation of H₂ molecule. The activation energy of H-H bond cleavage at the Au/TiO₂ interface site is about 0.1 eV lower than that of the Cd/TiO₂ interface. In addition, this reaction at Au/TiO₂ interface sites is exothermic ($\Delta E_{rxn}@Au_{13}$ -2D/TiO₂ = -0.13 eV, $\Delta E_{rxn}@Au_{13}$ -3D/TiO₂ = -0.21 eV) while that reaction at Cd/TiO₂ interface sites is endothermic (0.15, 0.02, and 0.19 eV for sites B, C, and D, respectively). These results indicate that the catalytic activity of metal/oxides depends on the type and nature of both metal and oxide support.

5.3.2 Adsorption of benzonitrile on Au₁₃/TiO₂

Next, the molecular adsorption of benzonitrile (PhCN) on the surface of Au₁₃-3D/TiO₂ was analyzed to identify the starting configurations for the catalytic reaction. We considered ten different adsorption configurations resulting in the optimized structures shown in Figure 5.7. Our DFT calculations indicate that PhCN

preferentially binds to the Lewis acidic Ti_{5c} surface site of the support in an end-on fashion rather than coordinating with the atoms of the supported Au cluster. The metallic surface stabilizes the TiO_2 -adsorbed species through the interaction with the π system of the aromatic ring. The coordination of PhCN to Ti_{5c} surface sites shows adsorption energies in the range of -1.13 to -1.53 eV. Among adsorption modes, the complexes PhCN_3D_Ti-1, PhCN_3D_Ti-2, and PhCN_3D_Ti-3 formed near the supported Au_{13} cluster are found to be the three most stable structures (-1.37, -1.52 and -1.53 eV), which is ca. 0.2-0.4 eV more favorable than the adsorption to the distant Ti_{5c} sites. This energy difference is close to the energy values computed for PhCN physisorbed to Au sites (-0.23 – -0.59 eV). Note that the most stable configuration, in this case, is obtained for the configuration featuring PhCN physisorbed at the Au/ TiO_2 interface, but with the basic -CN moiety pointing opposite to the Lewis acidic Ti sites.

A similar analysis of PhCN adsorption to the Au_{13} -2D/ TiO_2 model has provided us with five distinct adsorption configurations summarized in Figure 5.8. In line with the discussion above, the most favorable adsorption mode in the current case is realized for the coordination of the CN group of PhCN in an end-on mode to the surface sites with the preferential binding to the Lewis acidic Ti_{5c} site (PhCN_2D_Ti-1 and PhCN_2D_Ti-2). The DFT computed adsorption energies for these modes are in the range of -1.28 to -1.45 eV. In line with the higher stability of the Au_{13} -2D/ TiO_2 structure compared to the Au_{13} -3D/ TiO_2 , a somewhat weaker PhCN adsorption is predicted for the former model. For other configurations, the parallel adsorption of PhCN to the gold surface of the supported 2D Au_{13} cluster is less favorable (PhCN_2D_Au-1 and PhCN_2D_Au-2) with the computed adsorption energies of -0.55 and -0.63 eV, respectively. The alternative end-on adsorption mode of PhCN to Au surface site (PhCN_2D_Au-3) gives rise to the least stable configuration with the adsorption energy of -0.33 eV.

In summary, the DFT analysis of PhCN adsorption to Au_{13} -3D/ TiO_2 and Au_{13} -2D/ TiO_2 systems reveals that these species preferentially adsorb the PhCN substrate to the Lewis acidic Ti_{5c} site at the Au/ TiO_2 interface, which features the Au- O_{2c} Lewis acid-base pairs necessary for the heterolytic H_2 cleavage. We propose that such preferred coordination and polarization of the PhCN substrate near the H_2 dissociation sites provide a favorable channel for further highly selective reduction of the polar CN group. To probe this hypothesis, we further investigated the catalytic reduction of PhCN, starting with the most stable adsorption configurations for both Au_{13} -3D/ TiO_2 and Au_{13} -2D/ TiO_2 structures.

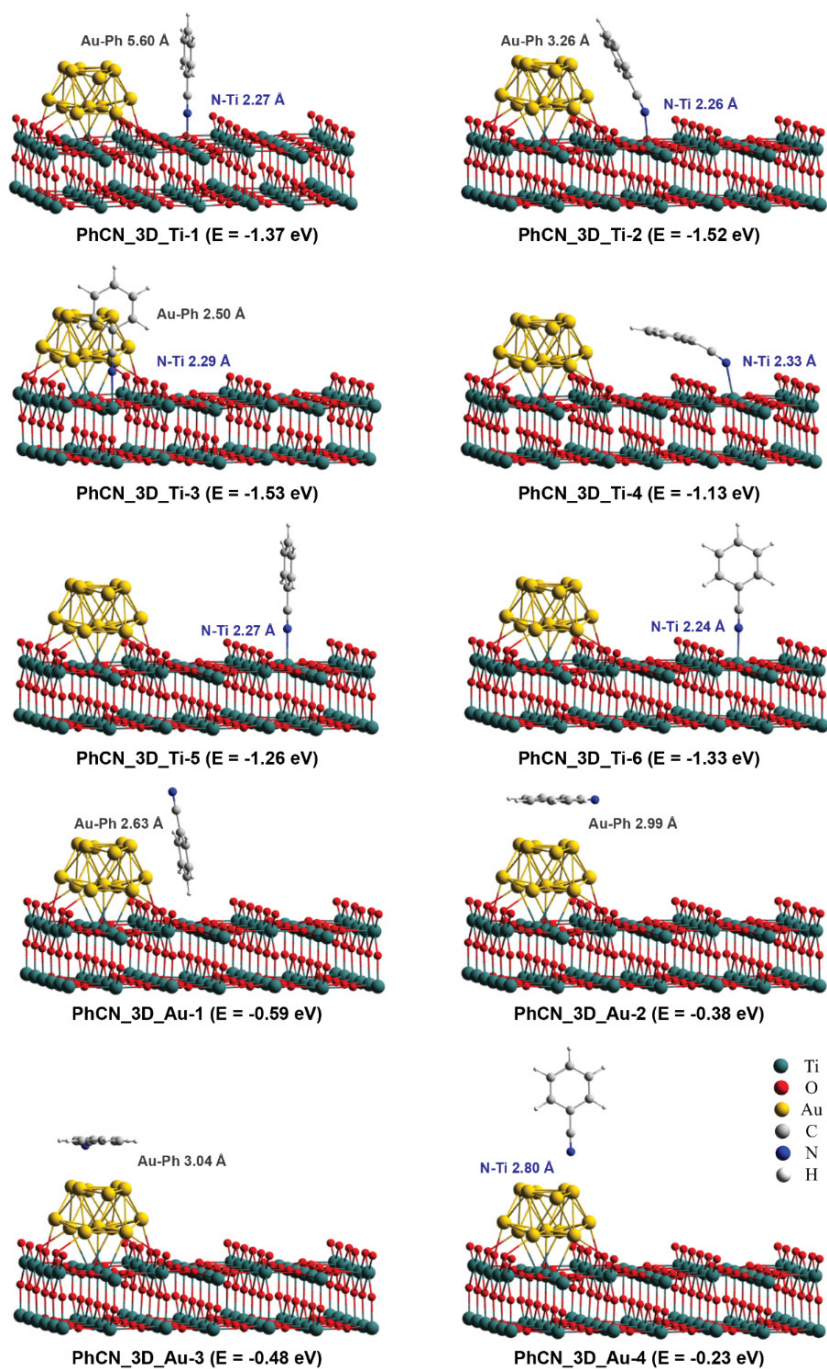


Figure 5.7 The optimized structures of benzonitrile (PhCN) adsorbed on different sites of $\text{Au}_{13}\text{-3D}/\text{TiO}_2$

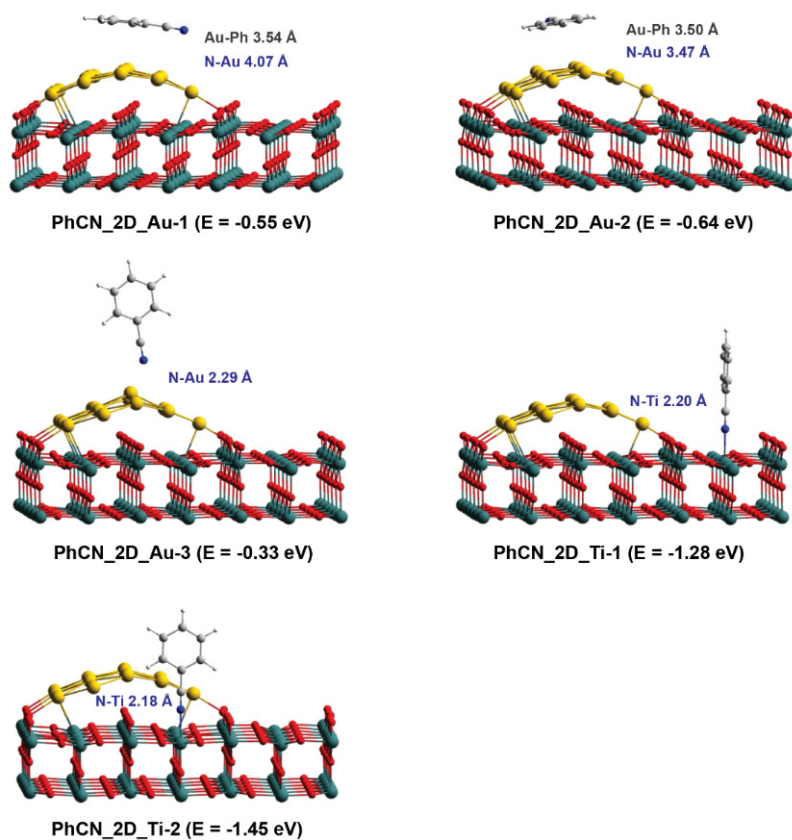


Figure 5.8 The optimized structure of benzonitrile (PhCN) adsorption on different sites of Au₁₃-2D/TiO₂ catalyst

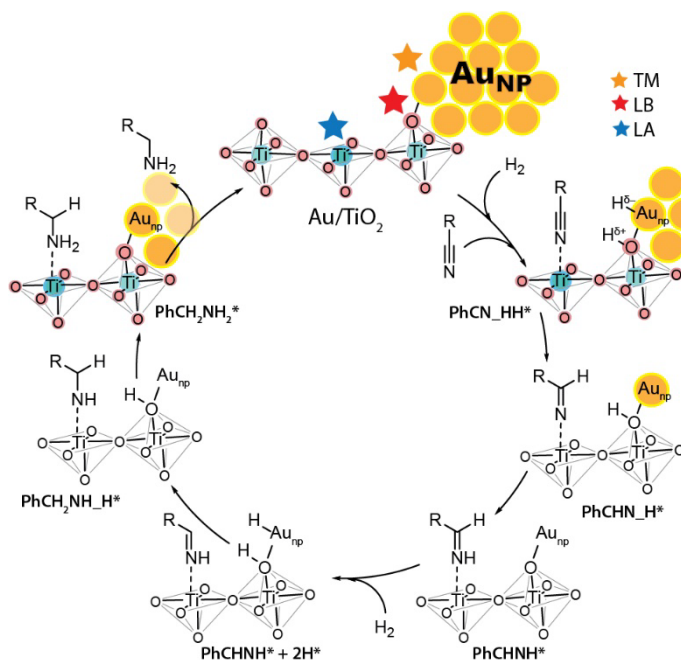


Figure 5.9 The proposed mechanism of benzonitrile hydrogenation at the Au/TiO₂ interface

5.3.3 Benzonitrile hydrogenation on Au₁₃/TiO₂

The reaction mechanism of benzonitrile (PhCN) hydrogenation to benzylamine (PhCH₂NH₂) is schematically presented in Figure 5.9. The synergy of the Lewis acid and base sites of the titania support and the metallic Au nanoparticle is proposed to play an important role in the heterolytic cleavage of H₂ and subsequent selective hydrogenation of the polar nitrile moiety. We propose that the hydrogenation of PhCN proceeds in four consecutive hydride and proton transfer reaction steps, forming PhCHN, PhCHNH, PhCH₂NH, and the final product PhCH₂NH₂. Firstly, the conversion of PhCN to PhCHN via a hydride transfer is studied on two different catalytic models (Au₁₃-3D/TiO₂ and Au₁₃-2D/TiO₂). Figure 5.10 shows that the first intermediate PhCHN is easily generated on the Au₁₃-3D/TiO₂ with small activation energy ($E_a = 0.10$ eV). In contrast, the same reaction on Au₁₃-2D/TiO₂ requires much higher activation energy ($E_a = 1.36$ eV). This result implies that the Au₁₃-3D/TiO₂ is the preferred catalytic model for the hydrogenation of PhCN even though the supported Au₁₃ cluster with the 3D structure is less stable than the planar structure. Hence, the full catalytic cycle is further determined by using only the Au₁₃-3D/TiO₂ catalytic structure.

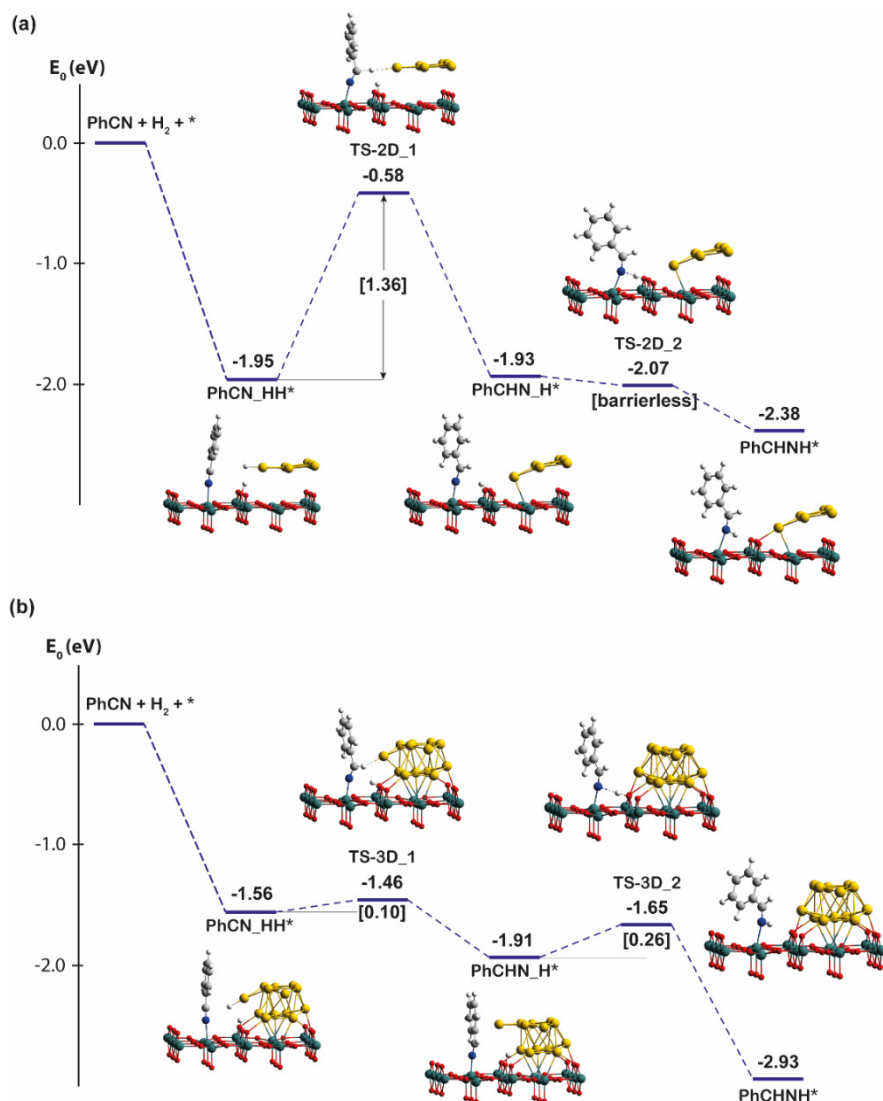


Figure 5.10 Reaction energy profiles of PhCN hydrogenation on (a) Au₁₃-2D/TiO₂ and (b) Au₁₃-3D/TiO₂ catalysts

The complete reaction energy profile of PhCN hydrogenation to produce PhCH₂NH₂ is illustrated in Figure 5.11. The end-on coordination of PhCN to the Lewis acidic Ti_{5c} site polarizes and activates the CN moiety facilitating thus the hydride transfer step. Indeed, once the H^{δ+}...H^{δ-} pair is generated at the interface site, the subsequent PhCN hydrogenation is energetically favorable and proceeds with small activation barriers of 0.10 eV and 0.26 eV for the hydride and proton

transfer steps, respectively. Further reduction of the benzyliimine intermediate (PhCHNH) to benzylamine (PhCH_2NH_2) is barrierless. However, the desorption of the PhCH_2NH_2 product and the regeneration of the Lewis acidic Ti site is quite endothermic by 2.25 eV. By accounting for the translational and rotational entropy gains due to the product desorption at 200 °C, we estimate the Gibbs free energy for this final step to be only 1.11 eV, as shown in Figure 5.12. These DFT results indicate that the synergetic action of the multifunctional active sites at the Au-TiO₂ interface is the key for selective nitrile hydrogenation.

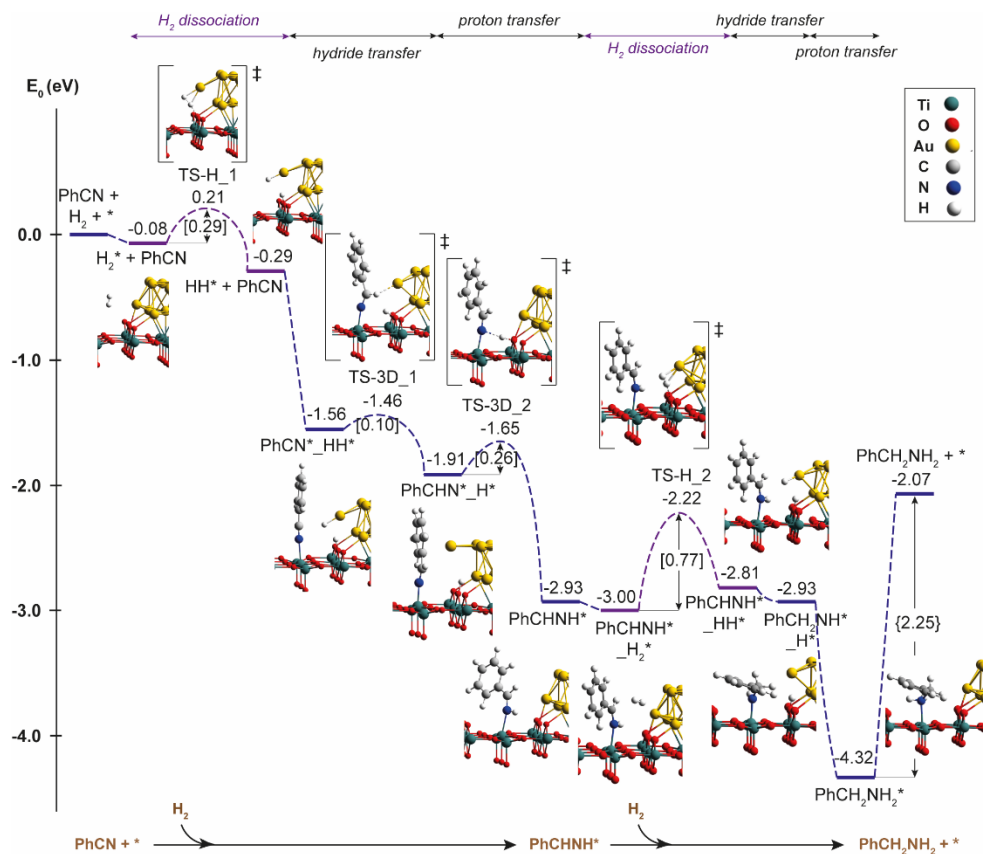


Figure 5.11 Reaction energy profile of the catalytic reduction of benzonitrile (PhCN) to benzylamine (PhCH_2NH_2) on the Au₁₃-3D/TiO₂

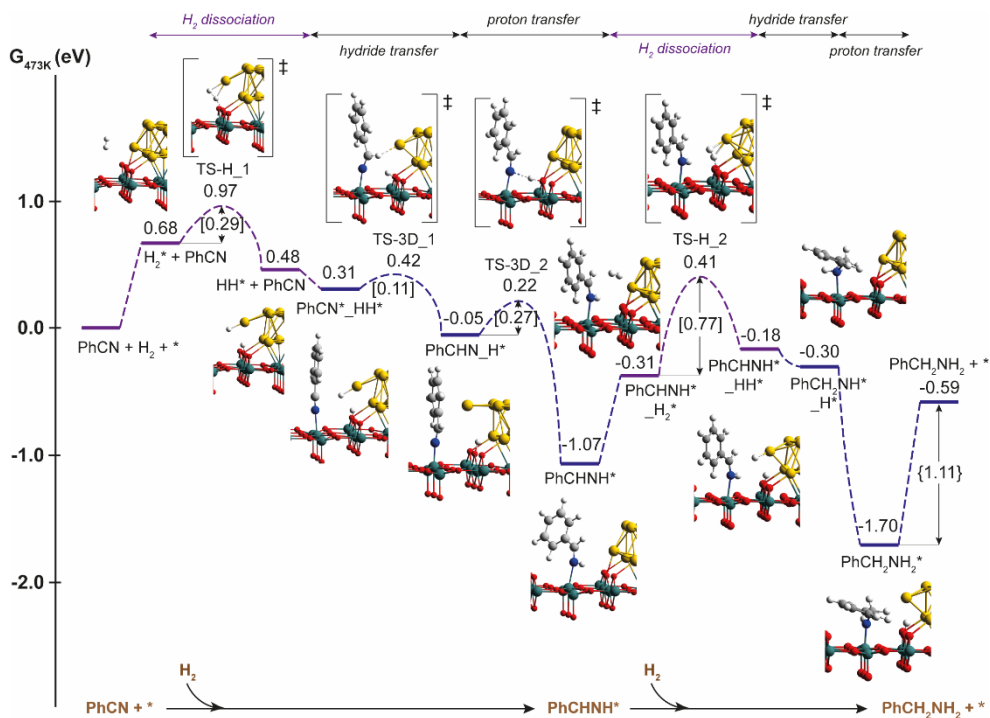


Figure 5.12 Reaction Gibbs free energy profile for benzonitrile hydrogenation to benzylamine (PhCN + 2H₂ → PhCH₂NH₂) on the Au₁₃/TiO₂ catalyst.

5.4 Conclusion

In summary, the catalytic activity of Au₁₃/TiO₂ for the benzonitrile hydrogenation to benzylamine was investigated by using periodic DFT calculations. We found that the Au/TiO₂ interface is the critical active site for the dissociation of H₂, while the benzonitrile tends to be adsorbed in the end-on configuration at the interfacial Ti_{5c} site via its CN moiety. The generated hydride and proton from the heterolytic cleavage of H₂ are essential for reducing the polar CN moiety, facilitating the subsequent hydrogenation reaction. Furthermore, we found that the geometry of the Au₁₃ cluster has a negligible effect on the activation energy of H₂ dissociation but has a significant impact on the hydrogenation of benzonitrile. The DFT calculations provide detailed mechanisms, while the descriptions of the catalytic role of each functional component clarify the catalytic reactivity. This information is useful for guiding the experiment and rationalizing the catalyst design for selective nitriles hydrogenation.

References

1. Nair, U.R., R. Sivabalan, G.M. Gore, M. Geetha, S.N. Asthana, and H. Singh, *Hexanitrohexaazaisowurtzitane (CL-20) and CL-20-based formulations (review)*. *Combust. Explos. Shock Waves*, 2005. **41**(2): p. 121-132.
2. Heuer, L., Benzylamine, in *Ullmann's Encyclopedia of Industrial Chemistry*. 2006.
3. Xungang, G., L. Guoqing, L. Shaosuo, L. Yinghui, L. Xuefeng, W. Gang, X. Song, and Z. Yunbing, *Method for synthesizing benzyl chloride*. *Patent CN109721466A*. 2019: China.
4. Anbarasan, P., T. Schareina, and M. Beller, *Recent developments and perspectives in palladium-catalyzed cyanation of aryl halides: synthesis of benzonitriles*. *Chem. Soc. Rev.*, 2011. **40**(10): p. 5049-5067.
5. Sundermeier, M., A. Zapf, S. Mutyala, W. Baumann, J. Sans, S. Weiss, and M. Beller, *Progress in the Palladium-Catalyzed Cyanation of Aryl Chlorides*. *Eur. J. Chem.*, 2003. **9**(8): p. 1828-1836.
6. Lv, J., Y. Shen, L. Peng, X. Guo, and W. Ding, *Exclusively selective oxidation of toluene to benzaldehyde on ceria nanocubes by molecular oxygen*. *Chem. Commun.*, 2010. **46**(32): p. 5909-5911.
7. Coeck, R., J. Meeprasert, G. Li, T. Altantzis, S. Bals, E.A. Pidko, and D.E. De Vos, *Gold and Silver-Catalyzed Reductive Amination of Aromatic Carboxylic Acids to Benzylic Amines*. *ACS Catal.*, 2021. **11**(13): p. 7672-7684.
8. Pugh, S., R. McKenna, I. Halloum, and D.R. Nielsen, *Engineering Escherichia coli for renewable benzyl alcohol production*. *Metab. Eng. Commun.*, 2015. **2**: p. 39-45.
9. Fujita, K.-i., S. Furukawa, N. Morishima, M. Shimizu, and R. Yamaguchi, *N-Alkylation of Aqueous Ammonia with Alcohols Leading to Primary Amines Catalyzed by Water-Soluble N-Heterocyclic Carbene Complexes of Iridium*. *ChemCatChem*, 2018. **10**(9): p. 1993-1997.
10. Gunanathan, C. and D. Milstein, *Selective Synthesis of Primary Amines Directly from Alcohols and Ammonia*. *Angew. Chem. Int. Ed.*, 2008. **47**(45): p. 8661-8664.
11. Imm, S., S. Bähn, M. Zhang, L. Neubert, H. Neumann, F. Klasovsky, J. Pfeffer, T. Haas, and M. Beller, *Improved Ruthenium-Catalyzed Amination of Alcohols with Ammonia: Synthesis of Diamines and Amino Esters*. *Angew. Chem. Int. Ed.*, 2011. **50**(33): p. 7599-7603.
12. Liu, Y., A. Afanasenko, S. Elangovan, Z. Sun, and K. Barta, *Primary Benzylamines by Efficient N-Alkylation of Benzyl Alcohols Using Commercial Ni Catalysts and Easy-to-Handle Ammonia Sources*. *ACS Sustain. Chem. Eng.*, 2019. **7**(13): p. 11267-11274.

13. Shimizu, K.-I., K. Kon, W. Onodera, H. Yamazaki, and J.N. Kondo, *Heterogeneous Ni Catalyst for Direct Synthesis of Primary Amines from Alcohols and Ammonia*. *ACS Catal.*, 2013. **3**(1): p. 112-117.
14. Shimizu, K.-I., S. Kanno, K. Kon, S.M.A. Hakim Siddiki, H. Tanaka, and Y. Sakata, *N-alkylation of ammonia and amines with alcohols catalyzed by Ni-loaded CaSiO₃*. *Catal. Today*, 2014. **232**: p. 134-138.
15. Arceo, E., J.A. Ellman, and R.G. Bergman, *A Direct, Biomass-Based Synthesis of Benzoic Acid: Formic Acid-Mediated Deoxygenation of the Glucose-Derived Materials Quinic Acid and Shikimic Acid*. *ChemSusChem*, 2010. **3**(7): p. 811-813.
16. Pfennig, T., J.M. Carraher, A. Chemburkar, R.L. Johnson, A.T. Anderson, J.-P. Tessonnier, M. Neurock, and B.H. Shanks, *A new selective route towards benzoic acid and derivatives from biomass-derived coumalic acid*. *Green Chem.*, 2017. **19**(20): p. 4879-4888.
17. Coeck, R., S. Berden, and D.E. De Vos, *Sustainable hydrogenation of aliphatic acyclic primary amides to primary amines with recyclable heterogeneous ruthenium–tungsten catalysts*. *Green Chem.*, 2019. **21**(19): p. 5326-5335.
18. Coeck, R. and D.E. De Vos, *One-pot reductive amination of carboxylic acids: a sustainable method for primary amine synthesis*. *Green Chem.*, 2020. **22**(15): p. 5105-5114.
19. Kresse, G. and J. Furthmüller, *Efficiency of ab-initio total energy calculations for metals and semiconductors using a plane-wave basis set*. *Comput. Mater. Sci.*, 1996. **6**(1): p. 15-50.
20. Kresse, G. and J. Furthmüller, *Efficient iterative schemes for ab initio total-energy calculations using a plane-wave basis set*. *Phys. Rev. B*, 1996. **54**(16): p. 11169-11186.
21. Perdew, J.P., K. Burke, and M. Ernzerhof, *Generalized Gradient Approximation Made Simple*. *Phys. Rev. Lett.*, 1996. **77**(18): p. 3865-3868.
22. Grimme, S., S. Ehrlich, and L. Goerigk, *Effect of the damping function in dispersion corrected Density Functional Theory*. *J. Comput. Chem.*, 2011. **32**(7): p. 1456-1465.
23. Song, W., S. Ma, L. Wang, J. Liu, and Z. Zhao, *Theoretical Explanation of the Photogenerated Carrier Separation at the Surface Junction*. *ChemCatChem*, 2017. **9**(23): p. 4340-4344.
24. Hong, S. and T.S. Rahman, *Rationale for the Higher Reactivity of Interfacial Sites in Methanol Decomposition on Au₁₃/TiO₂(110)*. *J. Am. Chem. Soc.*, 2013. **135**(20): p. 7629-7635.
25. Boronat, M., P. Concepción, A. Corma, S. González, F. Illas, and P. Serna, *A Molecular Mechanism for the Chemoselective Hydrogenation of Substituted Nitroaromatics with Nanoparticles of Gold on TiO₂ Catalysts: A*

- Cooperative Effect between Gold and the Support. J. Am. Chem. Soc.*, 2007. **129**(51): p. 16230-16237.
26. Ding, R.-L., J. Jia, and H.-S. Wu, *The growth pattern of Au_n (n=1–20) clusters absorbed on rutile TiO₂ (110) surfaces. Appl. Surf. Sci.*, 2015. **359**: p. 729-735.
27. Boronat, M., F. Illas, and A. Corma, *Active Sites for H₂ Adsorption and Activation in Au/TiO₂ and the Role of the Support. J. Phys. Chem. A*, 2009. **113**(16): p. 3750-3757.
28. Wan, W., X. Nie, M.J. Janik, C. Song, and X. Guo, *Adsorption, Dissociation, and Spillover of Hydrogen over Au/TiO₂ Catalysts: The Effects of Cluster Size and Metal–Support Interaction from DFT. J. Phys. Chem. C*, 2018. **122**(31): p. 17895-17916.
29. Liu, L., Z. Liu, H. Sun, and X. Zhao, *Morphological effects of Au₁₃ clusters on the adsorption of CO₂ over anatase TiO₂(101). Appl. Surf. Sci.*, 2017. **399**: p. 469-479.
30. Hu, G., Z. Wu, and D.-E. Jiang, *First Principles Insight into H₂ Activation and Hydride Species on TiO₂ Surfaces. J. Phys. Chem. C*, 2018. **122**(35): p. 20323-20328.
31. Yang, B., X.-M. Cao, X.-Q. Gong, and P. Hu, *A Density Functional Theory study of hydrogen dissociation and diffusion at the perimeter sites of Au/TiO₂. Phys. Chem. Chem. Phys.*, 2012. **14**(11): p. 3741-3745.
32. Sun, K., M. Kohyama, S. Tanaka, and S. Takeda, *A Study on the Mechanism for H₂ Dissociation on Au/TiO₂ Catalysts. J. Phys. Chem. C*, 2014. **118**(3): p. 1611-1617.

Summary

Computational chemistry provides powerful research tools for catalysis. It potentially allows us to study the structures of the catalytic sites and reaction mechanisms, which are difficult to observe only by experiment. This is particularly true for supported heterogeneous catalysts, of which reactivity and catalytic behavior are directly related to the presence of various functional groups and reactive ensembles on their surfaces. Such surface heterogeneities give rise to the formation of multifunctional reactive ensembles ready to convert substrate molecules to the desired products efficiently. At the same time, the presence of various reactive centers on the surface may contribute to undesirable conversion paths. Understanding the role of the multifunctional reaction environments established on the complex surfaces of supported heterogeneous catalysts is key to formulating design rules for achieving control over their activity and selectivity.

However, the complexity of surface species and the associated chemistry make it particularly challenging to get insights into the nature of the active site and the reaction pathways during the catalytic processes. In this context, computational chemistry provides a unique opportunity to unravel the detailed mechanistic picture of the catalytic phenomenon and understand the specific role and potential synergy between the different components of complex heterogeneous catalyst systems. In this thesis, I applied density functional theory (DFT) calculations to study the role of the multifunctionality of TiO_2 -based catalysts for the valorization of CO_2 and biomass. The main focus lies on the reaction mechanisms, the role of each catalytic component, and how they organically work together to facilitate the specific reaction steps.

In Chapter 2, periodic DFT calculations combined with microkinetic modeling (MKM) were performed to investigate the mechanisms of CO_2 hydrogenation to CH_3OH on Cd_4/TiO_2 catalyst. This catalyst, which was developed by our collaborators, displayed highly selective towards CH_3OH . Herein, we found that the multifunctionality at the Cd-TiO_2 interface, including the Lewis acid of metal and the Lewis base of surface oxygen, is essential for the outstanding performance of Cd/TiO_2 catalyst. H_2 and CO_2 molecules prefer to be activated at the Cd-TiO_2 interface rather than at the TiO_2 surface or Cd cluster. The detailed mechanistic study indicates that the formate pathway dominates over the RWGS pathway for the production of CH_3OH . In the RWGS pathway, the effect of the promotor, which is H_2O , was studied. We found that H_2O is needed to proceed the reaction via the

RWGS pathway. The MKM analysis pointed to the formation of the formaldehyde intermediate in the formate pathway as the rate-limiting reaction step. Surface formate species are identified as the resting state of the whole reaction, which is in line with the experimental observations. The strong binding of such species at the surface is responsible for the high activation energy in the rate-limiting reaction step. Thus, these results suggest that the interaction between support and the metal nanocluster should be fine-tuned to further improve the catalyst performance.

Besides the metal-support interface as a reaction center to activate reactant, the additives of alkali carbonates dispersed on the surface of TiO_2 can also play as promoters to facilitate CO_2 conversion and catalyst regeneration. In Chapter 3, we studied the catalytic activity of $\text{K}_2\text{CO}_3/\text{TiO}_2$, which was observed experimentally as an efficient catalyst for the esterification of benzene with CO_2 and CH_3OH . The bare defective TiO_2 was also investigated because it showed high efficiency but was deactivated rapidly. Here, the effect of the inhibition from the high thermodynamic stability of intermediates that was observed in the previous chapter was clarified. In these catalytic systems, the introduction of oxygen vacancy on TiO_2 surface generates Ti^{3+} as a new active site for the catalyst. The periodic DFT calculations revealed that the catalytic reactivity originates from $\text{Ti}^{3+}/\text{K}^+$ and $\text{Ti}^{3+}/\text{Ti}^{3+}$ pair sites of $\text{K}_2\text{CO}_3/\text{TiO}_2$ and bare defective TiO_2 , respectively. The reaction mechanism of benzene esterification with CO_2 and CH_3OH is composed of two main reactions. The first one is the carboxylation of benzene with CO_2 , while another is the methylation with CH_3OH to produce methyl benzoate. We found that both catalysts can catalyze the reaction with similar activation energies. However, the too-strong binding of products on the bare defective TiO_2 impedes the desorption and regeneration of the active site for the next catalytic cycle. In the case of $\text{K}_2\text{CO}_3/\text{TiO}_2$, the K_2CO_3 species, which partially occupy oxygen vacancies, affect the lowering of the product's adsorption strength and thus prevent catalyst poisoning. From this study, we expect that the unique multifunction of $\text{K}_2\text{CO}_3/\text{TiO}_2$ could be potential for the direct C-C coupling reaction of CO_2 with other less reactive but more abundant hydrocarbons such as CH_4 .

Therefore, to check our hypothesis, in Chapter 4, we extended the study of Chapter 3 to investigate the catalytic activity of $\text{K}_2\text{CO}_3/\text{TiO}_2$ for the same esterification reaction but using CH_4 instead of benzene as the substrate. One can expect that this catalyst could be as active in the conversion of CH_4 as for benzene because of the similarity in their C-H bond energies ($\Delta H_{298}(\text{CH}_4) = 105 \text{ kcal/mol}$, $\Delta H_{298}(\text{C}_6\text{H}_6) = 113 \text{ kcal/mol}$). Direct activation and conversion of CH_4 to chemicals

is extremely challenging because of the high binding energy, high symmetry, and low polarity of the C-H bonds. Moreover, the product is usually more reactive than CH_4 , making it difficult to control the selectivity and avoid over activation of the desired products. Thus, the conversion of CH_4 has been a challenge in chemical synthesis similar to CO_2 . This study highlights the difference in reactivity between benzene and CH_4 . The side reaction of CO production was also investigated to examine the product selectivity. The calculations revealed that, indeed, $\text{K}_2\text{CO}_3/\text{TiO}_2$ could potentially catalyze the esterification of CH_4 with CO_2 and CH_3OH . The activation barriers of all elementary steps are similar to the esterification of benzene, and the manners of reactants activation at the interface of $\text{K}_2\text{CO}_3/\text{TiO}_2$ are also comparable between CH_4 and benzene esterification.

However, in the initial step, the C-H bond carboxylation of CH_4 with CO_2 proceeds in one step, while that of benzene occurs in two-step reactions with the metastable $\text{C}_6\text{H}_6\text{COO}^*$ as an intermediate due to the aromaticity of benzene. The barrier of this step is 0.44 eV lower than the decomposition of CO_2 to CO. Thus, the selectivity towards methyl benzoate is higher than CO formation, which is consistent with the experimental observations. In contrast, in the case of CH_4 , a low selectivity of methyl acetate was predicted because the activation energy of C-H bond carboxylation with CO_2 in CH_4 is 0.06 eV higher than that of CO formation. This result implies that the formation of CO can compete with the CH_4 carboxylation, which is not the case in the carboxylation of benzene. Thus, further modification of this catalyst is required for selective C-H bond carboxylation of methane. We propose that enhancing the Lewis basic strength of surface oxygen atoms by replacing the neighboring Ti^{4+} with a lower-valence cation might be one of the strategies to strengthen the interaction with CH_4 and facilitate the C-H bond dissociation without accelerating the decomposition of CO_2 .

Chapter 5 presents the mechanistic study of benzonitrile hydrogenation on $\text{Au}_{13}/\text{TiO}_2$. This catalyst, which was developed by our experimental collaborators, exhibited high reactivity and selectivity for the conversion of benzonitrile to benzylamine. In our work, we applied the knowledge about multifunctional TiO_2 -supported catalysts to study the conversion of more complicated substrates. In this catalytic system, the reactivity is due to the synergistic effect of Lewis acid and Lewis base at the Au/TiO_2 interface. We also examined the geometrical effects of the supported Au_{13} cluster. The calculations reveal that the geometry of the Au_{13} cluster has a minor effect on the activation energy of H_2 dissociation but a significant impact on the hydrogenation of benzonitrile.

We have shown that multiple functionalities in heterogeneous catalysts are responsible for both positive aspects, such as reactant activation and intermediate stabilization; and negative aspects, such as catalyst deactivation, low product selectivity, and undesired products. Therefore, understanding the role of each function on catalysts can help us facilitate those desired aspects and prevent those undesired phenomena by controlling the very complex chemical transformations along low-energy reaction pathways. Designing the multifunctionality and understanding how it helps the desirable conversions is a key to rational catalyst design. The challenges are to learn how to construct these multifunctional ensembles, ensure that they do not degrade during performing, and maintain their performances over a prolonged period of time.

So far, most DFT studies have been performed to provide mechanistic details of catalytic processes under ultra-high vacuum and 0 K conditions. However, over the past decades, computational catalysis has evolved toward studying catalytic processes under working conditions. In our works, combining DFT with MKM allows us to convert microscopic reaction mechanism data into experimentally measurable parameters such as key reaction intermediates and rate-limiting steps. This is a practical way to bridge the gap between static DFT modeling and realistic reaction under catalyst working conditions. We prospect that global optimization methods and *operando* methodologies such as *ab initio* thermodynamics and molecular dynamics would offer more options to further narrow the gap between modeling and experiment by including reaction conditions in the simulation.

Samenvatting

Computationale chemie levert krachtige onderzoekshulpmiddelen voor katalyse. Dankzij computationale chemie kunnen we de structuren bestuderen van de katalytische centra en reactiemechanismen, die met alleen experimenten moeilijk waar te nemen zijn. Dit geldt met name voor gedragen heterogene katalysatoren, waarvan de reactiviteit en het katalytisch gedrag direct verband houden met de aanwezigheid van diverse functionele groepen en reactieve ensembles op het oppervlak ervan. Zulke oppervlakteheterogeniteiten geven aanleiding tot de vorming van multifunctionele reactieve ensembles die in staat zijn substraatmoleculen efficiënt om te zetten in de gewenste producten. Tegelijkertijd kan de aanwezigheid van diverse reactieve centra op het oppervlak bijdragen aan ongewenste omzettingroutes. Inzicht in de rol van de multifunctionele reactieomgevingen aan de complexe oppervlakken van gedragen heterogene katalysatoren is essentieel voor het formuleren van ontwerpregels om controle te krijgen over de activiteit en selectiviteit ervan.

De complexiteit van oppervlakte-entiteiten en de bijbehorende chemie maakt het echter bijzonder uitdagend om inzicht te krijgen in de aard van het actieve centrum en de reactieroutes tijdens de katalytische processen. In dit verband levert computationale chemie een unieke mogelijkheid om het gedetailleerde mechanistische beeld van het katalytische fenomeen te ontrafelen en de specifieke rol en potentiële synergie tussen de verschillende componenten van complexe heterogene katalysatorsystemen te begrijpen. In dit proefschrift gebruikte ik berekeningen volgens de dichtheidsfunctietheorie (DFT) om de rol te bestuderen van de multifunctionaliteit van katalysatoren op basis van TiO_2 voor de valorisatie van CO_2 en biomassa. De focus ligt vooral op de reactiemechanismen, de rol van elke katalytische component en hoe die organisch samenwerken om de specifieke reactiestappen mogelijk te maken.

In hoofdstuk 2 werden periodieke DFT-berekeningen in combinatie met microkinetische modellering (MKM) uitgevoerd om de mechanismen van CO_2 -hydrogenering tot CH_3OH op Cd_4/TiO_2 -katalysator te onderzoeken. Deze katalysator, die door onze samenwerkingspartners werd ontwikkeld, vertoonde hoge selectiviteit voor CH_3OH . Hierin vonden we dat de multifunctionaliteit aan het Cd-TiO_2 -grensvlak, met inbegrip van het Lewis-zuur van metaal en de Lewis-base van oppervlaktezuurstof, essentieel is voor de uitstekende prestaties van Cd/TiO_2 -katalysator. H_2 - en CO_2 -moleculen worden bij voorkeur geactiveerd aan het Cd -

TiO₂-grensvlak in plaats van aan het TiO₂-oppervlak of Cd-cluster. De gedetailleerde mechanistische studie geeft aan dat de formiaatroutte dominant is ten opzichte van de RWGS-route voor de productie van CH₃OH. In de RWGS-route werd het effect van de promotor, die H₂O is, bestudeerd. We hebben gevonden dat H₂O nodig is om de reactie via de RWGS-route te laten verlopen. De MKM-analyse wees op de vorming van het formaldehyde-tussenproduct in de formiaatroutte als de snelheidsbepalende reactiestap. Formiaat-entiteiten aan het oppervlak zijn vastgesteld als de rusttoestand van de hele reactie, wat klopt met de experimentele waarnemingen. De sterke binding van zulke entiteiten aan het oppervlak zorgt voor de hoge activeringsenergie in de snelheidsbepalende reactiestap. Deze resultaten suggereren dus dat de interactie tussen drager en het metaalnanocluster nauwkeurig ingesteld zou moeten worden om de prestaties van de katalysator verder te verbeteren.

Naast het metaal-drager-grensvlak als reactiecentrum om reactant te activeren, kunnen de alkalicarbonaat-additieven die op het oppervlak van TiO₂ gedispergeerd zijn, ook als promotor fungeren om de omzetting van CO₂ en de regeneratie van katalysator te vergemakkelijken. In hoofdstuk 3 onderzochten we de katalytische activiteit van K₂CO₃/TiO₂, waarvan experimenteel werd vastgesteld dat het een efficiënte katalysator voor de verestering van benzeen met CO₂ en CH₃OH is. Het kale defectieve TiO₂ werd ook onderzocht omdat het hoge efficiëntie vertoonde, maar snel werd gedeactiveerd. Hier werd het in het vorige hoofdstuk waargenomen effect van de remming door de hoge thermodynamische stabiliteit van tussenproducten verhelderd. In deze katalytische systemen wordt door het inbrengen van zuurstofvacature op het TiO₂-oppervlak Ti³⁺ gegenereerd als een nieuw actief centrum voor de katalysator. De periodieke DFT-berekeningen lieten zien dat de katalytische reactiviteit voortkomt uit respectievelijk Ti³⁺/K⁺ en Ti³⁺/Ti³⁺-paarcentra van K₂CO₃/TiO₂ en kaal defectief TiO₂. Het reactiemechanisme van verestering van benzeen met CO₂ en CH₃OH bestaat uit twee hoofdreacties. De eerste is de carboxylering van benzeen met CO₂ en de andere is de methylering met CH₃OH om methylbenzoaat te produceren. We hebben gevonden dat beide katalysatoren de reactie met vergelijkbare activeringsenergieën kunnen katalyseren. Echter, de te sterke binding van producten aan het kale defectieve TiO₂ verhindert de desorptie en regeneratie van het actieve centrum voor de volgende katalytische cyclus. In het geval van K₂CO₃/TiO₂ zorgen de K₂CO₃-entiteiten, die de zuurstofvacatures gedeeltelijk bezetten, voor verlaging van de adsorptiesterkte van het product en wordt daarmee vergiftiging van de katalysator voorkomen. Op basis van dit onderzoek verwachten we dat de unieke

multifunctionaliteit van $\text{K}_2\text{CO}_3/\text{TiO}_2$ potentie kan hebben voor C-C-koppelingsreactie van CO_2 met minder reactieve, maar meer algemeen voorkomende koolwaterstoffen zoals CH_4 .

Om onze hypothese te controleren, breidden we in hoofdstuk 4 daarom het onderzoek van hoofdstuk 3 verder uit om de katalytische activiteit van $\text{K}_2\text{CO}_3/\text{TiO}_2$ voor dezelfde veresteringsreactie te onderzoeken, maar dan met gebruik van CH_4 in plaats van benzeen als het substraat. Het is te verwachten dat deze katalysator even actief zou kunnen zijn bij de omzetting van CH_4 als voor benzeen, vanwege de vergelijkbare C-H-bindingsenergieën ervan ($\Delta H_{298}(\text{CH}_4) = 105 \text{ kcal/mol}$, $\Delta H_{298}(\text{C}_6\text{H}_6) = 113 \text{ kcal/mol}$). Directe activering en omzetting van CH_4 naar chemische stoffen is extreem uitdagend vanwege de hoge bindingsenergie, hoge symmetrie en lage polariteit van de C-H-bindingen. Bovendien is het product doorgaans reactiever dan CH_4 , waardoor het moeilijk is om de selectiviteit onder controle te krijgen en overmatige activering van de gewenste producten te vermijden. Daarom is de omzetting van CH_4 in de chemische synthese een uitdaging, net als met CO_2 . Dit onderzoek belicht het verschil in reactiviteit tussen benzeen en CH_4 . De nevenreactie van CO-productie werd ook bestudeerd om de productselectiviteit te onderzoeken. Uit de berekeningen bleek dat $\text{K}_2\text{CO}_3/\text{TiO}_2$ de verestering van CH_4 met CO_2 en CH_3OH inderdaad zou kunnen katalyseren. De activeringsbarrières van alle elementaire stappen zijn vergelijkbaar met de verestering van benzeen, en de manieren waarop reactanten aan het grensvlak van $\text{K}_2\text{CO}_3/\text{TiO}_2$ geactiveerd worden, zijn ook vergelijkbaar tussen de verestering van CH_4 en die van benzeen.

Echter, in de eerste stap verloopt de carboxylering van de C-H-binding van CH_4 met CO_2 in één stap, terwijl die van benzeen in tweestapsreacties plaatsvindt met het metastabiele $\text{C}_6\text{H}_6\text{COO}^*$ als tussenproduct als gevolg van de aromaticiteit van benzeen. De barrière van deze stap is 0,44 eV lager dan de ontleding van CO_2 tot CO. Daarom is de selectiviteit voor methylbenzoaat hoger dan de vorming van CO, wat klopt met de experimentele waarnemingen. Daarentegen werd in het geval van CH_4 een lage selectiviteit voor methylacetaat voorspeld, omdat de activeringsenergie van carboxylering van de C-H-binding met CO_2 in CH_4 0,06 eV hoger is dan die van CO-vorming. Dit resultaat impliceert dat de vorming van CO kan concurreren met de carboxylering van CH_4 , wat niet het geval is bij de carboxylering van benzeen. Daarom is verdere modificatie van deze katalysator nodig voor de selectieve carboxylering van de C-H-binding van methaan. We stellen voor dat verhoging van de Lewis-basesterkte van oppervlaktezuurstofatomen door het aangrenzende $\text{Ti}4^+$ te vervangen door een kation met een lagere valentie een van de strategieën zou kunnen zijn om de interactie met CH_4 te versterken en de

dissociatie van de C-H-binding te vergemakkelijken zonder de ontleding van CO₂ te versnellen.

Hoofdstuk 5 beschrijft de mechanistische studie van de hydrogenering van benzonitril op Au₁₃/TiO₂. Deze katalysator, die door onze experimentele samenwerkingspartners werd ontwikkeld, vertoonde hoge reactiviteit en selectiviteit voor de omzetting van benzonitril naar benzylamine. In ons werk pasten we de kennis over multifunctionele, op TiO₂ gedragen katalysatoren toe om de omzetting van complexere substraten te onderzoeken. In dit katalytische systeem is de reactiviteit het gevolg van het synergistische effect van Lewis-zuur en Lewis-base aan het Au/TiO₂-grensvlak. We onderzochten ook de geometrische effecten van het gedragen Au₁₃-cluster. Uit de berekeningen blijkt dat de geometrie van het Au₁₃-cluster een klein effect heeft op de activeringsenergie van H₂-dissociatie, maar een significante impact op de hydrogenering van benzonitril.

We hebben aangetoond dat meerdere functionaliteiten in heterogene katalysatoren verantwoordelijk zijn voor zowel positieve aspecten, zoals activering van reactanten en stabilisatie van tussenproducten, als negatieve aspecten, zoals deactivering van katalysator, lage productselectiviteit en ongewenste producten. Daarom kan inzicht in de rol van elke functie op katalysatoren ons helpen die gewenste aspecten te verbeteren en die ongewenste verschijnselen te voorkomen door de zeer complexe chemische transformaties via laagenergetische reactieroutes te controleren. Het ontwerpen van de multifunctionaliteit en het inzicht in hoe die gunstig is voor de wenselijke omzettingen is een sleutel tot rationeel katalysatorontwerp. De uitdagingen liggen in het leren hoe deze multifunctionele ensembles op te bouwen, te zorgen dat ze niet afbreken tijdens het gebruik en hun prestaties gedurende langere tijd behouden.

Tot dusver zijn de meeste DFT-studies gedaan om mechanistische details van katalytische processen onder omstandigheden van ultrahoog vacuüm en 0 K te leveren. In de afgelopen decennia is computationele katalyse echter geëvolueerd naar het bestuderen van katalytische processen onder werkomstandigheden. In ons werk heeft de combinatie van DFT en MKM ons in staat gesteld gegevens over microscopische reactiemechanismen om te zetten in experimenteel meetbare parameters, zoals belangrijke reactietussenproducten en snelheidsbepalende stappen. Dit is een praktische manier om de kloof te dichten tussen statische DFT-modellering en realistische reacties onder werkomstandigheden van katalysatoren. We verwachten dat algehele optimaliseringsmethoden en *operando*-methoden zoals ab-initio-thermodynamica en moleculaire dynamica

meer mogelijkheden zouden bieden om de kloof tussen modellering en experimenten verder te dichten door reactieomstandigheden in de simulatie op te nemen.

Acknowledgements

This Thesis would have been impossible without the support of many people. My first appreciation goes to my supervisor, Evgeny Pidko, for his supervision, guidance, and support. Sincere gratitude is extended to his patience and encouragement when I was feeling unproductive and unmotivated. I would also like to thank my daily supervisor, Guanna Li, for sharing her knowledge and experience, teaching me many computational techniques, and giving me excellent advice during my Ph.D. journey.

I would like to offer my special thanks to my colleagues for their efforts and contributions to our research. I am thankful to Chong, who greatly helped me in my initial Ph.D. stage. Also, I would like to thank Dapeng, who taught me microkinetic modeling and troubleshooting my python scripts.

I thank all the members of the ISE group for their insightful comments and suggestions in the group meeting. I also thank Annika, Ali, Chong, Elena, and Dapeng for creating a good research atmosphere in the office. I appreciate all the kind people I met in TU Delft and thank them for their help and support.

I acknowledge the National Nanotechnology Center of Thailand and the Royal Thai Government Scholarship for giving me a chance to pursue a doctoral degree. I thank the Thai student community for their help while living in the Netherlands. Also, I thank my friends for their encouragement. Finally, I am grateful to my parents for their unconditional love and support.

Curriculum Vitae

Jittima Meeprasert was born in Bangkok, Thailand, on the 27th of September 1983. In 2005, she graduated from Kasetsart University with a Bachelor's degree in General Science and continued with her Master's degree with a specialization in Physical Chemistry. In 2009, she worked at the National Nanotechnology Center (NANOTEC), a government organization under the National Science and Technology Development Agency, Thailand. In 2017, she received the Royal Thai Government Scholarship and moved to the Netherlands to pursue a Ph.D. research in the Inorganic Systems Engineering group at the Delft University of Technology, under the supervision of prof. dr. Evgeny Pidko. After finishing her Ph.D., she returns to Thailand and continues working as a researcher at the NANOTEC. The results of research in her Ph.D. period are described in this book.

List of Publications

Publications within the scope of this thesis

R. Coeck, **J. Meeprasert**, G. Li, T. Altantzis, S. Bals, E. A. Pidko, and D. E. De Vos, *Gold and Silver-Catalyzed Reductive Amination of Aromatic Carboxylic Acids to Benzylic Amines*. *ACS Catal.*, 2021, **11**(13), 7672-7684.

J. Meeprasert, G. Li, and E. A. Pidko, *Mechanistic investigation of benzene esterification by K_2CO_3/TiO_2 : the catalytic role of the multifunctional interface*. *Chem. Commun.*, 2021, **57**, 7890-7893.

J. Wang, **J. Meeprasert**, Z. Han, H. Wang, Z. Feng, C. Tang, F. Sha, S. Tang, G. Li, E. A. Pidko, and C. Li, *Highly dispersed Cd cluster supported on TiO_2 as an efficient catalyst for CO_2 hydrogenation to methanol*. *Chinese J. Catal.*, 2022, **43**(3), 761-770.

J. Meeprasert, G. Li, J. Wang, C. Li, and E. A. Pidko, *CO_2 Hydrogenation to Methanol over Cd_4/TiO_2 Catalyst: Insight into Multifunctional Interface*. *ChemCatChem*, 2022, **14**, e202101646.

J. Meeprasert, G. Li, and E. A. Pidko, *The direct C-H carboxylation challenge: on the difference in the interaction mechanisms of CO_2 with CH_4 and C_6H_6 on K_2CO_3/TiO_2 catalyst*. *To be submitted*.

Publications outside the scope of this thesis

L. Grajciar, C. J. Heard, A. A. Bondarenko, M. V. Polynski, **J. Meeprasert**, E. A. Pidko, and P. Nachtigall, *Towards operando computational modeling in heterogeneous catalysis*. *Chem. Soc. Rev.*, 2018, **47**, 8307-8348.

D. Culver, R. Dorn, A. Venkatesh, **J. Meeprasert**, A. Rossini, E. A. Pidko, A. Lipton, G. Lief, and M. Conley, *Active Sites in a Heterogeneous Organometallic Catalyst for the Polymerization of Ethylene*. *ACS Cent. Sci.*, 2021, **7**(7), 1225-1231.

A. Venugopal, L. H. T. Egberts, **J. Meeprasert**, E. A. Pidko, B. Dam, T. Burdyny, V. Sinha, and W. A. Smith, *Polymer Modification of Surface Electronic Properties of Electrocatalysts*. *ACS Energy Lett.* 2022 **7**(5), 1586-1593.

E. Khramenkova, **J. Meeprasert**, E. A. Uslamin, and E. A. Pidko, *Operando Computational Characterization and Modelling in Heterogeneous Catalysis*. *Submitted*.

